Doctoral theses at NTNU, 2021:32

Jan Inge Hammer Meling

Hydrogen assisted crack growth in iron: a simulations approach

Doctoral thesis

NTNU
Norwegian University of Science and Technology
Thesis for the Degree of Philosophiae Doctor
Faculty of Engineering
Department of Mechanical and Industrial Engineering

NTNU
Norwegian University of Science and Technology

Jan Inge Hammer Meling

Hydrogen assisted crack growth in iron: a simulations approach

Thesis for the Degree of Philosophiae Doctor

Trondheim, February 2021

Norwegian University of Science and Technology
Faculty of Engineering
Department of Mechanical and Industrial Engineering

NTNU
Norwegian University of
Science and Technology

NTNU
Norwegian University of Science and Technology

Thesis for the Degree of Philosophiae Doctor

Faculty of Engineering
Department of Mechanical and Industrial Engineering

ISBN 978-82-471-4983-6 (printed ver.)
ISBN 978-82-471-4985-0 (electronic ver.)
ISSN 1503-8181 (printed ver.)
ISSN 2703-8084 (online ver.)

Doctoral theses at NTNU, 2021:32

Printed by NTNU Grafisk senter

Summary

Hydrogen enhances crack growth, limiting the lifetime of industrial components. Despite the abundance of research into hydrogen enhanced crack growth and its proposed mechanisms, none of the models can explain all the observations.

The effect of hydrogen on the growth of a sharp crack in a Fe-3wt%Si is an enhanced crack growth rate and a sharper crack. The higher the hydrogen gas pressure, the sharper the crack tip. Other observations include a reduced residual plastic zone. The objective of this thesis is to investigate how hydrogen may cause the enhanced crack growth rate and crack sharpening by implementing variants of the hydrogen mechanism HEDE and HELP.

In this work, we show that hydrogen can activate mechanisms suggested by the literature, and the deciding factor is system-specific. Two different simulation models are used to investigate the hydrogen effect. The first is a study on a sharp crack simulated using 2D discrete dislocation dynamics. In the case of a sharp crack tip in Fe-3wt%Si, a reduction in the cohesive energy at the crack tip is the most critical for the crack growth and sharpening of the crack. The second study is a time-dependent microstructure evolution model of nanoindentation. In the case of nanoindentation, the reduction in the line energy of dislocations is the most prominent hydrogen effect.

Both models emulate the hydrogen mechanisms through the defactant framework. The defactant framework describes the hydrogen influence as a reduction in the energy of defects as a function of the chemical potential of hydrogen. The hydrogen effect of reducing the line energy of dislocations does not replicate the sharpening of the crack. A reduction in the cohesive force, on the other hand, does. A lowered cleavage criterion due to decohesion at the crack tip results in less plasticity before a cleavage event. Activation of a cleavage event at a lower load replicates the experimental findings of lowered fracture toughness, enhanced crack growth rate and a sharper crack tip. However, this does not rule out the hydrogen effect on dislocations, as that hydrogen effect replicates the lowered pop-in seen in nanoindentation experiments.

Hydrogen can promote several fracture types; intergranular, transgranular or void growth and coalescence. Which fracture type hydrogen promotes, depends on the loading conditions, charging conditions and the underlying microstructure. Hydrogen promotes local deformation where it accumulates, and different loading and charging conditions can change where and at what rate hydrogen is accumulating. The hydrogen effect should be linked to the charging conditions using the chemical potential of hydrogen. We suggest the best way forward is to assume the hydrogen effect is a hybrid of several mechanisms, and which is critical depends on the system.

Preface

This doctoral thesis has been carried out at the Norwegian University of Science and Technology (NTNU) at the Department of Mechanical and Industrial Engineering. The work has been conducted between November 2016 and October 2020 under the supervision of Professor Afrooz Barnoush and Professor Astrid de Wijn. The computations were performed on resources provided by the NTNU IDUN/EPIC computing cluster [1].

The thesis was financially supported through the HyF-Lex project (Petromaks 2 Program, Project No. 244068/E30) by the Research Council of Norway (RCN).

Acknowledgments

I would like to thank my supervisors Professor Afrooz Barnoush and Professor Astrid de Wijn. Thank you, Professor Afrooz Barnoush, for letting me work on your ideas which are the basis of this thesis. You have done me a huge favour allowing me to work with you and your team. You always made sure to keep my head to the ground and related to the experimental data. Thank you, Professor Astrid de Wijn, for providing the valuable opportunity of working with you. You have taught me much in mathematical modelling, physics and scientific common sense. Though many have helped, you two are the most significant contributors to the quality within my thesis.

There are so many to thank, and I hope I do you justice. Professor Alexander Hartmaier, you have been fantastic, and I cannot thank you enough for all your patience and willingness to help. You provided the code which the majority of this thesis work is based on, and you have quite admirably stuck with us to guide us through the model. Your insights have been invaluable. Dr Inga Ringdalen, you have helped me in so many ways. Your understanding of dislocations, and the corresponding simulation methods have helped me considerably. Without your insight, I would be far behind. Professor Christan Motz, your guidance was vital to my progress, and I hope I can repay by finishing the work we have started. Professor Nuria Espallargas, thank you for your help during these last months, they have been vital.

To my coworkers who made my good days great and my bad days tolerable; Brage, Gaute, Robin, Cristian, Jørgen, Kristoffer, Andreas and so many others, thank you. A special thanks to Di and Dong, your ideas and discussions often removed the monotony of the workdays. Di, you helped me so much in so many things, thank you. To Dong, my time as your office mate has been the best, and I have been truly blessed. My wife gave me a reason to go home; you gave me a reason to come to work.

To my wife, my love, and my everything. You are my reason to bother, to give a damn. Thank you.

Table of Contents

List of Tables

List of Figures

Chapter 1

Introduction

The work in this thesis is part of the project ”field life extension through controlling the combined material degradation of fatigue and hydrogen (HyF-Lex)”. The project aims to investigate, understand and measure the influence of hydrogen on fatigue crack growth in iron. Macroscopic testing of the hydrogen effect on iron and steels often observes a reduced strain to fracture. Hydrogen enhances crack growth, which reduces the load-bearing area. The current literature offers several chains of events leading to failure induced by hydrogen. A number of investigators have suggested that hydrogen affects the elastic fracture toughness of cracks and interfaces such as grain boundaries. A further portion has related the hydrogen effect to plasticity and dislocations, arguing that hydrogen changes the plastic response of the material. Others have found a hydrogen effect linked to enhanced formation of vacancies or hydrides.

Comparing the experimental data is difficult due to differences in mechanical loading, chemical application of hydrogen and the investigated material. In this work, we are investigating hydrogen embrittlement, with an emphasis on removing these complexities. Features such as grain boundaries and precipitates complicate the analysis. Therefore, the work focuses on monocrystalline iron or similar materials. Moreover, mechanical loading can be controlled by selecting an experiment where one single stress concentrator is dominant. The charging conditions for hydrogen is controlled by identifying the chemical potential of hydrogen in the system.

This thesis investigates hydrogen embrittlement using dislocation theory and dynamics described in chapter 2. Chapter 3 will explore the literature of the effect of hydrogen on the fundamentals detailed in chapter 2. The two next chapters are each a simulation model of previous experimental testing on Fe-3wt$\%$Si. Chapter 4 is a 2D discrete dislocation dynamics simulation of a single edged notched tension specimen subject to a load. The simulation can estimate the plastic response of the crack and calculate the elastic and plastic work for the fracture of a sharp crack. Chapter 5 is an initial value problem which estimates the load-displacement curves from nanoindentation. The nanoindentation model finds the displacement achieved during indentation through estimating corresponding elastic and plastic deformation. In the end, a summary of the discoveries of the work, with related discussions in chapter 6 and conclusions of the thesis in chapter 7.

Due to the difficulty in ascertaining the exact hydrogen effect, considerable effort has gone into correlating the two different simulation models. The intention is that the two simulations are based on the same fundamental dislocation theory. The implementation of the hydrogen effect in one is possible in the other.

Chapter 2

Fundamentals of Plasticity and Fracture

The strength and toughness of a material are dependent on its microstructure, or in essence, the defects within. Dislocations are one type of these defects and are the primary process of distributing strain energy. The work in this thesis will be based around dislocation theory, including discrete dislocation and collective dislocation behaviour. The two simulation approaches in chapter 4 and 5 uses the theory described in section 2.1 as a foundation. The approach in chapter 4 uses a 2D version of a simulation technique, described in section 2.2, that calculates the dynamics of discrete dislocation nodes. The model in chapter 5 uses a phenomenological approach, described in section 2.3, where state parameters represent the system and its microstructure. At the end (section 2.4), we will briefly touch upon cracks and the role of plasticity.

2.1 Dislocation Theory

Plastic behaviour in metals is a reaction to stress, lowering the strain energy in the system. This plastic behaviour can occur in the form of a local deformation, creating a mismatch in the lattice. This mismatch is a linear lattice defect called a dislocation. Dislocations are defined by their dislocation line $\vec{n}$ and Burgers vector $\vec{b}$. The dislocation line is the boundary line dividing the slipped and unslipped regions within the lattice. As a dislocation moves, it will shift the lattice it moves along, otherwise known as slip.

The Burgers vector is the indicator of the slip direction and magnitude. In dislocation theory, there are two defined types of dislocations, edge and screw dislocations. The edge dislocation is a dislocation where the Burgers vector is perpendicular to the dislocation line $\vec{n} \perp \vec{b}$, while the screw dislocation line is parallel to the Burgers vector $\vec{n} \parallel \vec{b}$. Figure (2.1) illustrates both an edge and a screw dislocation.

The elastic theory used in our work leads to a singularity at the core of the dislocation. The energy of a dislocation is separated into contributions from the long-range elastic strain and the atomic mismatch at the core. The self-energy of dislocations E_d is the sum of the elastically strained bonds outside the core and the core configuration of the dislocation. For BCC iron, the core energy is around 0.5 eV/nm, and the long-reaching strain energy is about 5 eV/nm. The energy of the dislocations is proportional to its length, consequently the longer the dislocation line, the more energy it has.

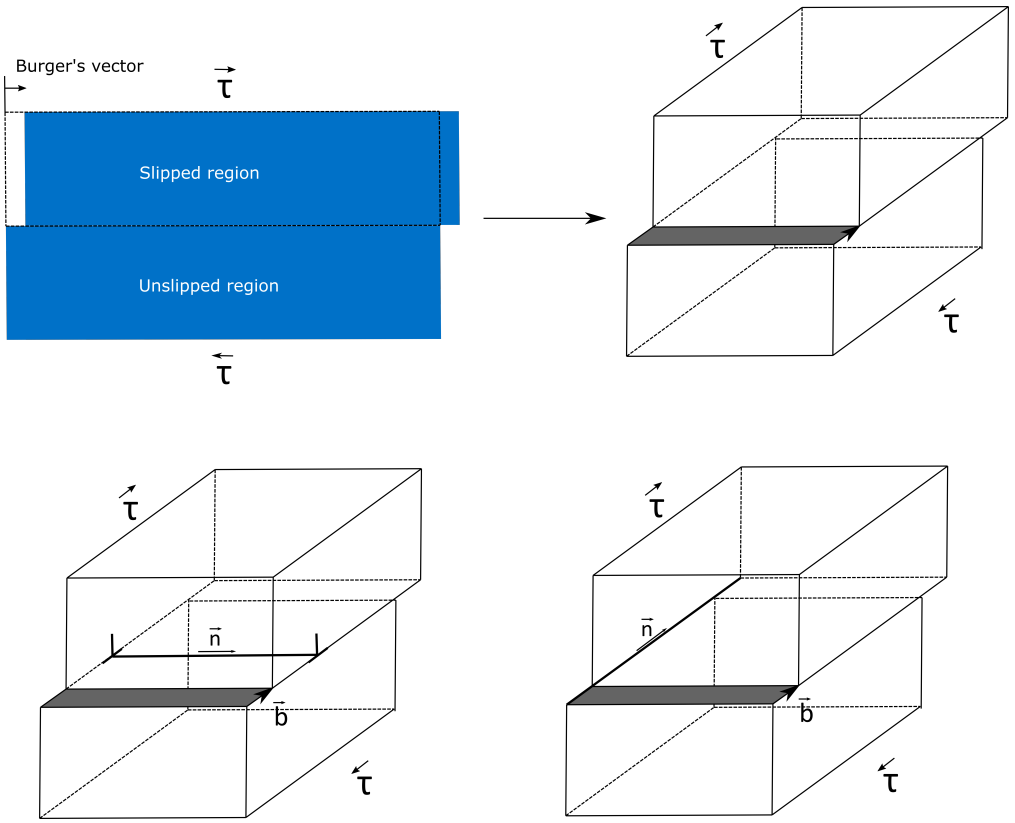

Figure 2.1: Illustration of an Edge vs a Screw dislocation; Notice how the Burgers vector is the same, and the slip area is the same, but the dislocation lines are different. The edge dislocation line is moving inwards into the paper, shown in the bottom left. The screw dislocation line is moving to the left, shown in the bottom right.

2.1.1 Elastic Fields of Dislocations

Dislocations distort atomic bonds in their vicinity, producing a stress field as a result. The stress field from dislocations includes both dilational and shear components depending on the character of the dislocation and the elastic properties of the lattice. The most significant parameters for the stress field are the shear modulus G and the Burgers vector $\vec{\boldsymbol{b}}$. The shear modulus is the lattice's resistance against elastic deformation, and the Burgers vector is the amount of deformation. The stress field is long-ranged and will affect all other defects in the lattice, including itself.

The stress affecting a dislocation is a sum off external and internal stresses. The total stress can be separated into three terms, the external stress σ_{ext}, the internal stress σ_{int} and the image stress σ_{img}. The external stress is a result of the imposed load onto the specimen. The internal stress is a sum of all stress fields from other defects within the specimen. The image stress accounts for the attraction a dislocation feels towards a free surface. A free surface is more compliant than the bulk, by travelling to the surface, a dislocation will reduce the internal energy. The image term is a stress field which ensures that the tractions at the surface are zero.

There are numerous ways of estimating the stress tensor σ. For chapter 4, we will use a two-dimensional solution specific for dislocation interaction between other dislocations and a crack tip [2]. In chapter 5, we will be using a more macroscale approach, estimating the internal stress within the specimen due to the dislocation density.

2.1.2 Dislocation Movement

The Body-Centred Cubic (BCC) structure of iron has no clear dominant slip plane, resulting in a possible slip in three different planes (110), (112) and (123). The initiation stress is higher for (112) and (123) than for (110), but the difference is so small that in a practical sense all are operational. These three slip planes give 48 possible slip systems, making cross-slip for screw segments easy and leads to irregular wavy slip bands [3]. The possible three slip planes complicate the analysis of BCC systems, where each slip plane can have differing properties, for example, the Peierls stress [4].

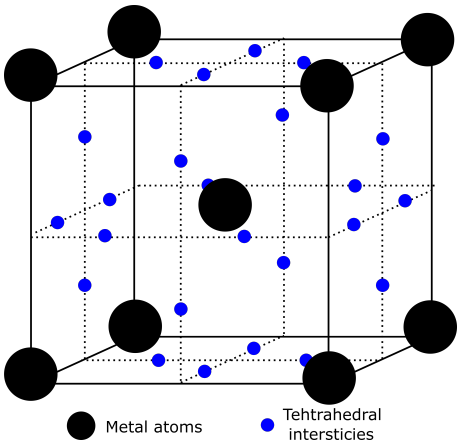

Figure 2.2: Illustration of BCC structure with tetrahedral interstitial sites.

The primary dislocation motion is gliding along the dislocation's glide plane, which has to contain both the Burgers vector and the dislocation line. A dislocation that is able to glide in this way is considered glissile. One that is not able to move in its glide plane is considered sessile.

Dislocation gliding needs to overcome a minimum stress to activate, that stress is called the Peierls Nabarro (Peierls) stress. The Peierls stress τ_{p} is the threshold stress needed to activate gliding at 0 K. When the Peierls stress is easily overcome, the dislocations movement

is determined by their ability to pass defects along their glide path. Examples of this occur in Face-Centred Cubic (FCC) metals, where the Peierls stress for dislocation glide is in the range of 10^{-5} to $10^{-4}G$.

The effective force on a dislocation can be resolved in the direction of movements using the Peach and Koehler [5] equation. The two principal directions of movements for a dislocation is, in glide plane or out of glide plane. Both directions are normal to the dislocation line. The first is the glide direction which contains both the slip plane and slip direction. The second is normal to the glide direction, where the dislocation would climb to another slip plane. The effective force can be found through $\vec{\boldsymbol{f}} = (\sigma \cdot \vec{\boldsymbol{b}}) \times \vec{\boldsymbol{n}}$, where σ is the stress tensor.

The dislocation's glide velocity is based on a drag force $v_{\text{glide}} = \vec{\boldsymbol{f}}_{\text{glide}}/B$, where B is the drag coefficient. $\vec{\boldsymbol{f}}_{\text{glide}}$ is the sum of the effective forces on the dislocation in its gliding direction. The dynamics in chapters 4 and 5 assumes an overdamped situation. Inertial effects are neglected and the velocity of dislocations are estimated through phenomenological velocity equations.

The initial estimations of dislocation velocities are based on their collective movement and impact on the macroscale. The intention was to understand the plastic behaviour of metals by correlating dislocation speeds and achieved plastic strain using the Orowan equation, explained in section 2.3. Several laws have been suggested, but most include a velocity prefactor v_0, a friction stress τ_0 and a stress sensitivity m. The power-law, $v(\tau, T) = v_0 \exp\left(-Q_D/k_B T\right)(\tau/\tau_0)^m$, accounts for the temperature effect through an activation barrier for dislocation movement, Q_{D}. The power-law represents the velocity of dislocations in pure iron as a function of stress, τ, and temperature, T. k_B is the Boltzmann constant. The power-law captures the experimentally observed effects, such as the temperature and stress dependence of dislocation movement.

The mobility of screw segments in BCC is much lower than for the edge segments. Screw dislocations have a high Peierls stress, $10^{-2}G$, rendering planar glide unlikely. The reason for the high Peierls stress is the core of the screw dislocation. In BCC, the screw dislocation has its core equally distributed on three slip planes. Due to the high stresses necessary for glide, screw dislocations will move using another mechanisms called kink-pair nucleation and migration.

Screw dislocation movement through kink-pair nucleation and migration can occur through a single or several nucleations of kink-pairs. A kink-pair is produced when a local segment of a dislocation line is shifted a distance along a glide plane. The kink-pair consists of the shifted local segment, which is parallel to the dislocation line and two edges which connects the local segment with the trailing dislocation line. The two edges are called kink edges and are normal to the dislocation line. The stability of kink-pairs depends on the distance between the kink edge segments and the resolved shear stress on their glide plane. Stable kink-pairs can shift the trailing dislocation line in its direction through kink migration. Kink migration is when the kink edges of the kink-pair moves parallel to the screw dislocation line, shifting the dislocation line in the direction the kink-pair formed.

The kink-pair nucleation and migration movement is here differentiated into two different regimes, regime 1 and regime 2. Formation of kink-pairs and kink migration can occur on all three of the slip planes. The screw dislocation movement would be based on the resolved shear stress on these slip planes. The plane with the highest resolved shear stress will be refereed to as the primary plane in this work. The kink-pairs in the primary plane have a higher survival rate, and the kink edges have a higher migration speed. At high formation energy of a kink-pair, or when the temperature is low, a single kink-pair will form on the primary plane. This is regime

1, shown in Fig. (2.3a). In regime 1, the kink nucleation rate is the determining factor for the dislocation movement. In regime 2, Fig. (2.3b), when the formation energy of kink-pairs is low, several kink-pairs may be formed. Kink-pairs can form so readily that formation can occur on the two other slip planes and other kink-pairs. As the kink edges glide, they can encounter opposite kink edges and annihilate. Annihilation between dislocations is covered in section 2.1.3. When the kink edges encounter kink edges on the two other slip planes they will intersect and form sessile segments. These new sessile segments can acts as anchors to the dislocation and when left behind, act as defects to other dislocations. In regime 2, the kink migration time is the determining factor for the dislocation movement.

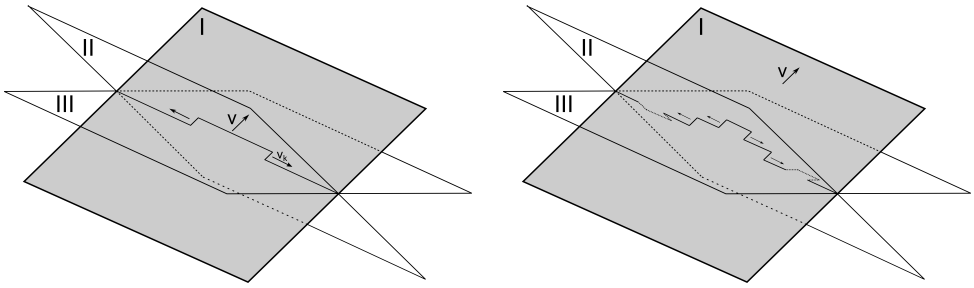

(a) Regime I **(b)** Regime II

Figure 2.3: Kink nucleation and migration of a screw dislocation in two different regimes. The dislocations primary plane (highest resolved shear stress) is marked as I and shaded gray. In regime I, only a single kink-pair is nucleated and the velocity of the equation is determined by the stability of the nucleated kink-pair and subsequent kink migration v_{k}. In regime II kink-pair nucleation is easy, so there will be formation on all slip planes. Screw dislocation motion is now more dictated by density of kink-pairs in the primary glide plane

Screw mobility in iron has a linear relationship between its length and velocity. This length dependency occurs due to the nature of kink-pair nucleation and migration. Small screw dislocation's movement is mostly controlled by the nucleation rate of the kink-pairs, the kink-pair nucleation time $t_{\mathrm{nucleation}} >> t_{\mathrm{Migration}}$. Longer dislocations, on the other hand, are more controlled by the density of the kink-pairs along the dislocation line and the speed of the kink-migration. There are a few different ways of estimating the speed of a dislocation line due to kink-pair nucleation and migration. In our case we will be using one where kink nucleation time is negligible compared to the kink migration time.

The velocity v for a screw dislocation is found as a result of kink-pair migration, assuming kink-pair nucleation time is negligible. The approach is a phenomenological, where it links the area covered by a concentration of kink-pairs c_{kp} over time with the velocity of the screw dislocation. The area covered by a kink-pair over time is determined by the height h of the kink-pair and the migration velocity of the kink-pair edges v_{kp}. The initial width of the kink-pairs are negligible compared to the distance covered by the migration $v_{\mathrm{kp}}dt$. The area covered by a concentration of kink-pairs along a dislocation length L over time $\mathrm{d}t$ is then $A_{\mathrm{kp}} = h(v_{\mathrm{kp}}dt)(c_{\mathrm{kp}}L)$. The velocity v of the screw dislocation is found by setting $vL\mathrm{d}t = h(v_{\mathrm{k}}\mathrm{d}t)(c_{\mathrm{kp}}L)$, which resolves to $v = hv_{\mathrm{k}}c_{\mathrm{kp}}$. The kink-pair concentration is assumed to be at equilibrium concentration for kink-pair nucleation $c_{\mathrm{k}} = 2/a\exp\{(-\Delta G_{\mathrm{kp}}/k_BT)\}$. The free energy for formation of

a kink-pair is the energy of a kink-pair Q_{kp} minus the resolved shear stress τ over the volume covered by the kink-pair $\Delta G_{\mathrm{kp}} = Q_{\mathrm{kp}} - V_{\mathrm{act}}\tau$. Setting $h \approx a$, gives the speed of a screw dislocation as

$$v(\tau) = 2v_{\mathrm{k}} \exp\left(-\frac{\Delta G_{\mathrm{kp}}(\tau)}{k_B T}\right). \tag{2.1}$$

Here v_k is the migration speed of a kink segment, assumed to be so fast that it is independent of the resolved shear stress. The activation volume V_{act} is an indication of the average size of the nucleated kink-pairs within the kink-pair density c_{kp}. The smaller the activation volume is, the higher the stresses must be to make the kink-pairs stable.

Alternative methods of movement

Two other notable methods of movement for dislocations are climb and cross-slip. As these types of movement are not implemented in this thesis, a brief explanation should suffice.

Climb is movement of an edge dislocation, where it moves from its slip plane to a parallel slip plane above or below the current slip plane. Climb occurs through diffusion of vacancies or self-interstitial atoms. Vacancy concentration and diffusion is thereby an essential factor in climb, and climb can be considered as a thermally activated movement. In the case of a high abundance of vacancies, climb would be easy.

As shown in Fig. (2.3), the screw dislocation has three slip planes it can move on. The screw dislocation will move on its primary plane of movement, where the shear stress is the highest. However, if the screw dislocation encounters a defect on that slip plane, it can move on the two other slip planes instead. This is cross-slip, and the change can be both global or local along the dislocation line.

2.1.3 Interactions

The interactions between dislocations detailed in section 2.1.1 are the elastic interaction between dislocations. Dislocations can also intersect and form a multitude of configurations. In chapter 4 the dislocations never intersect each other. This is not to say this type of dislocation interaction does not occur in the material that is modelled, just that they are not included as they are deemed negligible. These interactions are more relevant for chapter 5, where dislocation intersection dictates the ratio between glissile and sessile dislocations as well as the internal stress within the material.

As moving dislocations intersect, there are four types of intersections of interest. Three of them form new defects, and one removes them. The one who removes defects is termed annihilation and is when two opposite dislocation segments intersect. They cancel out $\vec{b}_1 + \vec{b}_2 = 0$. The three defect formations are jog, kink and junction formation. Jogs and kinks are products of two intersecting dislocations, which produce local shifts in their dislocation line. A jog is a shift in the local dislocation segment out of the slip plane. A kink is a shift of the local dislocation segment within its slip plane. These local shifts in a dislocation line act as anchors to further dislocation movement, and a stress threshold must be overcome for the dislocations to leave the debris behind. The formation of a junction is probable when the energy of the product is smaller than the energy of the dislocation segments separately, know as the Frank

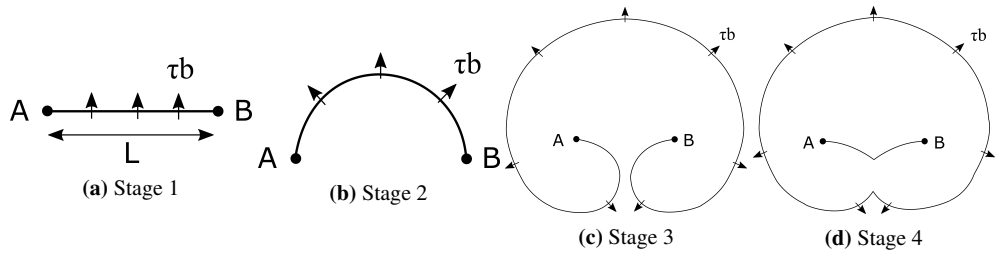

(a) Stage 1 **(b)** Stage 2 **(c)** Stage 3 **(d)** Stage 4

Figure 2.4: Illustration of a Frank Read source. There are four stages in the formation of a dislocation loop through a Frank Read Source. A dislocation line lies between point A and B. Point A and B are the end points of the dislocation and they are immobile. When a shear stress is applied, the dislocation line will bow out. When complete (Stage 4), a dislocation loop is formed and the source resets.

energy criterion. Junctions can be binary, tertiary or more, and are part of the sessile dislocation configuration.

2.1.4 Dislocation Nucleation and Multiplication

In this work, the nucleation and multiplication of dislocations are critical to the plastic response of the imposed load. The work in chapter 4 includes dislocation multiplication. Chapter 5 include both dislocation nucleation and multiplication.

Dislocation nucleation (homogeneous nucleation) is sudden nucleation of a dislocation in a perfect lattice and considered to be a rare event. These nucleations can take place frequently with a high attempt rate, though they collapse easily. The event can be described through classical nucleation theory, where the self-energy of the dislocation must be overcome for the nucleation to be stable. The shear stress onto the dislocation must be enough to resist the collapse of the dislocation. The necessary stress to homogeneously nucleate a dislocation is of the order $G/15$.

An much easier formation process for dislocations is the multiplication of dislocations, where dislocations are formed from defects. The defects may be a surface ledge, precipitates, jogs, kinks, or junctions connected by a dislocation line. The most commonly type referred too would be the case of a Frank Read source. A Frank Read source is a dislocation line terminated at both ends by a sessile point, as illustrated in Fig. (2.4a). The dislocation line moves due to external stresses, but the defects it is connected to are immobile. The dislocation line will then form an arc with a radius dependent on the resolved shear stress, stage 2 in Fig. (2.4b). When a critical radius is reached, further movement requires less stress. The bowing will extend around both defects, where the dislocation line eventually intersects itself, as shown in stage 3 in Fig. (2.4c). The local segments annihilate and connect the dislocation line forming a complete loop, see Fig. (2.4d). The formed dislocation loop is then able to escape, and the Frank-Read source resets to stage 1 and is capable of producing more dislocations. Other methods of dislocation multiplication are often variants of the Frank read source or spiral arms.

2.2 Discrete Dislocation Dynamics

Discrete Dislocation Dynamics (DDD) is an emerging and relatively new simulation technique [6, 7]. Our investigation into the hydrogen effect on the crack growth will use a 2D version of this DDD simulation technique (chapter 4). A short introduction to the DDD simulation technique is, therefore, given here.

The DDD simulation technique is a micro-level simulation focusing on the dislocation movement and interactions. The simulation space in DDD is continuous where dislocations can move, interact and multiply. In DDD the dislocations are defined by their Burgers vector and their dislocation line. In a 3D simulation, the dislocation lines are often divided into discrete segments, and each dislocation segment moves with a velocity determined by a net virtual force exerted on the segment. The virtual forces in the simulations may include elastic interaction between defects and other forces. These other forces could be, for example, an external force due to mechanical loading or image forces from a surface.

A single iteration of a DDD simulation would include: 1) Calculating the elastic interaction between the defects in the simulation volume. 2) Move the dislocations according to their net virtual force and the allowed forms of movement. 3) Check for collisions of dislocation segments, and use phenomenological rules to determine which type of intersection will occur.

DDD simulations have a number of challenges, some are computational, some are conceptual, and some are practical. Computational challenges are, for example, the long-range elastic interaction between the defects. The long-ranged elastic interaction makes the simulation computationally heavy, especially in DDD, where the number of defects increases with increasing strain. At the same time, the time-steps must be small for the dynamics to be accurate when dislocations are close together. The conceptual challenges are deciding how to implement dislocation line intersection and transformation, i.e. kink, jog or junction formation. Finally, the bookkeeping needed in the DDD simulations is quite extensive, which make designing the code structure difficult. For example, each dislocation line must be represented by a set of coordinates for the discrete segments, and their corresponding Burgers vector, the links between the segments and the shared nodes (junctions) between dislocation lines.

DDD simulations are used to describe the dynamics of a network of discrete dislocations. As a result, they are often used to investigate microstructural features. One area where this is done a lot is strain hardening (see, for example, [8, 9, 10, 11]). Modelling the strain hardening between material systems can often demand different approaches as the conceptual rules have to account for varying microstructural features, such as grain boundaries, texture, precipitates and different phases.

DDD simulations have also been augmented by coupling it with a Finite Element Method (FEM), where it can represent more complex geometries and inhomogeneous stress fields. The FEM modules can also incorporate surface effects by solving the stress field so that the tractions normal to the surface are null [12]. This allows investigating the size effect found in deformation of samples at micro scales [13, 14].

2.2.1 DDD Simulation of Crack Growth

Simulating crack growth presents additional computational challenges on top of those already mentioned above. The first added challenge is realistically resolving the movement of disloca-

tion line segments distributed over large strain gradients. To accurately capture the dynamics of a dislocation line in a high strain gradient field, the length of the segments must be short, and the time steps small. Another challenge is the inhomogeneous stress field of the crack. The inhomogeneous stress field can be produced with a FEM module, though this adds significantly to the computations.

One approach to reduce the computations is to solve the problem with a 2D model. In 2D simulations, the dislocations lines are assumed to be perfectly straight and infinitely long. The complexities of dislocation intersection, junction formation and dislocation multiplication from the bulk, when appropriately, can be neglected without affecting the overall behaviour of the system. These features can practically be removed to achieve higher numerical efficiency. The 2D method can, therefore, treat each dislocation as a single node, the position of which can be described with one 2D vector. Producing the inhomogeneous stress field with a FEM module in a 2D representation of a crack is computationally cheaper than in 3D [15]. There are also analytical solutions for the stress fields that can be used more easily in such a 2D setup [2, 16].

The 2D models are therefore computationally much cheaper than 3D, allowing for investigations into systems at a higher level of deformation (strain). Also, when investigating a complex problem such as hydrogen embrittlement, it is beneficial to keep the rest of the simulation as efficient and straightforward as possible.

2D simulations have thus been used for investigations into; The Hall-Petch effect in nanocrystalline metals[17], strengthening effect of preexisting obstacles [10], or studies into the size effect in small scale testing of cantilever bending [14]. Simulating the loading of a plane crack has previously been solved in 2D [15, 18, 19], where the load and boundary conditions are solved by the Finite Element Method. The cohesive zone model solves the fracture condition. The FEM and Cohesive zone model can introduce a higher level of detail of the deformation processes. However, the higher level of detail often comes at the cost of numerical efficiency.

An example of a 2D model that is able to achieve high loads is a quasi-static 2D DDD simulation [20], including an analytical stress field [2] of a crack tip due to an imposed external load. The model simulates discrete dislocations, with dislocation generation close to the crack tip and their movement away. The interactions in the model are purely elastic, core effects and dislocation intersections are neglected. Though it is simplified, it can estimate the elastic and plastic work necessary for a cleavage fracture. By estimating the elastic and plastic work for fracture, the BDT can be approximated by changing the dislocation mobility as a function of the temperature. The model have thus previously been utilized to investigate the Brittle to Ductile Transition (BDT) temperature seen in BCC materials such as Si [21, 22], Fe [23] and W [20, 24, 25, 26].

The main objective of this thesis is to understand the Hydrogen effect on crack growth. The hydrogen effect on crack growth is complicated, as will be illustrated in section 3, there is no need to add to that complexity unnecessarily. Moreover, the hydrogen effect on the cleavage criterion is more significant at relatively high loads. Thus this problem is particularly suitable for investigating with the 2D model introduced above.

2.3 Plasticity

The theory of dislocations presented above helps us understand and model the irreversible deformation of a material due to an imposed load. This irreversible deformation is called plasticity,

and it accounts for the material's ability to accommodate loading through plastic deformation. The strength and ductility of a material is, mostly, determined by its ability to activate plasticity; in other words, multiply dislocations and move them. Plasticity is activated when the stresses in the system reach or exceeds a threshold, the flow stress. Activation of plasticity can lead to a change in the defect density within the material. An increasing defect density can lead to an strengthening effect. The strengthening effect is called strain hardening, and it accounts for the increased resistance against further plastic deformation.

The plastic deformation a material undergoes during loading can be grouped into four stages. Each stage represents a different strain hardening behaviour. The transition between the stages depend on the evolution of the microstructure. The first stage has little to no strain hardening and is linked to the step-wise activation of slip-systems. The flow stress increases locally within the activated slip systems. However, the global average flow stress of the system is not significantly changed. As the flow stress in the activated slip systems increases, other slip systems are activated instead. The first stage is not common as it needs a low initial dislocation density and a significant amount of available dislocation sources. The second stage is linked to a linear increase in the flow stress and starts when storage mechanisms are activated. These storage mechanisms increases the defect density by pinning moving dislocations within the material system and are related to dislocation intersections such as kink, jog or junction formation. The increasing dislocation density increases the flow stress, either through counteracting elastic interactions or through pinning of moving dislocations. The third stage is marked by a decreasing strain hardening, as in the hardening rate decreases with further deformation. The decrease in hardening rate is due to an increase in the rate of recovery, leading to a slower increase in the defect density. An example of a recovery mechanism is dislocation annihilation through climb. At stage four, the hardening rate is zero, and the flow stress becomes constant. The rate of recovery now equals the rate of storage, and the internal dislocation density reaches a steady state.

As we have pointed out, during all four stages the flow stress increases with increasing defect density. The increase in flow stress occurs because dislocation movement and multiplication are harder to activate. A higher dislocation density means more pinning and increased resistance to glide. To activate plasticity, the stress on the dislocation configuration must be higher as the stress has to overcome the additional internal stresses. The strain hardening process is system-specific, where, for example, the flow stress can be a function of the mobility of dislocations and the external loading rate. In other cases, obstacles along the glide path of dislocations are the rate-determining factor. When dislocation mobility is the rate-dependent factor, as it is in BCC, the temperature or loading rate can affect the flow stress of the system.

DDD modelling beyond stage 2 is computationally heavy, because of the large number of dislocations. An approach for dealing with this is to describe the evolution of the dislocation network through averages, such as dislocation densities. These types of models can also account for more complex microstructure features, for example grain boundaries, strengthening effects from substitutional, and interstitials solutes or other phases. This macroscale approach can describe the texture, dislocation network and other defects through state parameters and constitutive relations. In simple systems the microstructure can be described by a single state variable, the dislocation density [27, 28, 29]. The evolution of the microstructure, in this case, is described through storage and recovery mechanisms. The evolution of the time-dependent state parameter is described by rate equations that contain the rates of storage and recovery, which

depend on strain, which in turn results from a time-dependent stress. The single state parameter models can capture the increase in flow stress when the deformation and the dislocation density is homogeneous. The models fail when the microstructure is in, or has evolved to a state, where the deformation and dislocation densities are no longer homogeneous.

When the the microstructure consists of several features, additional state parameters could be introduced [30, 31, 32, 33, 34]. These features could be inhomogeneous dislocation densities, large misorientation between grains or when the dynamics of the microstructure are transient. The transient behaviour could be sudden plastic avalanches, for example, the pop-in during nanoindentation [35, 36]. The transient behaviour can be solved by introducing a second state parameter, splitting the dislocation configuration into two subsets, glissile (mobile) and sessile (forest) dislocations [37, 38]. The reasoning is that these two subsets of the dislocation densities are the cause of independent features. The mobile dislocation density activates plastic deformation of the system to accommodate the load and lower the internal energy. The forest dislocation density is responsible for the increasing internal stress within the system. Depending on the system, the increased internal stress is a result of increased elastic interaction or increased pinning of the dislocations. This modelling approach using the two-state variables representing the microstructure is adopted in chapter 5, while also introducing a third state variable for the plastic deformation, the plastic strain.

2.4 Cracks

Cracks may be formed in the production step, or through damage from internal or external stresses. A crack is a stress raiser, as it reduces the load-bearing area, projecting stresses ahead of the crack tip. The fracture toughness of a perfectly sharp crack tip depends on the interatomic bond between the atoms at the tip of the crack. Loading a crack means putting a strain on these atomic bonds. The strain on the atomic bonds at the crack tip is often represented by a stress intensity factor, which describes the stress state of the crack tip due to a global load. The stress intensity factor can account for geometric effects due to the test specimen and loading conditions.

The stress necessary to break these bonds can be found through a thermodynamic approach by Griffith [39]. He found that the stress necessary to break the bonds is equal to the energy needed to create two new surfaces. The criterion worked for brittle materials such as glasses, but severely underestimates the fracture toughness of metals. What the criterion is missing is an estimation of the dissipated energy. The crack can distribute its strain energy through emitting or attracting dislocations. Whether or not the crack can accommodate the load depends on its ability to activate plasticity compare to the load rate. Regardless if the dislocations already exist, are multiplied from the crack tip or other sources, a dislocation will have an impact on the stresses at the crack tip. Dislocations can either be shielding or anti-shielding, meaning that they will either lower or increase the stress state of the crack tip. Consequently, shielding dislocations are repulsed from the crack, whereas anti-shielding dislocations are attracted to the crack. Dislocations emitted from the crack tip will cause the crack tip to blunt and grow, whereas the anti-shielding dislocations will blunt the crack where they intersect the crack.

The blunting effect reduces the stress field ahead of the crack. A blunt crack is found in materials where dislocation motion is easy and plasticity occurs readily. Rice & Thomson [40] have shown that for some FCC metals such as aluminium and nickel, an atomically sharp crack

tip is unstable, and multiplication of dislocations at the crack tip is a spontaneous process. If a sharp crack is present in the material, it activates plasticity, blunting itself with little to no external stress. In these cases, a blunt crack grows through a mechanism known as void nucleation, growth and coalescence. This fracture mechanism will not be explored in this work, though suffice it to say that the hydrostatic pressure formed due to the plasticity ahead of the crack will help nucleate voids along the crack path. These voids can grow and coalesce, growing the crack and reducing the global load bearing area. This fracture mechanism requires a lot of energy and is correlated with high fracture toughness and as a ductile fracture.

For most BCC materials, on the other hand, the multiplication of dislocations at the crack tip is not a spontaneous process [40], and a local strain at the crack tip is needed to generate the necessary stresses for dislocation multiplication. In case of low dislocation mobility or lack of surrounding dislocation sources, the majority of plasticity is generated at the crack tip. If the material is unable to activate dislocations movement and multiplication, the crack will propagate in a brittle manner. When mobility and nucleation of dislocations depend on external parameters, a transition between the cases is possible, a mixed case where the material can exhibit plasticity before a cleavage event. The most common example of this phenomenon is the Brittle-Ductile Transition for BCC material. In these cases at a low or intermediate temperature, plasticity can be activated but is too slow to accommodate the increasing strain at the crack tip, and a cleavage event is activated. As dislocation mobility increases with temperature, the crack is more able to accommodate the load, and the fracture toughness increases.

For cracks operating at loads above the critical stress intensity, $K_{\mathrm{I,C}}$, the strain energy release mechanisms of a crack are not enough, and it will lead to unstable crack growth. Therefore, cracks should only operate in stress regimes where crack growth is stable or not happening. The stages in crack growth can be grouped into three regimes, regime one being where the growth is either not existent, negligible or reversible. Regime two is where crack growth is stable and predictable. Regime three is when the crack growth becomes unstable and catastrophic failure is imminent. Hydrogen embrittlement can affect this process as it changes the threshold stress intensities, often shifting them towards lower values. In the region close to the crack tip, the hydrostatic stress enhances the hydrogen solubility locally at the crack tip and flux towards the region. The diffusion speed of hydrogen from bulk or surface to the crack tip is therefore critical. Increased temperature or decreased strain rate increases the materials ability to release strain energy in the form of dislocations. At the same time, it also increases the distance travelled by hydrogen.

Chapter 3

Hydrogen Embrittlement

This chapter will introduce the problem of hydrogen embrittlement. The intent is to discuss the state of the hydrogen embrittlement field, and relate it to the dislocation theory introduced in chapter 2.

Research into hydrogen embrittlement started with the work of Johnson [41, 42], where he noted the embrittling effect of cleaning iron or steel in sulphuric acid. He found similar results with other acids and concluded that the common denominator is hydrogen. Johnson wrote

> For a long time it has been well known to wire drawers and other manufacturers, who free the iron or steel they are engaged in working from rust by cleaning it with sulphuric acid, that after this process the metal becomes much more brittle than before. Further, if a piece of iron wire that has been cleaned in sulphuric acid be bent rapidly to and fro till it is broken, and the fracture be then moistened with the tongue, bubbles of gas arise from it, causing it to froth. If the same wire be now gently heated for a few hours, or left in a dry warm room for some days, it will be found to have regained its original toughness, and not to froth when broken and the fracture moistened.

Hydrogen, it seems, causes catastrophic fracture of iron or steels at a lower strain than intended. Though, if hydrogen diffuses out of the material, it should regain its fracture toughness.

The work in the hydrogen field after Johnson's discovery includes suggestions that hydrogen affects the interphases, dislocations, vacancies or the formation of brittle hydrides. Despite the abundance of research into this field and proposed mechanisms, none of the models can explain all the observations. All mechanisms have their suggested chain of events leading to the catastrophic fracture; the problem is to determine which mechanism is the critical one.

The work in this PhD will focus on hydrogen assisted crack growth in ferritic iron, including modelling at a different time and length scales using dislocation theory as a common foundation. The section will begin with an overview of the current literature and suggested mechanism for hydrogen embrittlement in section 3.1. How to approach simulation of the hydrogen effect is detailed in section 3.2, and a literature study on the effect of hydrogen on defects is in section 3.3.

3.1 Overview of Testing on Iron and Steels

The intent of our models in chapter 4 and 5 are to implement different mechanisms and see which one can replicate the experimental data. This section offers an overview of key discoveries and discuss mechanisms that may be relevant to enhanced crack growth and their connection to our simulation models.

A key problem in testing of the hydrogen effect is that it leads to different changes, depending on hydrogen application, temperature, mechanical testing and material. Pfeil's [43] tensile testing of pure iron indicates that different microstructure can exhibit different hydrogen effects. Pfeil carefully tested both finely crystalline and single grained samples. He found a notable drop in fracture strain in both cases, while a loss in tensile strength was only significant in the finely crystalline samples. He noted in his test that the deformation mode enhanced by hydrogen differed from trans-crystalline, inter-crystalline, cleavage or a mix of the three. The transition between them could be temperature, charging of hydrogen or the underlying microstructure. He concluded that hydrogen's critical effect was a weakening of the inter-crystalline boundaries, which leads us to the introduction of one of the most well-known hydrogen suggested mechanism, Hydrogen Enhanced Decohesion.

3.1.1 Hydrogen Enhanced Decohesion

Hydrogen Enhanced Decohesion (HEDE) argues that hydrogen lowers the cohesive strength in the lattice. HEDE was established by Oriani [44], who introduced the cohesion force for atomic bonds. The cohesion force describes the inter-atomic bonds resistance to rupture. This force depends on a critical theoretical stress level that needs to be overcome. HEDE argues that the presence of hydrogen weakens cracks and interphases, such as grain boundaries. Oriani compared the necessary stress intensity for fracture of a sharp crack tip in AISI 4340 steel to a varying hydrogen gas pressure. An increase to the gas pressure of hydrogen leads to a smaller K^{C} needed for fracture. The high hydrostatic stresses close to the crack tip increase the hydrogen concentration locally, which in turn causes a drop in cohesion force. A higher gas pressure indicates a higher hydrogen solubility in the metal, leading to a faster saturation at the crack tip.

Vehoff & Rothe [45] have documented similar findings where a single crystal Fe-3wt$\%$Si specimen was tested at different hydrogen gas pressures. They correlated the crack tip opening to a changing hydrogen gas pressure. Without hydrogen, the crack tip opening was dictated by the slip systems activated at the crack tip. This process is indicative of crack growth through dislocation emission, where the crack surface is shifted according to the Burgers vector of the generated dislocation. When hydrogen is introduced, the crack sharpened, indicating crack growth through cleavage. An increase to the gas pressure leads to a sharper crack tip.

When discussing the effect of hydrogen on the cohesive force between atoms, there are two parameters of interest, the theoretical strength σ_{th} and the work of separation WoS. The theoretical strength is the threshold stress necessary to break the bond. The work of separation is the energy released in the process. The Griffith criterion, as discussed earlier in section 2.4, estimates the theoretical stress by comparing it to the energy that will be released in the process. If the work of separation is reduced due to hydrogen, there should be a similar reduction in the theoretical strength [46, 47].

In our work, the hydrogen effect on surface energy is used to estimate the reduction to the cleavage criterion K^{C}. The lowered cleavage criterion is one of the two major hydrogen effects implemented in this work. The other change is the effect of hydrogen on dislocations, which leads us to the next suggested mechanism.

3.1.2 Hydrogen Enhanced Localized Plasticity

Hydrogen Enhanced Localized Plasticity (HELP) argues that the most critical impact of hydrogen is related to the effect on dislocations. It began with, the paper from Beachem [48], where he performed wedge crack testing and torsion testing. Beachem argued that hydrogen's embrittling effect is enhancing whatever deformation mechanism that is possible. The hydrogen effect would occur at places of high triaxial (hydrostatic) stress, where hydrogen would accumulate, and enhance the available deformation mechanisms.

Tabata and Birnbaum investigated the effect of hydrogen on dislocations and a crack in Transmission Electron Microscopy (TEM) samples. They recorded an increase in dislocation mobility correlated with the hydrogen gas pressure [49]. Introducing hydrogen to a sharp crack activated a plastic response at a lower load than without hydrogen [50]. The increased velocity causes an enhanced plastic response, though only where the presence of hydrogen is considerable.

It is argued that instead of a global response to the load, plasticity is activated where hydrogen has accumulated. The enhanced plastic response locally then deforms at a lower load than without, activating the available deformation mechanisms. This, in turn, could lead to faster crack growth, faster void nucleation and growth or faster build-up of stresses at weak points, such as grain boundaries.

When it comes to how hydrogen causes an enhanced plastic activity, there are two possibilities considered here. The first is that hydrogen reduce the elastic stresses between dislocations; the other is that hydrogen enhances the mobility of dislocations. Each has its merit and will be further discussed in section 3.3.1.

3.1.3 Defactant Model

The defactant mechanism was introduced by Kirchheim [51, 52], where he argues that the hydrogen effect can be generalised as a reduction in the formation energy of defects. The theory has been used to explain the lowered pop-in force seen experimentally in nanoindentation with hydrogen present [53, 54].

The main effect of hydrogen is lowering the energy of defects, much like surface acting agents can lower the energy off a surface. The effect is described through $\mathrm{d}\gamma = -\Gamma_H \mathrm{d}\mu_H$, where γ is the energy of a defect. Γ_H is the excess hydrogen at the defect and μ_H is the chemical potential of hydrogen. The higher the chemical potential of hydrogen, the lower the energy of the defect. Hydrogen would in this case cause formation of defects at lower loads than without, promoting an earlier deformation.

In our simulations, the defactant model will serve more as a framework through which HEDE and HELP will be implemented. Both HEDE and HELP are suggestions for how hydrogen affects the deformation of the material, with a corresponding chain of events leading to fracture. Though both have an explanation for how the fracture occurs, the exact theory on

how hydrogen is doing it is not quantified. We wished to have an easily reproducible method to implement HEDE and HELP that was based on the same idea. The defactant mechanism is the framework, where hydrogen lowers the energy of defects, controlling the change through the chemical potential of hydrogen.

3.1.4 Other Mechanism

HEDE and HELP are not the only suggested mechanisms for hydrogen embrittlement. The reason we do not focus on the other is not due to a presumed smaller significance. As will be discussed later in the discussion for the thesis, all mechanism may be relevant. However, we do not implement them in this current study. These theories are briefly summarised below, including the reason for why they are not implemented.

Stress-induced hydride formation and cleavage are operative in systems where sufficient amounts of hydrogen activate the formation of brittle hydrides. This occurs at locations of high triaxial stresses, such as ahead of cracks, where they serve as obstacles to dislocations, decreasing fracture toughness significantly. Stress-induced hydride formation is not included as the pure iron systems at low gas pressures are usually considered to be non-hydride formers.

Adsorption Induced Dislocation Emission (AIDE) suggested that hydrogen enhanced dislocation nucleation at the crack tip, increasing crack growth due to dislocation emission. Lynch [55, 56, 57] has argued that in fracture of steels, it is often void nucleation and growth that is the dominant fracture mechanism. In this case, if hydrogen enhances dislocation emission, the crack tip would grow at an increased rate, connecting to voids at a faster rate. The voids would, therefore, have less time to grow and consequently appear smaller in the post-fracture analysis. This theory has its most significant effect when dislocation emission from the crack tip is insignificant in the no hydrogen case. Within the model in chapter 4, this is not the case, as dislocation emission from the crack is the primary plastic response to the load.

Hydrogen Enhanced Strain-Induced Vacancies (HESIV) [58, 59, 60, 61] postulates hydrogen's primary effect is the nucleation and stabilisation of vacancies. HESIV puts vacancies at the centre stage, arguing they are the primary reason for the embrittlement effect. Hydrogen has increased concentration at highly strained locations, and will, therefore, increase the vacancy concentration. A high concentration of vacancies can conglomerate, causing void nucleation and growth, leading to reduced load bearing area and crack formation. Again this mechanism is mostly relevant when the primary deformation mechanism is void nucleation and growth. Our simulation cases can not account for the phenomenon of void nucleation and growth.

3.2 Application of Hydrogen to Simulations

Hydrogen enters the material either during production or service. It distributes in equilibrium with the traps and lattice structure. The hydrogen atom exists in its atomic form, staying at interstitial sites; most often the tetrahedral sites in BCC.

Most experimental research presents their application of hydrogen as a function of the hydrogen gas pressure or chemical potential in the system. We will approach the presence of hydrogen in the same manner. The experimental work which is used as validation in this work use two different methods of applying hydrogen to a sample; hydrogen gas or chemically charging

using a glycerol-based electrolyte solution [62]. In both cases, hydrogen penetrates the material surface and spread into the bulk. Both can be addressed through a change to the chemical potential of hydrogen.

3.2.1 Gas Charging

During hydrogen gas charging, an equilibrium will be established between the gas, adsorbed hydrogen at the surface and absorbed hydrogen in the metal. The hydrogen gas will split into two atomic hydrogen atoms $H_2 \rightleftharpoons 2H^+ + 2e^-$. Hydrogen from the gas phase will form a monolayer on the surface Γ_{H} [63]. Hydrogen adsorbed at the surface layer penetrates the surface and absorbs into the bulk. The formation of the monolayer is fast, and changes to the gas phase will quickly affect the monolayer. In the event of introducing another element, such as oxygen gas, the oxygen will adsorb to the surface of the metal due to its lower energy state at the surface. Removing the hydrogen monolayer can be shown to remove the hydrogen effect [45].

The hydrogen bulk concentration is determined by the charging conditions p and T temperature. The chemical potential of a hydrogen gas $\mu_{H_2,g}$ is

$$\mu_{H_2,g} = \mu_g^0 + RT\log(p/p_0)\ , \tag{3.1}$$

where R is the gas constant and T is the temperature. p_0 is 10^5 Pa and $\mu_g^0 = 130.68T$ J/mol is the entropy change due to the degrees of freedom. The chemical potential can then be estimated for both the surface of a metal and its bulk by using an equilibrium

$$\mu_{H_2,g} = 2\mu_{H,s} = 2\mu_{H,b} \tag{3.2}$$

between the gas phase $\mu_{H_2,g}$, surface of the metal $\mu_{H,s}$ and the bulk concentration $\mu_{H,b}$. The diffusion kinetics of hydrogen in BCC are high, so achieving an equilibrium between gas phase, surface and bulk is assumed fast.

The chemical potential of hydrogen at the surface hydrogen can be connected using

$$\mu_{H,s} = \mu_{H,s}^0 + 2W\frac{\Gamma_H}{\Gamma_{sat}} + RT\log\left(\frac{\Gamma_H}{\Gamma_{sat}-\Gamma_H}\right)\ , \tag{3.3}$$

where Γ_H is the excess hydrogen at the surface and Γ_{sat} is the saturating value at roughly $\Gamma_{sat} = 2\times10^{-5}\mathrm{mol/m^2}$[63]. The $\mu_{H,s}^0$ is the standard value for the chemical potential of atomic hydrogen at the surface, set as $-6.84\mathrm{kJ/mol}$, and W is an hydrogen-hydrogen interaction energy parameter set as 0 for iron.

The bulk chemical potential $\mu_{H,b}$ can be found through

$$\mu_{H,b} = \mu_{H,b}^0 + RT\log(C(\vec{\boldsymbol{x}}))\ , \tag{3.4}$$

where $\mu_{H,b}^0$ is the standard value for chemical potential of atomic hydrogen in the bulk and $C(\vec{\boldsymbol{x}})$ is the hydrogen concentration per Fe atom dependent on position $\vec{\boldsymbol{x}}$. Assuming negligible internal stresses in the material before load, the hydrogen concentration is homogeneous $C(\vec{\boldsymbol{x}}) = C_0$ within the same phases. $\mu_{H,b}^0$ is calculated to be $63.9\mathrm{kJ/mol}$ based on gas pressures and hydrogen concentration from table 1 [64].

Using the explained relations and standard values for chemical potential, the hydrogen concentration before load can be estimated. By adding a load, one- has to account for the increased

hydrostatic stress σ_h which changes the local chemical potential and therefore the local hydrogen concentration. The hydrogen concentration $C(\vec{\boldsymbol{x}})$ is then dependent on this load from

$$C(\vec{\boldsymbol{x}}) = C_0 \exp\left(\frac{\sigma(\vec{\boldsymbol{x}})V_H}{RT}\right) , \tag{3.5}$$

where V_H is the macroscopic volume change per mol hydrogen. Using these equations, one can account for the effect of not only the initial hydrogen charging but also the load locally. This will be shown to be a vital contribution to the understanding of the hydrogen effect on crack growth in BCC iron.

3.2.2 Hydrogen Movement

Diffusible hydrogen moves along pathways between interstitial sites in the crystal lattice. The driving force for diffusion is the gradient of hydrogen concentrations[65] as an Arrhenius relation

$$D = D_0 \exp\left(-\frac{Q_D^0}{k_B T}\right) , \tag{3.6}$$

where Q_D^0 is the height of the activation barrier, D_0 is a prefactor, often assumed to be independent of the temperature T, and k_B is the Boltzmann constant. Both Q and D_0 are dependent on the intermetallic bonding, crystal structure and microstructure. In BCC hydrogen solubility is low, and diffusivity is high. In iron, coefficients are $Q_D^0 = 6.88$ kJ/mol and $D_o = 2.0x10^{-7}$ $\mathrm{m^2 s^{-1}}$ [66]. Vacancies, dislocations, grain boundaries, solutes, precipitates, inclusions and interfaces all serve as traps for H atoms[67, 68].

3.3 Effect of Hydrogen on Defects

This section will attempt to discuss some of the accumulated work in the field of the effect of hydrogen on defects. Specifically, focusing on defects presented in chapter 2, which are relevant to our current discussion. The review will start with the hydrogen effect on dislocations, and then discuss its effect on crack.

3.3.1 Dislocations and Plasticity

As mentioned earlier, there are experimental evidence suggesting that hydrogen promotes dislocation movement. This can be achieved through shielding (reducing) of the elastic stresses between dislocations or a change to their mobility.

The shielding effect has been discussed by Birnbaum and others [69, 70, 71], where it is argued that hydrogen lowers the elastic interaction between dislocations. How this is achieved is yet to be determined, with attempts at relating the hydrogen effect to dislocations through a hydrogen stress field [72, 73] or changes to the dislocation energy [74, 75]. One has to consider not only the case of edge, screw and mixed dislocation but also any metastable events such as junctions, kinks, jogs, cross slip and partial dislocation. By changing the energy of these defects, hydrogen could alter the plastic response significantly.

A change to the mobility of dislocations due to hydrogen would also change the plastic response of the material. In iron it is often suggested there should be one or several transitions between a softening and hardening effect. The hardening aspect in the case of iron, comes from hydrogen pinning of dislocation glide [53]. Hydrogen at the core of the dislocation lowers the energy of the dislocation [76]. The dislocation would have to break free of the hydrogen, similar to the Cottrell effect. This pinning is important in the case of edge dislocation glide and kink migration. The softening effect would arise as hydrogen can lower the formation energy of kink-pairs [77, 78]. This is important as the screw dislocation is the rate-dependent factor in deformation of iron. Lowering the formation energy of kink-pairs could lead to enhanced mobility. Though, due to the complex movement of kink-pair nucleation and migration, it is often concluded that the effect of hydrogen can be both a softening or a hardening effect. The transition between the two is dependent on the shear stress, temperature and concentration of hydrogen.

3.3.2 Cracks

The effect of hydrogen on cracks is not a simple matter. There are many types of cracks and different ways of loading them. One observed hydrogen effect in one system does not necessarily translate directly to another.

The overall effect of hydrogen on a tensile test of bcc Fe3wt%Si [79] indicates a reduction in the strain to fracture. A further study [80] into the fatigue crack growth behaviour of Fe3wt%Si showed a significant increase of the fatigue crack growth rate when hydrogen was added to the system. Post-fracture characterisation found reduced residual plastic zones and a brittle-like fracture feature termed ”quasi-cleavage”. A study on the fatigue crack growth in bcc iron [81] shows an enhanced crack growth rate due to hydrogen, reporting a less developed dislocation structure along the crack path. Changing the hydrogen gas pressure also leads to a change. The sharpness of the crack is dependent on the hydrogen gas charging [82], and Birenis et al. [81] found a correlation between gas pressure and the starting point for the enhanced fatigue crack growth rate. Mechanical testing at the microscale captures similar findings with an enhanced crack growth rate, reduced residual plastic zone and sharper cracks [83, 84, 85].

In summary, hydrogen enhances crack growth in such a way that the residual plasticity after fracture is less developed. The brittle like features and sharpening of the crack indicate a loss in fracture toughness and a higher gas pressure of hydrogen results in a more substantial embrittling effect.

Simulations using the Finite Element Method (FEM) with a cohesive zone model have been performed on loading tests in seawater under cathodic protection on single edge notched tension (SENT) specimens made from 25%Cr duplex stainless steel [86] and API X70 pipeline steel [87, 88, 89]. While these simulations do not exhibit the exact material and microstructure that will be simulated in this work, their work resulted in one crucial finding in regard to our simulation. Crack growth was recorded with the collapse of the first cohesive element at the crack tip surface and not at the point where the hydrostatic stress was at maximum. They identified that the accumulation of hydrogen at the crack tip due to the stress field of the crack could have a significant effect on the local hydrogen concentration.

A 2D analysis using discrete dislocations modelled the change in cleavage criterion at the crack tip with a change in the surface energies due to hydrogen segregation [90]. Results indi-

cate that hydrogen can promote crack growth alternating between mechanisms of cleavage and dislocation emission . They also found that higher hydrogen gas pressure changed the crack growth ratio between cleavage and dislocation emission. A higher gas pressure meant more crack growth through cleavage.

The results from atomistic simulations of the hydrogen effect show that hydrogen can have different effects depending on the crack system. Taketomi et al. found evidence for enhanced dislocation emission due to hydrogen[91]. Whereas Wen et al. [92] found that hydrogen suppresses dislocation nucleation at the crack tip. Song et al. [93] found no configurations which show a preference to atomic bond-breaking vs dislocation emission. Matsumoto et al. [74] found that hydrogen-related phenomena can occur depending on the boundary conditions and the initial conditions. Adlakha et al. [94] showed hydrogen's dual role in enhancing both dislocation emission and cleavage events. Our conclusion from these atomistic simulations is that hydrogen can have multiple effects, depending on the simulation setup, hydrogen concentration and crack system modelled. This varying behaviour does not mean that some are wrong or right. Instead, it alludes to that the hydrogen effect is system-specific.

Chapter 4

Crack Dislocation Dynamics

The influence of hydrogen on crack behaviour in ferritic steels indicates a sharpening of the crack and an enhanced crack growth rate. The current understanding of the hydrogen embrittlement mechanisms effect on the crack growth rate gives an incomplete picture. We will use a 2D Discrete Dislocation Dynamics model to examine the effect of hydrogen on a sharp crack under load by implementing different hydrogen mechanisms. The plastic work in the model is dependent on loading rate, dislocation mobility, dislocation multiplication and the cleavage criterion. The model is set to capture the build-up of hydrostatic stress at the crack tip, increasing the hydrogen concentration locally. We incorporate the proposed hydrogen mechanisms HEDE and HELP through the defactant framework. The aim is to determine which hydrogen mechanism can reproduce the sharpening of the crack and enhanced crack growth seen in experiments

We find that a change in elastic interaction between dislocations does not produce a sharper crack tip, the hydrogen effect on the cleavage criterion does. Lowering the surface energy of a crack decreases the cleavage criterion. A lowered cleavage criterion means a lower fracture toughness and sharper crack. These results are system-specific, and changes to the loading or charging conditions could alter the critical hydrogen effect.

4.1 Introduction

Hydrogen has a deterimental effect on Fe-3wt%Si, because it increases the growth rate of cracks [80]. How hydrogen enhances the crack growth rate is yet to be determined with a multitude of suggested mechanisms. This chapter investigates the influence of hydrogen on crack growth by implementing two possible hydrogen effects in a 2D simulation of the plastic response to loading of a crack. The intention is to see if either one of the two possible hydrogen effects, or a combination of the two, can replicate experimental trends found in the literature. As previously discussed in chapter 3, the role of hydrogen in deformation is complex, and the critical hydrogen effect can often be system-specific.

There are two experimental studies which we will base this study on, Vehoff & Rothe [45] and Wan et al. [80]. Both studies use a Single Edged Notched Tension (SENT) specimen of Fe-3wt%Si. In these studies, the microstructure features are simplified by working with monocrystalline, or similar samples. The effect of grain boundaries, precipitates and surface effects from the specimen surface are negligible. Vehoff & Rothe [45] studied the effect of

hydrogen on the ratio between the crack tip opening and the crack growth. They found that the crack growth ratio increased with increasing hydrogen gas pressures, i.e. a sharper crack. The sharpening due to hydrogen indicates that hydrogen enhances crack growth through promoting cleavage fracture. The second study [80] investigates the influence of hydrogen on a Fatigue Crack Growth (FCG) testing of a SENT specimen. The study found that hydrogen enhanced the crack growth rate. The critical factors in replicating the experimental work would be to find which hydrogen mechanism causes both enhanced crack growth rate and a sharpening of the crack.

The model we have chosen to investigate these studies is a 2D Discrete Dislocations Dynamics (DDD) model [95, 96, 2]. The simulation model is a quasi-static 2D DDD model of a crack in a continuum subject to a load. The load is applied normal to the crack plane, and the stress state of the crack tip is calculated in combination with a cleavage criterion. The model also includes dislocation emission from the crack tip. The emitted dislocations have a strengthening effect on the crack tip, lowering the stress state of the crack tip. The fracture toughness of the crack is the global load necessary to activate a cleavage fracture, which depend on the loading history.

This 2D model has been previously used to investigate the Brittle to Ductile Transition (BDT) in BCC metals [29]. The BDT describes a material phenomenon where the fracture toughness changes with the temperature. At low temperatures the BCC metal behaves in a brittle way, activating fracture with little to no plasticity. At high temperatures, the BCC metal behaves in a ductile way or exhibits a high strain fracture. Both ductile behaviour and high strain fracture are associated with high amounts of plasticity. The transition between the brittle and ductile behaviour can be a soft or sudden transition. This 2D model of a crack can correlate the BDT with the mobility of the dislocations, where the mobility is a function of temperature [20, 21, 22, 23]. The BDT can also depend on the loading conditions [97] and the microstructure [29].

The model was chosen due to its efficiency. There are other models of cracks under load, both 2D and 3D, which can offer higher levels of detail in the deformation process. However, this additional level of detail is often accompanied by increasing computational demands and additional complications that could affect the analysis. Our approach is intended to be as simple as possible. The complications and implementation biases we introduce needs to be as transparent as possible.

The model is detailed in section 4.2 without the effect of hydrogen. The effect and implementation of hydrogen is discussed in section 4.3, and the results are presented in section 4.4. The results and their implications are discussed in section 4.5 and the conclusions of the study are in section 4.6.

4.2 Simulation Model

The 2D DDD model simulates loading of a crack through describing the dynamics of dislocation emission and movement away from the crack tip. An external stress is applied to the simulation resulting in an applied stress intensity K^{a} on the crack. The applied stress intensity starts from zero and is increased over time with a rate of ΔK^{a}. The model differentiates the applied stress intensity (external load) and the local stress state of the crack tip, K^{L}. The 2D model include two types of events; dislocation emission and cleavage fracture, each with their

respective activation criterion. The criterion for dislocation emission is a critical resolved glide stress on point sources near the crack tip. Emitted dislocations move based on their mobility as a function of their resolved glide stress τ. The dislocations reduce the stress state of the crack tip through elastic interaction, referred to as shielding. A cleavage fracture is activated when the local stress state of the crack tip reaches or exceeds a cleavage threshold stress intensity K^{C}. Activation of a cleavage fracture ends the simulation.

This section will describe the model without the hydrogen effect. Features such as the dislocation multiplication, dislocation mobility and elastic interaction between defects are discussed in section 4.2.1. The simulation protocols more specific to the mechanical loading and boundary conditions are presented in section 4.2.2, and the numerical implementation of the model is presented in section 4.2.3.

4.2.1 Model Dynamics

A description of the implementation of dislocation emission from the crack tip is presented below, followed by the elastic interaction between defects in the simulation volume. The mobility of dislocations is covered at the end of this section. The shielding effect of dislocations on the crack and its consequences are discussed later, in section 4.2.2.

Dislocation Multiplication

In this subsection, the implementation of dislocation emission from the crack tip is introduced, together with the corresponding crack growth which occurs with every dislocation emission.

Dislocation generation occurs at source positions, where dislocation nodes are emitted when the shear stress is above a threshold. The criterion for dislocation emission from the point source is a critical resolved glide stress τ_{emission}. When the shear stress on a source is above the threshold, a dislocation is introduced gradually over a period t_{emission}. The gradual introduction of each dislocation is done by linearly increasing the magnitude of the Burgers vector to b_0 after t_{emission}. The stress on the dislocation source is a function of the stress field from the crack tip, the image stress and the stress from other dislocations. The dislocation emission parameters are presented in table 4.1.

The placement of these point sources affects the final results of the simulation. The placement of the point sources is determined by the crack system, corresponding blunting system and the number of defects along the crack front. The point sources emulate dislocation emission from crack tips. Defects along the crack front at a sufficient stress level can produce dislocation half-loops, see Fig. (4.1). Along the crack front, the half-loops will grow and intersect with other half-loops. The point sources are positioned to be where the half-loops combine into parallel straight edge dislocations. Each point source emulates one slip plane; in our case, we wish to recreate the double slip system seen in experiments. That means placing one point source above the crack plane, and one below the crack plane. Two parameters determine the location for a point source. The first is the angle between the crack and the slip planes. The second is the distance away from the crack.

The angle can be determined by finding which blunting plane is activated in the current crack system. There are many different crack systems, all behaving differently depending on the orientation to the global load, orientation to the grain it is embedded in and the surrounding

Property	**Symbol**	**Value**
Emission criterion [MPa]	τ_{emission}	40
Emission time [μs]	t_{emission}	1
Crack system		$(011)\,[0\bar{1}1]$
Blunting system		$(211)\,[\bar{1}11]$
Angle between the crack and slip planes [1]	θ	54.7
Distance away from the crack [1]	d	$5a$
Young's Modulus [GPa]	E	211
Shear Modulus [GPa]	G	82
Poisson's ration	ν	0.291
Lattice constant [nm]	a	0.2875
length of Burgers vector	b	$\sqrt{3}a/2$
Velocity prefactor [m/s]	v_0	40
Kink-pair formation energy [eV]	Q_{kp}	0.69
Activation volume for kink-pair formation	V_{act}	$25b^3$
Speed of sound in Fe [m/s]	$v_{\max}$	3000
Temperature [K]	T	300
Loading rate [MPa$\sqrt{m}$/s]	ΔK^{a}	1.0
Specimen width [mm]	W	6
Crack length [mm]	a_c	0.5
Geometrical factor	$\text{f}(\text{a}_\text{c}/\text{W})$	1.18
Surface energy [2][J/m^2]	γ_s^0	2.41
Standard value absorbed hydrogen [kJ/mol]	$\mu_{\text{H,b}}^0$	63.9
Macroscopic volume change [m^3/mol]	V_H	$2.1e-6$
Excess hydrogen at dislocations [mol/m]	Γ_{disl}	8.1×10^{-15}
Saturation of excess hydrogen at surface [3][mol/m^2]	Γ_{sat}	2.65×10^{-5}
Hydrogen interaction energy [J]	W_H	0

[1] Parameters related to the dislocation source positions
[2] Surface energy of a (110) surface in pure iron without hydrogen [98].
[3] Density of surface sites in Fe for adsorption of Hydrogen [99].

Table 4.1: Fixed parameters for a simulation of a monocrystalline Fe-3wt%Si Single Edge Notched Tension (SENT) specimen.

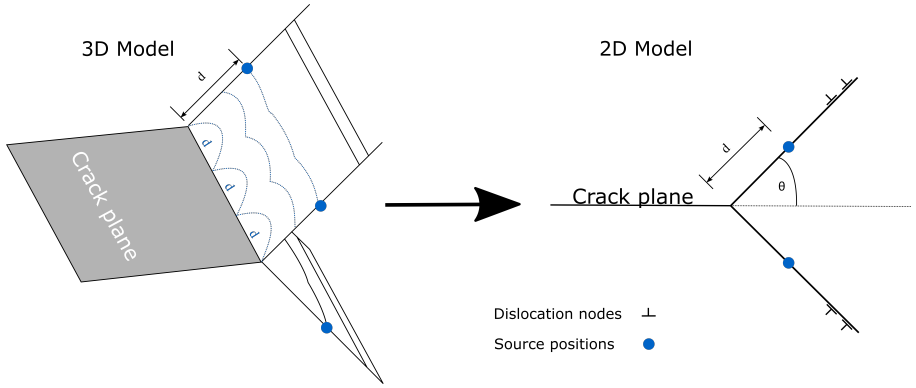

Figure 4.1: Defects along the crack front produce dislocation half-loops which combine to give parallel straight edge dislocations on the slip plane. The 3D model can, therefore, be represented in a 2D framework.

microstructure. In this work, due to the complexities of hydrogen embrittlement and its implementation, we will not delve into the previously mentioned parameters. For simplicity, only the single crack system $(011)\,[0\bar{1}1]$ with the blunting system $(211)\,[\bar{1}11]$, is discussed here. The crack system emulates the orientations and microstructure in the experimental system in Vehoff and Rothe [45]. One source is positioned at an angle θ to the crack plane, and a second one at an angle $-\theta$ to the crack plane. With this chosen setup, the dislocation configuration will develop in two slip bands, one set of dislocations above and one below the x_1 axis.

The second parameter d determines at which distance away from the crack at an angle θ the source positions will be placed. The distance d is obtained from an estimation of the average distance between irregularities or defects along the crack front. These defects along the crack front are nucleation points for dislocation half-loops, as shown in Fig. (4.1). The distance d is then where the half-loops collapse into a straight dislocation. This second parameter has a significant effect on the final fracture toughness of the system. The further away from the crack tip the source position is, the lower the fracture toughness. As to the author's knowledge, there is no good way of determining the number of defects along the crack front. The distance d has been chosen to be as close to the crack tip without introducing too much added numerical complications for the calculation. The chosen angle θ and distance d is found in table 4.1.

The generated dislocations are nodes, with an infinite line direction parallel to the crack front at the origin x_3, illustrated in Fig. 4.2. The position of dislocation l is a complex variable ζ_l where the real part is its position along the x_1 axis and the imaginary part is its position along the x_2 axis. The Burgers vector for the dislocations is denoted $\vec{\boldsymbol{b}}$ and it is parallel to the slip plane. The Burgers vector $\vec{\boldsymbol{b}}$ is determined by its length b and the chosen slip systems which is activated at the crack tip, see table 4.1.

Each emitted dislocation will introduce a slip on the crack tip, i.e. the crack tip will be shifted in space. The shift in space of the crack tip is the Burgers vector $\vec{\boldsymbol{b}}$ of the emitted dislocation. The crack tip grows (along x_1), where the growth per dislocation emission is equal to $\vec{\boldsymbol{b}}_{x_1}$, the component of $\vec{\boldsymbol{b}}$ along the x_1 direction. The crack opens (x_2) $\vec{\boldsymbol{b}}_{x_2}$ from each emitted dislocation. This is important in relation to the experimental findings of a sharper cracks.

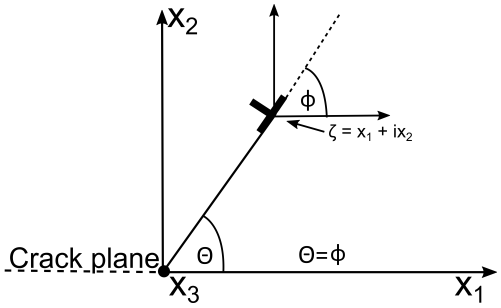

Figure 4.2: Coordinate system for the crack and the dislocations. The crack tip is at the origin with cleavage plane along the negative x_1 axis. The x_3 axis is normal to the paper. The dislocation is at position ζ_l, described by a complex variable $\zeta = x_1 + ix_2$. i is the imaginary number

The crack growth and opening is the sum of the Burgers vector $\vec{\boldsymbol{b}}$ from the number (N_D) of dislocations emitted from the crack tip.

The crack growth ratio a_n is an estimation of the ratio between the total crack growth Δa and $\Delta\delta$ crack opening. The longer the crack growth is compared to the crack opening, the higher the crack growth ratio. A higher crack growth ratio means a sharper crack tip. The crack growth ratio is

$$a_\mathrm{n} = 2\frac{\Delta a}{\Delta\delta} = 2\frac{\Delta a_\mathrm{d} + \Delta a_\mathrm{c}}{\Delta\delta_\mathrm{d}} \,, \tag{4.1}$$

where Δa is the sum of the crack growth through dislocation emission Δa_d and cleavage fracture Δa_c. $\Delta\delta_\mathrm{d}$ is the crack opening due to dislocation emission.

As an example, with the current blunting system one dislocation emitted from the crack tip ($N_\mathrm{D} = 1$) will grow the crack $\Delta a_\mathrm{d} = N_\mathrm{D}\vec{\boldsymbol{b}}_{x_1} = 0.144$ nm, and open the crack $\Delta\delta_\mathrm{d} = N_\mathrm{D}\vec{\boldsymbol{b}}_{x_2} = 0.203$ nm. The crack growth ratio is then $a_\mathrm{n} = 1.42$, and the crack opening angle would be $\alpha = 2\,\mathrm{arccot}\, a_\mathrm{n} = 70.45$.

Increasing the amount of dislocations emitted from the crack tip will increase the growth through dislocation emission. Four thousand dislocations emitted from the crack tip ($N_\mathrm{D} = 4000$) would give a crack growth of $\Delta a_\mathrm{d} = N_\mathrm{D}\vec{\boldsymbol{b}}_{x_1} = 575.51$ nm, and open the crack $\Delta\delta_\mathrm{d} = N_\mathrm{D}\vec{\boldsymbol{b}}_{x_2} = 812.82$ nm. The increased amount of dislocation emission results in a crack growth ratio of $a_\mathrm{n} = 1.42$, the same as with one dislocation. As long as the crack growth is dominated by dislocation emission and the same slip systems, the crack growth ratio will remain the same.

Activating a cleavage fracture, will grow the crack, contributing to the crack growth Δa, but not to the crack opening $\Delta\delta$. With a crack growth through emission of dislocations and a cleavage fracture, the crack growth ratio will increase. In the case of $N_\mathrm{D} = 4000$ and a cleavage growth of $\Delta a_\mathrm{c} = 400$ nm, the crack growth ratio would be $a_\mathrm{n} = 2.4$.

Elastic interaction between the crack and the dislocations

The force fields used in this model are developed by Lin & Thomson [2], where the crack and dislocations are singularities embedded in an isotropic elastic field. The force fields assumes that the defects only interact in an elastic way, meaning that any nonelastic interaction is neglected. The effective force on a dislocation is the summed contribution from all other defects,

plus a correction for the surface at the crack and the external load. The resolved glide stress used to estimate the mobility of the dislocations is computed by the Peach-Kohler equation. The effective forces on a dislocation node can be grouped into four terms,

$$f = f^{\mathrm{c}} + f^{\mathrm{img}} + f^{\mathrm{dd}} + f^{\mathrm{ext}}. \tag{4.2}$$

f^{c} is the force field of the crack, f^{img} is the image force from the crack surface, f^{dd} is the forces between dislocations and f^{ext} is the force due to the external loading. For the equations presented below, the crack tip is at the origin, with the crack plane along the negative x_1-axis. The elastic interaction of dislocations on the crack tip and their strengthening effect is discussed in section 4.2.2.

Three of the four terms presented in Eq. (4.2) is described by the framework developed by Lin & Thomson [2]. These three terms are the force field of the crack f^{c}, the image force from the crack surface f^{img} and forces between dislocations f^{dd}. The three forces are complex numbers indicating the force in x_1 and x_2 with its real and imaginary part, respectively. The force on a dislocation due to the crack is presented below, followed by the image force and the forces due to other dislocations. The force term due to external load f^{ext}, which is not a part of the Lin & Thomson [2] framework, is discussed last.

The force from the crack f_l^{c} on dislocation l is the main driver for the plastic work. The force from the crack is a result of the loss off load-bearing area due to the crack. $f_{\mathrm{l}}^{\mathrm{c}}$ is repulsive on a shielding dislocation, while attractive to an anti-shielding dislocation. The force from the crack is

$$\bar{f}_l^{\mathrm{c}} = \frac{1}{2i\sqrt{2\pi\zeta_l}}\left(K_{I,II}^{\mathrm{a}} b_l - \bar{K}_{I,II}^{\mathrm{a}} b_l + \bar{K}_{I,II}^{\mathrm{a}} b_l \frac{\zeta_l + \bar{\zeta}_l}{2\zeta_l} - \bar{K}_{I,II}^{\mathrm{a}} \bar{b}_l\right) + \frac{K_{I,II}^{\mathrm{a}} \bar{b}_l}{2\sqrt{2\pi\bar{\zeta}_l}}. \tag{4.3}$$

where the Bar notation, i.e. $\bar{f}_l^{\mathrm{c}}$, indicates the complex conjugate. ζ_l is a complex number representing the position of dislocation l, where the real part is x_1 and imaginary part is x_2. b_l is a complex number representing the Burgers vector $\vec{\boldsymbol{b}}$ of dislocation l, where the real and imaginary part represents x_1 and x_2, respectively. The load on the crack tip is expressed in terms of a stress intensity factor $K_{I,II}^{\mathrm{a}}$, this is the external load previously referred to as K^{a}. The subscript I and II denotes two different types of loading of a crack. The stress intensity factor $K_{\mathrm{I,II}}^{\mathrm{a}}$ is a complex variable, where the real part is Mode I loading, and the imaginary part is Mode II. The third mode of loading, Mode III is also included in this framework, however, our work only includes mode I loading. The terms for Mode III loading $K_{\mathrm{III}}^{\mathrm{a}}$ are removed to simplify the presentation of the equations.

Briefly explained these Modes of loading described different ways of loading a crack. Loading a crack can include either just one or a combination of them. Mode I loading occurs when a load is applied normal to the crack plane, and leads to crack opening. Mode II is an in-plane shear, which is a shear parallel to the x_2 axis. Mode III is an out-of-plane shear, parallel along the x_3 axis. Mixed-mode loading is not explored in this work, and the loading will always be Mode I.

The next equation is the image force, and is a results of the free surface of the crack. This term is quadratic in b and is always attractive towards the crack surface. The term is a force field which enforces zero traction at the surface at the crack tip due to dislocation l. The image

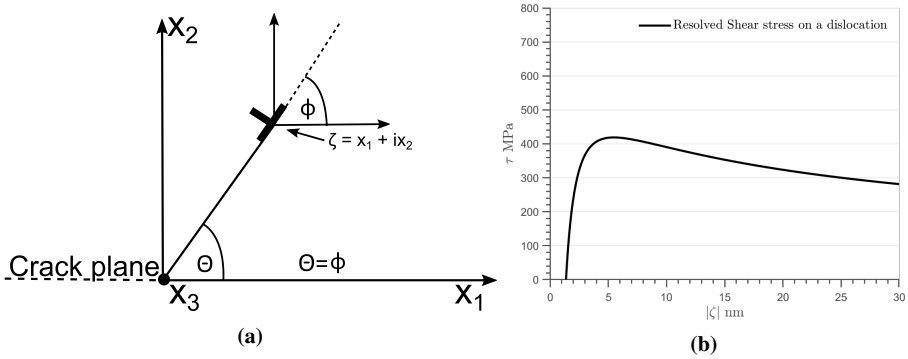

Figure 4.3: The resolved glide stress τ on a dislocation when there are no other dislocations around at an applied stress intensity of $K_{\mathrm{I}}^{\mathrm{a}} = 0.4285\ \mathrm{MPa}\sqrt{\mathrm{m}}$. The applied stress intensity $K_{\mathrm{I}}^{\mathrm{a}}$ is the point where the first dislocation is nucleated without the effect of hydrogen.

force can be calculated from

$$\bar{f}_l^{\mathrm{img}} = -\frac{G}{4\pi(1-\nu)}\Big(\frac{b_l^2\sqrt{\bar{\zeta}_l}}{4\zeta_l^{3/2}}\left(\sqrt{\bar{\zeta}_l/\zeta_l}+1\right) + \frac{b_l\bar{b}_l}{4}\left(\frac{3}{\zeta_l}+\frac{1-\bar{\zeta}_l/\zeta_l}{2\sqrt{\zeta_l\bar{\zeta}_l}}+\frac{3-\sqrt{\bar{\zeta}_l/\zeta_l}}{\sqrt{\zeta_l}(\sqrt{\zeta_l}+\sqrt{\bar{\zeta}_l})}-\frac{\bar{b}_l^2}{4\bar{\zeta}_l}\left(1+\sqrt{\bar{\zeta}_l/\zeta_l}\right)\right)\Big). \quad (4.4)$$

Here, G is the shear modulus and ν the Poisson's ratio, values are given in table (4.1). The force of the crack and the image force from the crack tip affects the emission of dislocations and the final fracture toughness. The two terms are presented in Fig. (4.3b), where they are converted to the resolved glide stress on a dislocation at a varying distance away from the crack at an angle θ. The resolved glide stress on a dislocation shown in Fig. (4.3b) gives an indication of how the emission parameter d can influence the fracture toughness of the system. The shear stress due to the image term is weaker the further away from the crack tip. A dislocation source position further away from the crack will emit dislocations at a lower stress state of the crack. A lower stress state of the crack tip for emission activates plasticity at a lower load, but it does not results in a higher fracture toughness. The critical factor for the final fracture toughness in this model is the ability for dislocations to escape the region close to the crack tip.

Lastly, the force from dislocation j onto dislocation l,

$$\begin{aligned}\bar{f}_l^{dd} = \frac{G}{8\pi(1-\nu)}\Bigg(&\left(b_l b_j + \bar{b}_l b_j + b_l \bar{b}_j\right)\left(\frac{\sqrt{\zeta_j/\zeta_l}+1}{\xi_1} + \frac{\sqrt{\bar{\zeta}_j/\zeta_l}-1}{\xi_2}\right)\\ &- \bar{b}_l \bar{b}_j \left(\frac{\sqrt{\bar{\zeta}_j/\bar{\zeta}_l}+1}{\bar{\xi}_1} + \frac{\sqrt{\zeta_j/\bar{\zeta}_l}-1}{\bar{\xi}_2}\right) - 2ib_l b_j y_1 \left(\frac{\sqrt{\zeta_j/\zeta_l}+1}{\xi_1^2} + \frac{\sqrt{\bar{\zeta}_j/\zeta_l}-1}{\xi_2^2}\right)\\ &+ \frac{ib_l b_j y_2}{\xi_1^2}\left(\sqrt{\frac{\zeta_j}{\zeta_l}} + \sqrt{\frac{\zeta_l}{\zeta_j}} + 2\right) - \left(\frac{iy_2(b_l\bar{b}_j + b_l\bar{b}_j)}{\xi_2^2} + \frac{4b_l\bar{b}_j y_1 y_2}{\xi_2^3}\right)\left(\sqrt{\frac{\bar{\zeta}_j}{\zeta_l}} + \sqrt{\frac{\zeta_l}{\bar{\zeta}_j}} - 2\right)\\ &- \frac{iy_2\bar{b}_l b_j}{\bar{\xi}_2^2}\left(\sqrt{\frac{\bar{\zeta}_j}{\zeta_l}} + \sqrt{\frac{\zeta_l}{\bar{\zeta}_j}} - 2\right) - \frac{ib_l b_j y_1}{\zeta_l^{3/2}}\left(\frac{\sqrt{\zeta_j}/\xi_1 + \sqrt{\bar{\zeta}_j}}{\xi_2}\right) + \frac{b_l\bar{b}_j y_1 y_2}{\xi_2^2\zeta_l}\left(\sqrt{\frac{\zeta_l}{\bar{\zeta}_j}} - \sqrt{\frac{\bar{\zeta}_j}{\zeta_l}}\right)\Bigg)\end{aligned}$$

$$\xi_1 = \zeta_l - \zeta_j; \xi_2 = \zeta_l - \bar{\zeta}_j; y_1 = \frac{\zeta_l - \bar{\zeta}_l}{2i}; y_2 = \frac{\zeta_j - \bar{\zeta}_j}{2i}. \quad (4.5)$$

Equation 4.5 shows the effective force from dislocation j onto dislocation l. b_j is a complex number representing the Burgers vector of dislocation j. ζ_j is the complex number representing the position of dislocation j.

The external force f^{ext} is a function of the applied stress,

$$f^{\text{ext}} = \tau b. \quad (4.6)$$

τ is the resolved glide stress on the dislocation as a function of the applied stress σ. Close to the crack tip the forces from the crack dominates, and the external force is negligible compared to these forces. When the dislocations move further away from the crack tip this changes, and the external force has a more significant impact on the effective force on the dislocation nodes.

Dislocation Mobility

The velocity of the dislocation nodes are determined by a phenomenological equation as a function of their resolved glide stress. The velocity equation used in this model is an approximation of the movement of a screw dislocation through kink-pair nucleation and migration. Capturing the real atomistic scale movement of screw dislocations means simulating events at time scales which are too small for this simulation. The velocity of a dislocations node is instead found by calculating its resolved glide stress and inputting the resolved glide stress into a phenomenological velocity equation. There are several available phenomenological velocity equations for a BCC material. In our current model, we have chosen an approach that estimates the mobility of screw dislocations in BCC materials. Screw dislocation movement is often considered to be the rate dependent factor for plastic deformation in BCC materials, which is why it is chosen here.

It is important to note that while we describe the kinetics of movement through the kink-pair nucleation and migration, these features are not simulated in the model. A brief introduction into the relevant features of screw dislocation movement through kink-pair nucleation and migration is offered below. A more in-depth description of the different regimes and derivation of the velocity equation used in this work is presented in section 2.1.2.

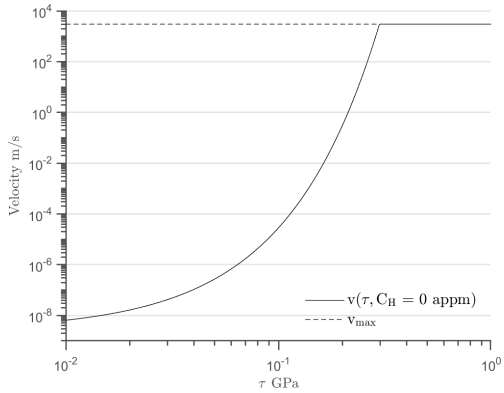

Figure 4.4: Dislocation velocity as a function of the resolved glide stress τ

The screw dislocation moves by the formation of one or several kink-pairs, and subsequent lateral movement of the kink edges, known as migration. The kink-pair nucleation and migration phenomenon has different regimes and behaviours dependent on the ease of kink-pair nucleation and kink migration. There are two regimes of significant. In regime 1 kink-pair nucleation is the rate-determining step, whereas in regime 2 it is the kink-migration. Which of these two regimes are active depends on parameters such as temperature and the resolved glide stress. In this current work, the velocity equation chosen applies to regime 2 of kink-pair nucleation and migration.

In regime 2, kink-pairs are easily nucleated and stable. Movement is achieved through kink edge migration and annihilation when meeting an opposite edge segment. Assuming regime 2 applies for all cases of nodal velocity during the simulation is a simplification. The high stresses close to the crack tip, ignoring the possibility of pure glide, would indicate a rate dependence on kink-pair nucleation instead of kink migration. However, to avoid sampling different velocity equations during integration steps, regime 2 has been assumed for all cases.

The velocity of a dislocation node is a function of its resolved glide stress τ found through

$$v(\tau) = v_0 \exp\left(-\frac{Q_{\mathrm{kp}}}{k_B T}\right) \exp\left(\frac{\tau V_{\mathrm{act}}}{k_B T}\right). \tag{4.7}$$

v_0 is double the kink speed v_{k}. Q_{kp} is the kink-pair formation energy, V_{act} is the activation volume for kink-pair formation, k_B is the Boltzmann constant and T is the temperature. The velocity Eq. (4.7) is more thoroughly discussed in section 2.1.2, and the velocity parameters are shown in Table 4.1. The values in Table 4.1 are chosen to replicate the velocity reported in Table 1 for screw dislocation in pure iron [100].

The velocity of the dislocation nodes has a max speed $v_{\max}$. The dislocation velocity as a function of the resolved glide stress is presented in Fig. 4.4. Note the cutoff at ≈ 0.5 GPa. The calculated dislocation velocity is never allowed to be higher than the speed of sound in iron which is roughly $v_{\max} = 3000$ m/s.

4.2.2 Mechanical Loading

The mechanical test emulated in this study is a Single Edge Notched Tension (SENT) specimen. The parameters related to the loading conditions are meant to reproduce the loading conditions in the work of Vehoff&Rothe [45]. The simulation approximates the experiment [45] by applying a tensile stress normal to a simulated sharp crack. Any shear occurring due to lattice rotation or from dislocations are neglected. The mechanical loading of the crack and the boundary conditions are explained first. The cleavage criterion is explained along with the shielding effect of the dislocation configuration.

The simulation volume is an infinite continuum, without any stored dislocations, grain boundaries, precipitates or surface. The tests specimen in Vehoff&Rothe [45] are large well annealed monocrystalline samples. These monocrystalline samples have a low dislocation density, and no grain boundaries or precipitates. The surface effects in these cases can be neglected without affecting the system considerably.

The loading in the model is an applied stress intensity K^{a}, which is a function of the tensile stress σ. The loading in this model will only include Mode I loading, i.e. $K_{\mathrm{I}}^{\mathrm{a}}$. The conversion between the stress intensity factor and tensile stress is dependent on which mechanical loading we are emulating, in this case the SENT specimen. The applied stress intensity is

$$K_{\mathrm{I}}^{\mathrm{a}} = \sigma f(a_{\mathrm{c}}/W)\sqrt{\pi a_{\mathrm{c}}}\,, \tag{4.8}$$

where $K_{\mathrm{I}}^{\mathrm{a}}$ is the real part of the K^{a}. The applied stress intensity is a Mode I loading ($K_{\mathrm{I}}^{\mathrm{a}}$) because the tensile stress is normal to the crack plane, no shear is introduced. The pure mode I loading means that the complex part of K^{a} is zero at all times. a_{c} is the original crack length and $f(a_{\mathrm{c}}/W)$ is an empirical factor used to model specific geometries. W is the width of the specimen. For the SENT specimen the empirical factor used is

$$f\left(\frac{a_{\mathrm{c}}}{W}\right) = \sqrt{\frac{2W}{\pi a_{\mathrm{c}}}\tan\left(\frac{\pi a_{\mathrm{c}}}{2W}\right)}\frac{0.752 + 2.02\dfrac{a_{\mathrm{c}}}{W} + 0.37\left(1-\sin\left(\dfrac{\pi a_{\mathrm{c}}}{2W}\right)\right)^3}{\cos\left(\dfrac{\pi a_{\mathrm{c}}}{2W}\right)}. \tag{4.9}$$

The empirical factor is specific to the mechanical tests and depend on the relation between the crack length a_0 and width (W) of the testing sample. The tensile stress σ is then converted to a resolved glide stress in the glide direction τ and added on to the resolved glide stress..

The loading of the crack emulates an monotonic loading of the specimen, where the rate of loading is ΔK^{a}. The loading rate applied to the simulation is given in table 4.1.

The fracture toughness of the simulated specimen is found by increasing the applied stress intensity K^{a} at a rate of ΔK^{a} until a cleavage event is activated. The cleavage event is activated when the stress state of the crack tip K^{L} exceeds a cleavage threshold K^{C}. The criterion for cleavage depends on the elastic strength of the bonds at the crack tip and the shielding effect of the surrounding dislocation configuration. The elastic strength of the crack tip is found by using the Griffith criterion for cleavage.

The cleavage criterion is $K_{\mathrm{I}}^{\mathrm{L}} \geq K_{\mathrm{I}}^{\mathrm{C}}$. The threshold $K_{\mathrm{I}}^{\mathrm{C}}$ relates the energy needed for an atomic-bond fracture to the formation energy of the surface created by the cleavage. The cleavage threshold is

$$K_{\mathrm{I}}^{\mathrm{C}} = \sqrt{\frac{2E\gamma_{\mathrm{s}}}{1-\nu^2}}. \tag{4.10}$$

E is the Young's modulus and γ_{s} is the surface energy. The key parameter in this threshold is the surface energy, and is where we will be introducing the hydrogen effect on the cleavage criterion. Without hydrogen the surface energy $\gamma_{\mathrm{s}} = \gamma_{\mathrm{s}}^0$, where γ_{s}^0 is based on the surface energy of a (110) surface in pure iron [98]. The hydrogen effect will be an independent term added to the γ_{s}^0, how that is done is detailed in section 4.3.2. A reduced surface energy along the cleavage path in this case means a reduced cleavage criterion $K_{\mathrm{I}}^{\mathrm{C}}$.

Dislocations are emitted from the crack tip before the cleavage criterion is met in Fe-3wt%Si. The shielding effect from the emitted dislocations reduce the stress state of the crack tip. This shielding effect can have a considerable affect on the fracture toughness.

The shielding effect is implemented through a relation between the applied stress intensity and the local stress intensity at the crack tip,

$$K^{\mathrm{L}} = K^{\mathrm{a}} - \sum_{l=1}^{N} k^{\mathrm{l}}. \tag{4.11}$$

K^{L} is the stress intensity of the crack tip and $\sum_{i=1}^{N} k_i^d$ is the shielding effect on the crack tip from the dislocation configuration. The dislocation configuration shields the crack tip by having a counteracting effect on the loading so that the local stress intensity is always smaller than the applied global stress intensity.

The shielding effect of dislocations describes how dislocations can impact the strains on the bonds at the crack tip. The following equation is exactly this effect, where the shielding of a dislocation depends on the position and the Burgers vector of the dislocation. The shielding effect can be found from

$$k^{\mathrm{l}} = \frac{G}{2i(1-\nu)\sqrt{2\pi}} \left(\frac{b_l}{\sqrt{\bar{\zeta}_l}} + \frac{b_l}{\sqrt{\bar{\zeta}_l}} + \frac{\bar{b_l}\left(\zeta_l - \bar{\zeta}_l\right)}{2\bar{\zeta_l}^{3/2}} \right), \tag{4.12}$$

where k^{l} is the impact of dislocation l on the stress intensity at the crack tip. The screw component is omitted in Eq. 4.12 as we only consider mode I loading.

4.2.3 Numerical Implementation

The numerical implementation of the 2D DDD simulation model is written in FORTRAN with parallelised (OpenMP) calculation of the elastic interaction between dislocations. The code is written using the code from Hartmaier and Gumbsch [25] as a guideline. The simulation results presented in this work has been run on a Intel Xeon Processor E5-2630 v4 [1], using the Intel Fortran $v2019$ compiler. The code implementation using the intel compiler was tested against the gfortran $v4.8.5$ compiler, leading to numerical rounding off errors only.

The structure of the code is illustrated in the flow chart in Fig 4.5. The iterative scheme starts with checking for nucleation and cleavage events. As long as a cleavage event is not activated, the simulation continues with integrating the dislocation positions due to their resolved glide stress. The position of the dislocations is integrated in time by using a time step adaptive 2nd ordered Runge Kutta (RK) algorithm. The time step is adapted to the ensures that the fastest dislocation during the first or second RK step never travels further than one lattice position per integration step. The max travel distance per iteration reduces the error occurring due to the

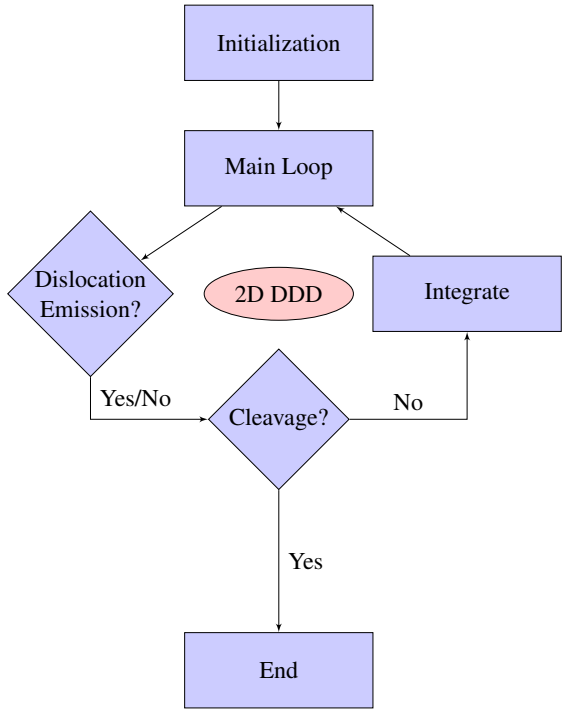

Figure 4.5: A flowchart representing the numerical implementation of the 2D DDD simulation.

high strain gradients and ensure that dislocation nodes do not pass each other. When the time step is accepted, the dislocation configuration is integrated. The iterative scheme returns to the checks for dislocation emission and cleavage events.

Numerically, the computations for these simulations are heavy for several reasons. First, the elastic interaction between the dislocations are long-ranged, and so the interaction between dislocations must account for all other dislocations. The second is the inaccuracy of the force fields when the defects are within a few lattice parameters of each other. Thirdly, the stress gradients from the defects are large. Lastly, the number of dislocation nodes are increasing with increasing load. The three first introduces situations where the time step size must be reduced to the size of nanoseconds. The final problem makes estimations of the full wall time of the simulations difficult to predict.

There are a few methods which could solve these numerical problems in future work. One method is using super dislocations, where several dislocations are grouped as one single large dislocations. This method can significantly cut down computation time, as it reduces the number of dislocation nodes. While inaccurate close to the super-dislocation, the long-range elastic interaction can be less impacted if carefully implemented. The second method is a neighbour method, where there is a list for every dislocation node. The list includes all other dislocation nodes and categorises them into two different categories. Those that are within a threshold distance, and those that are not. At integration steps when time steps are smaller than a time step threshold, the elastic interaction from dislocation nodes that are outside the threshold distance,

would not be updated.

4.3 Hydrogen Effect

Hydrogen is attracted to regions under tensile hydrostatic stress. A crack subject to a load will attract hydrogen, either from interstitial hydrogen of the bulk or hydrogen present at the crack surface. In this work, we will attempt to investigate the impact of hydrogen on a sharp crack in BCC iron under load.

The hydrogen is applied through a chemical potential to emulate gas charging of hydrogen gas H_2. The chemical potential for the hydrogen gas μ_{H_2} can be found through Eq. (3.1), as a function of the gas pressure p_{H_2}. A gas pressure of 1 kPa and 10 kPa results in a chemical potential of the hydrogen gas at 27.72 and 33.46 kJ/mol, respectively.

The relation between the chemical potential of the hydrogen gas and atomic hydrogen at the surface and in the bulk is $\mu_{H_2} = 2\mu_{H,s} = 2\mu_{H,b}$, where $\mu_{H,s}$ is the chemical potential of hydrogen at the surface, and $\mu_{H,b}$ is the chemical potential of hydrogen in the bulk.

The hydrogen effect on crack growth will be tested in this chapter by lowering the energy of defects through the defactant framework [51, 52]. The defactant framework reduces the energy of a defect γ_{defect} in the lattice. The change in energy is depends of the excess hydrogen Γ_{H} and chemical potential of hydrogen $d\mu_{\text{H}}$ at the defect. The defactant framework is

$$d\gamma_{\text{defect}} = \Gamma_{\text{H}} d\mu_{\text{H}}. \tag{4.13}$$

This investigation on the hydrogen effect on crack growth applies the defactant framework on the crack surface energy and the dislocation line energy. Lowering the energy of these two defects are meant to replicate the hydrogen mechanism HELP and HEDE.

The reduction in the energy of the defects is determined by the local chemical potential of hydrogen μ_{H} at the defect. The excess hydrogen at the defect Γ_{H} is set as a fixed value, dependent on the charging conditions. The chemical potential of hydrogen in the simulation volume is determined by

$$\mu_{H,b} = \mu^0_{H,b} + RT \log(C(\zeta)), \tag{4.14}$$

where $\mu^0_{H,b}$ is the standard value for chemical potential of atomic hydrogen in the bulk and R is the gas constant. $C(\zeta)$ is the hydrogen concentration dependent on position ζ. The slow loading rate and high diffusion speed of hydrogen in iron [66] allow hydrogen to acquire equilibrium with the current hydrostatic stress quickly. The kinetics of hydrogen diffusion is neglected, and the hydrogen concentration $C(\zeta)$ is given by

$$C_{\text{H}}(\zeta) = C^0_{\text{H}} \exp\left(\frac{\sigma(\zeta) V_H}{RT}\right). \tag{4.15}$$

Here V_{H} is the macroscopic volume change per mol hydrogen. C^0_{H} is the bulk concentration of hydrogen. The bulk concentration of hydrogen is dependent on the charging conditions, and is $C^0_{\text{H}} = \exp((0.5\mu_{H_2} - \mu^0_H)/RT)$. The final hydrogen concentration C_{H} and the chemical potential of hydrogen $\mu_{\text{H,b}}$, depend on the local hydrostatic stress σ_{h}.

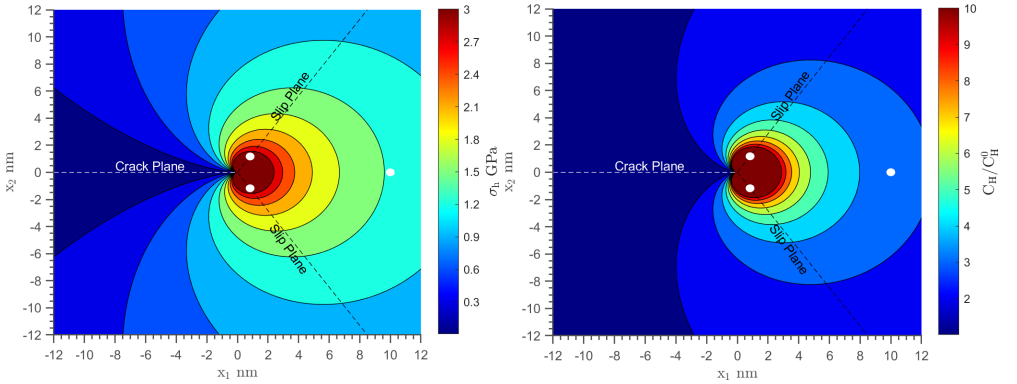

(a) Hydrostatic stress **(b)** Hydrogen Concentration ratio

Figure 4.6: The hydrostatic stress and corresponding hydrogen concentration ratio at a specific local stress intensity factor, $K_{\mathrm{I}}^{\mathrm{L}} = 0.4285$. The crack plane, cleavage point and the two slip planes with their corresponding point source positions are drawn in both figures. The dislocation point sources are the circles along the slip planes, while the cleavage point is along the positive x_1 axis. The take away from these two figures are that the most significant increase to hydrogen concentration is close to the crack tip. Please also note that b) is the ratio of hydrogen concentration C_{H} compared to the base hydrogen concentration C_{H}^0. At low hydrogen gas pressures p_{H_2}, $C_{\mathrm{H}}^0 << 1$ appm.

The hydrostatic stress is calculated using the Griffith-Inglis equation for Mode I load of a near field infinite crack [101]. The stress field of the crack varies greatly within the simulation volume. The hydrostatic stress at position ζ is

$$\sigma_h = K_{\mathrm{I}}^{\mathrm{L}} \cos(\psi/2) \frac{1+\nu}{\sqrt{2\pi|\zeta|}}. \tag{4.16}$$

The position is represented through the angle ψ between the position and the x_1 axis and the distance to ζ. As ζ is a complex variable, the absolute value determines the distance away from the crack tip. $K_{\mathrm{I}}^{\mathrm{L}}$ is the momentary mode I local stress intensity factor at the crack tip, which is the real part of $K_{\mathrm{I,II}}^{\mathrm{L}}$ (section 4.2.1). The hydrostatic stress is a function of the stress state of the crack tip. The momentary differences in hydrogen concentration due to stress field of the dislocations are not included.

The application of the hydrogen effect is applied through the defactant framework Eq. (4.13). The excess hydrogen Γ_{H} in these simulations are fixed based on the defect and the charging conditions, and given later in section 4.3.1 and 4.3.2. The chemical potential of hydrogen at the defect is found through Eq. (4.14). The charging condition is C_{H}^0 and the local hydrogen concentration due to the local hydrostatic stress is represented through $C(\zeta)$. The chemical potential of hydrogen at a dislocation is found by calculating the hydrostatic stress σ_{h} at the position ζ_l of dislocation l. The hydrostatic stress is then used to find the change in the local concentration of hydrogen $C(\zeta)$ and inputted into Eq. (4.14).

The position sampled for the hydrostatic stress for the cleavage criterion is taken along the cleavage path. The cleavage position is indicated in Fig. (4.6), alongside the dislocation source positions. Figure (4.6) shows the hydrostatic stress in Fig. (4.6a) and ratio of change in hydrogen concentration in Fig. (4.6b). The closer the cleavage point is to the crack tip,

the higher the hydrostatic stress. The position chosen has a significant effect on the impact of hydrogen on the fracture toughness of the system. The stress fields from the Griffith-Inglis equation for Mode I load are not accurate close to the crack tip, so the position is chosen to be 10 nm along the x_1 axis, as in $\zeta_{\text{cleav}} = 10 + 0i$. Different cleavage positions have been tested to confirm that the overall behaviour of the hydrogen effect is the same.

4.3.1 Reduced Dislocation Energy

A reduced line energy of a dislocation due to hydrogen could lead to two changes considered in this work. The first is a reduction in the elastic interaction between dislocations. The second is a change to the mobility of dislocations. The reduction in the line energy of dislocations is based on nanonindentation data of Fe-3wt$\%$ [54]. The change to the dislocation mobility is based on the work of Katzarov [100].

In nanoindentation, there is a phenomenon where a sudden plastic avalanche called the pop-in can occur. The pop-in event can be linked to nucleation of a dislocation loop. A dislocation loop is stable if the forces on the loop are higher than the attractive forces between the dislocation loop segments. The competition between external and internal forces on the dislocation loop is used as the nucleation criterion. In the criterion, the self-energy of the dislocation determines at what stress a dislocation would be stable. In testing of Fe-3wt$\%$Si [54], the introduction of hydrogen lowers the load necessary to induce the pop-in. The lowered pop-in load can be correlated to a reduction in the line energy of the dislocations γ_{disl} [53].

In the case of nanoindentation, the loop nucleated is in the size of nanometers, whereas, this work has infinite straight dislocations. The core contribution of the self-energy in this chapter is then negligible. The line energy is represented through a simplified version

$$\gamma_{\text{disl}} \simeq \frac{Gb^2}{2\pi}. \tag{4.17}$$

Here the line energy of a dislocation is determined by its shear modulus G and Burgers vector b. The influence of hydrogen comes through changing the line energy of the dislocation. The exact change to the line energy used here is based on nanoindentation data from Barnoush et al. [54]. The energy of dislocation without hydrogen using Eq. 4.17 gives an line energy density of 7.98×10^{-10} J/m, with material parameters listed in section 4.2.1. The line energy change $d\gamma_{\text{disl}} = \Gamma_{\text{H}}\mu_{\text{H}}$ is controlled by the chemical potential of hydrogen μ_{H} at the dislocations positions with a constant excess hydrogen Γ_{H}, given in table 4.1.

The change to line energy in the experimental work of Barnoush [54] is not linear, which is due to the fact that the excess hydrogen at the dislocation can also be dependent on the chemical potential of hydrogen. Though, a constant Γ_{H} is assumed for simplicity, where the best fit is within a μ_{H} between 5 and 20 kJ/mol. There is no change in line energy when $\mu_{\text{H}} < 0$ and any change in the line energy when $\mu_{\text{H}} > 25$ kJ/mol is set to $\mu_{\text{H}} = 25$ kJ/mol.

The numerical implementation of the hydrogen effect on the line energy is done by modifying the Burgers vector of the dislocations. The hydrogen effect on the line energy of dislocations produces in this case an effective Burgers vector b^*. The effective Burgers vector is reduced in length to reduce the line energy of the dislocation, based on Eq. (4.17). The implementation is presented in Fig. (4.7). We would like to stress that we do not believe hydrogen in fact reduces the length of the Burgers vector. The reduction to the Burgers vector in this model is only

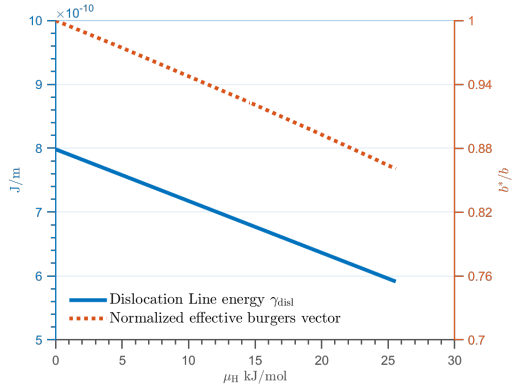

Figure 4.7: The figure illustrates the reduction in line energy of a dislocation with chemical potential of hydrogen μ_{H}, and the numerical implementation of the reduction. The suggested hydrogen effect of a lowered elastic interactions between dislocations is emulated with a reduction to the Burgers vector, as in an effective Burgers vector b^*. This effective Burgers vector is only applied to the elastic interactions between defects described in section 4.2.1. We wish to stress the fact that we do not believe hydrogen reduces the Burgers vector of the dislocations. The implementation is strictly to emulate reduced elastic interaction between the defects in the system.

applied to the elastic interaction discussed in section 4.2.1. Lowering the line energy of dislocations is an attempt to emulate the HELP mechanism. The lowered line energy of dislocations results in smaller stresses between dislocations. It can also affect the mobility of dislocations, as will be discussed in the following section.

Mobility Changes

This subsection discusses the effect of hydrogen on the mobility of dislocations. The hydrogen effect on dislocation mobility is applied to the velocity calculated by the phenomenological equation 4.7. The dislocation velocity is changed based on the local hydrogen concentration $C(\zeta)$ at the position ζ of the dislocation. The change to the dislocation velocity is based on the work of Katzarov [100] using the kinetic Monte-Carlo scheme designed by Cai [102]. The work in Katzarov [100] included the effect of hydrogen by lowering the kink-pair nucleation energy Q_{kp} and the solute drag effect on the kink edge segments.

The effect of the hydrogen on dislocation mobility has been extracted from figure 13[100], using six sampling points per applied resolved stress and fitted using a piecewise linear interpolation. The piecewise linear interpolation of the hydrogen effect on dislocation mobility is shown in Fig. 4.8a. Fig. 4.8a shows the change in the dislocation velocity due to hydrogen as the logarithm of the actual velocity without hydrogen. Two white lines have been drawn in the map, which are connected with the blue and green lines in Fig. 4.8b. Fig. 4.8b shows the velocity for three cases of hydrogen concentration. The two lines for the hydrogen concentration are just examples, and the simulation can sample within the 1 to 20 appm hydrogen range. Below 1appm, the change to dislocation mobility is assumed negligible, above 20 appm is set to the recorded change for 20 appm.

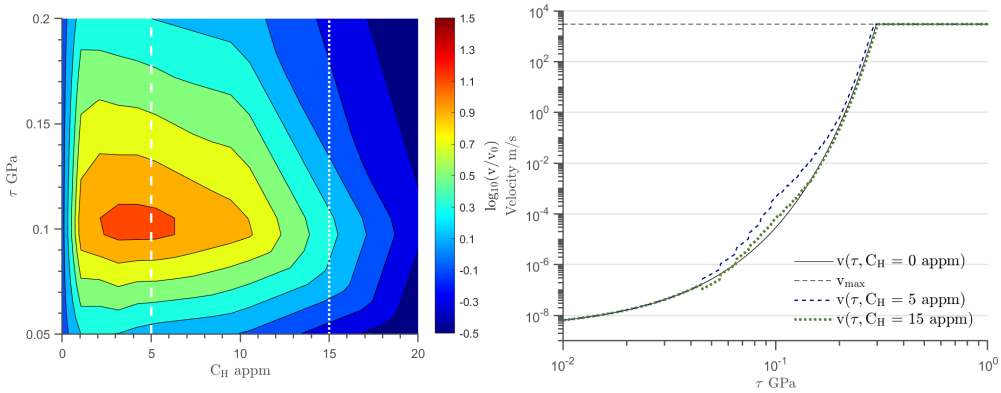

(a) An color map of the hydrogen effect.

(b) The velocity of dislocations.

Figure 4.8: The hydrogen effect on dislocation mobility is shown in these two figures. In a) the map shows the varying changes to the dislocation velocity depending on the resolved glide stress τ on the dislocation, and the surrounding hydrogen concentration C_{H} at the position of the dislocation. The change to the velocity is the logarithm of the ratio of the actual velocity without the hydrogen influence. The two lines drawn in the colour map connects with b). b) shows the actual velocity of the dislocations as a function of the resolved glide stress in three different environments, one without hydrogen, and two with different base concentrations of hydrogen.

4.3.2 Reduced Surface Energy at Crack

The cohesive strength of the bonds at the crack tip is emulated using the Griffith criterion(Eq. 4.10) for a cleavage fracture. The hydrogen effect on the cohesive strength of the bonds at the cleavage position is implemented as a reduction in the threshold for cleavage. The reduction in the cleavage threshold is a function of the chemical potential of hydrogen at the cleavage position. This subsection will link the cleavage threshold to the chemical potential of hydrogen.

The ideal fracture energy for a crack in pure iron is assumed to be dependent on the hydrogen coverage along the cleavage path. A high hydrogen density at the crack surface lowers the surface energy. The cleavage threshold is correlated with the surface energy through Eq. (4.10). A change to the surface energy of a possible cleavage path could, therefore, indicate a lowered cleavage threshold.

The defactant framework is used to estimate the change to the energy of the surface that would be formed in case of a cleavage fracture. Our model is able to estimate the change to the chemical potential of hydrogen; including both the initial effect of gas charging and change due to loading. The surface energy is the controlling parameter in the cleavage criterion, and with that, the impact of hydrogen on the cleavage threshold can be implemented in this study. By starting with

$$\gamma_{\mathrm{s}} = \gamma_{\mathrm{s}}^{0} + \Delta\gamma_{\mathrm{H}}, \tag{4.18}$$

where γ_{s} is the estimated surface energy at the cleavage position. γ_{s}^{0} is the surface energy without hydrogen and $\Delta\gamma_{\mathrm{H}}$ is the change in surface energy due to hydrogen. To find the change in surface energy we must find the change in the chemical potential of hydrogen $\Delta\mu_{\mathrm{H,b}}$ at the cleavage position.

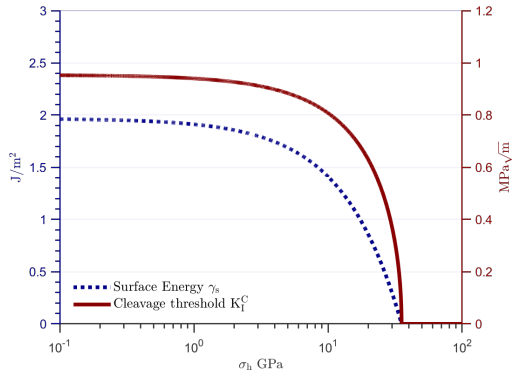

Figure 4.9: The surface energy and the Griffith Criterion as a function of the hydrostatic stress under a hydrogen gas pressure of 10 kPa. The hydrostatic stress increases the local hydrogen concentration, which weakens the interatomic bonds. This is estimated through Eq. 4.20, where the increased hydrogen concentration due to the hydrostatic stress decreases the surface energy.

The first step is to estimate the conditions before loading, where the chemical potential of hydrogen is based on the charging conditions alone. The changes to the surface energy γ_{s}^{*} due to the hydrogen gas charging μ_{g} is $\gamma_{\mathrm{s}}^{*} = \gamma_{\mathrm{s}}^{0} + \Gamma_{\mathrm{H}}^{\mathrm{cleav}}\mu_{\mathrm{g}}/2$. The excess hydrogen at the cleavage position $\Gamma_{\mathrm{H}}^{\mathrm{cleav}}$ is determined with Eq. (3.3). Gas pressures above 1 kPa achieve next to full hydrogen saturation, as in $\Gamma_{\mathrm{H}}^{\mathrm{cleav}} = \Gamma_{\mathrm{H}}^{\mathrm{sat}}$ along an eventual cleavage path. Γ_{sat} and the hydrogen interaction energy W_{H} is given in table 4.1. The gas pressure $p_{\mathrm{H_2}}$ 1 and 10 kPa would results in an initial change to the surface energy without load, where γ_{s}^{*} is 2.04 and 1.97 $\mathrm{J/m^2}$, respectively.

The next step is to include the effect of the load on the chemical potential of hydrogen. The critical parameter for this calculation is the local change to the hydrostatic stress σ_h. Combining Eq. (4.14) and Eq. (4.15) leads $\mu_{\mathrm{H,b}} = \mu_{\mathrm{H,b}}^{0} + RTln(C_{\mathrm{H}}^{0}) + \sigma_h(x)V_{\mathrm{H}}$. The initial change to bulk concentration due to the hydrogen gas charging is already accounted for in γ_{s}^{*}. So the only significant change during the simulation is the change to the hydrostatic stress. The change to chemical potential due to loading $\Delta\mu_{\mathrm{H}}$ is

$$\Delta\mu_{\mathrm{H}} = \sigma_h(\zeta_{\mathrm{cleav}})V_{\mathrm{H}} \tag{4.19}$$

Eq. (4.19) leads to Eq. (4.20), which is the equation used in the simulation. The changes in the surface energy due to loading is calculated through the relationship

$$\gamma_{\mathrm{s}} = \gamma_{\mathrm{s}}^{*} - \Gamma_{\mathrm{H}}\sigma_h(\zeta_{\mathrm{cleav}})V_{\mathrm{H}}. \tag{4.20}$$

γ_{s} is the surface energy used in the calculation of the momentary cleavage threshold in Eq. (4.10). The hydrostatic stress is found using Eq. 4.16. The change in surface energy and the cleavage threshold is shown in Fig. (4.9) as a function of the hydrostatic stress. The potential surface energy at the cleavage position reduces as the loading increases, which also causes a drop in the cleavage threshold.

Case name	p_{H_2} kPa	μ_{H_2} kJ/mol	C_{H}^0 appm	γ_{s}^* kJ/mol	$\Gamma_{\mathrm{H}}^{\mathrm{Cleav}}$ mol/m^2
No Hydrogen	0	Na	Na	Na	Na
HELP 10kPa	1	27.72	0.0019	2.41	0.0
HELP + HEDE 0.1kPa	0.1	21.97	0.0006	2.12	2.61×10^{-5}
HELP + HEDE 1kPa	1	27.72	0.0019	2.04	2.65×10^{-5}
HELP + HEDE 10kPa	10	33.46	0.0061	1.97	2.65×10^{-5}
HELP + HEDE 100kPa	100	39.20	0.0194	1.89	2.65×10^{-5}

Table 4.2: Overview of the hydrogen related parameters for the hydrogen study

4.4 Results

This section starts with introducing the method of analysis and the simulation results without any hydrogen effect in section 4.4.1. The model is then expanded by adding the hydrogen effect through the defactant framework to the dislocation line energy and the surface energy. The reduction in the line energy of dislocations affects both the elastic interaction between the defects and the mobility of the dislocations. The lowered surface energy affects the cleavage threshold. The lowered line energy of dislocations is a variant of HELP, and the lowered surface energy is a version of HEDE.

The parameters for the cases relevant for the hydrogen study are shown in table 4.2. The model emulates hydrogen charging with hydrogen gas charging at a pressure p_{H_2}. The implementation of the charging conditions is described in section 4.3. These charging conditions result in a bulk hydrogen concentration C_{H}^0, starting surface energy γ_{s}^* at the cleavage point and excess amount of hydrogen along the crack surface $\Gamma_{\mathrm{H}}^{\mathrm{Cleav}}$. The "HELP" cases differ from the others ("HELP + HEDE") where only the line energy of dislocations is reduced due to the charging conditions. The HELP + HEDE cases have activated both the reduction to the line energy of dislocations and reduction to the cleavage threshold. By varying the gas pressure, the change in behaviour can be compared to the changes seen in the experiments [45], i.e. faster crack growth rate, sharper crack tips and reduced amount of plasticity.

4.4.1 No Hydrogen

In this section, we will introduce the modelling results with cases without hydrogen. In our analysis there are four points of interest: 1) The fracture toughness, 2) the net shear stress, 3) the dislocation configuration, or in other words, the plastic zone and 4) the crack growth due to dislocation emission and cleavage.

These points of interest will be introduced by varying two parameters that are not investigated in the hydrogen study, lowered temperature and faster loading rate. Changing the temperature or loading rate changes the plastic response, either through decreasing dislocation mobility (decreased temperature) or decreasing the time dislocations have to move (faster loading rate). The temperature in the temperature results are given in the legends, where $\mathrm{T}240$ means that the temperature in the system is at 240 kelvin. The faster loading rate is 10 times the loading rate in the no Hydrogen case ($\Delta K^{\mathrm{a}} = 10$ MPa$\sqrt{\mathrm{m}}\mathrm{s}^{-1}$).

The introduction starts with an explanation of the dynamics from start to finish for the case

without hydrogen with the fixed parameters described in table 4.1. Then the loading rate and temperature cases will follow with the points of interest.

Here we will introduce the reference case for the hydrogen study, the "No Hydrogen" case. The simulation begins with an initial loading where the local stress intensity is equal to the global applied stress intensity, see Fig. (4.10). The first emission of a dislocation from the crack tip occurs at $K_{\mathrm{I}}^{\mathrm{a}} = 0.42$ MPa$\sqrt{\mathrm{m}}$. As the load increases, more dislocations are emitted from the crack tip. The two dislocation sources at their respective side of the x-axis produce their own slip band. The generation of each dislocation must overcome its image stress and the back stress of the previously nucleated dislocations. Without climb, cross-slip, and junction formation, the elastic interaction between dislocations is the only hardening mechanism.

The stress state of the crack tip, represented by $K_{\mathrm{I}}^{\mathrm{L}}$, fluctuates with every dislocation emission, see Fig. (4.10a). The increasing back stress of the dislocation configuration increases the stress state of the crack tip. The rate of increase to the stress state of the crack tip depends on the mobility of dislocations, the slower the mobility, the higher the rate. The simulation increases the applied load $K_{\mathrm{I}}^{\mathrm{a}}$ at a rate $\Delta K_{\mathrm{I}}^{\mathrm{a}}$ until the stress state of the crack tip exceeds the cleavage threshold, red line in Fig. (4.10). When the stress state of the crack tip exceeds the cleavage threshold, a cleavage event is activated, and the simulation ends.

The first point of interest, the fracture toughness, is estimated as the applied stress intensity $K_{\mathrm{I}}^{\mathrm{a}}$ when a cleavage event occurs. In Fig. (4.11), the local stress intensity at the crack tip is plotted against the applied stress intensity. The fracture toughness $K_{\mathrm{I}}^{\mathrm{C}}$ is extracted from the point where the local stress intensity and corresponding cleavage threshold line intersect. The fracture toughness predicted by the model is changed by decreasing the temperature, done in Fig. (4.11a) or increasing the loading rate Fig. (4.11b).

Reducing the temperature (Fig. (4.11a)), reduces the mobility of dislocations. Lower dislocation mobility reduces the emission of dislocations from the crack tip, as the emitted dislocations spend more time close to the crack tip compared to in cases of higher mobility. This reduces the fracture toughness of the system and activates the cleavage event when the stress state of the crack tip exceeds the cleavage threshold.

Similarly, increasing the loading rate (Fig. (4.11b)), reduces the time dislocations have to move. The plastic response from the crack tip is limited by the mobility of the dislocations. Hence, the faster loading rate reduces the fracture toughness of the system, activating a cleavage event at a lower load.

In some cases, as in the case without hydrogen, the cleavage event is not reached; this is due to computational reasons. The numerical calculations are taking too long, with an efficiency at the end of over a year of computations per second simulation time. The computation slows down due to the increasing number of dislocations in the simulation. In the cases where a cleavage event did not occur, an extrapolation was implemented to estimate the fracture toughness. The extrapolation was done using a power-law $a(x)^m$, fitting for the coefficient a and m. The extrapolation is only intended to demonstrate the change in fracture toughness when the hydrogen mechanisms are applied. The extrapolated cleavage event for the "No Hydrogen" case, i.e. $T = 300$ and $\Delta K_{\mathrm{I}}^{\mathrm{a}} = 1$ MPa$\sqrt{\mathrm{m}}$/s, is calculated to be 10.44 MPa$\sqrt{\mathrm{m}}$, with the coefficients $a = 0.4965$ and $m = 0.3235$. This would correspond to a global stress of $\sigma = 223$ MPa using the relations described in section 4.2.2.

The second point of interest is the net shear stress τ_{f}, which is the resolved glide stress averaged over the dislocations. During loading, each dislocation has a resolved glide stress

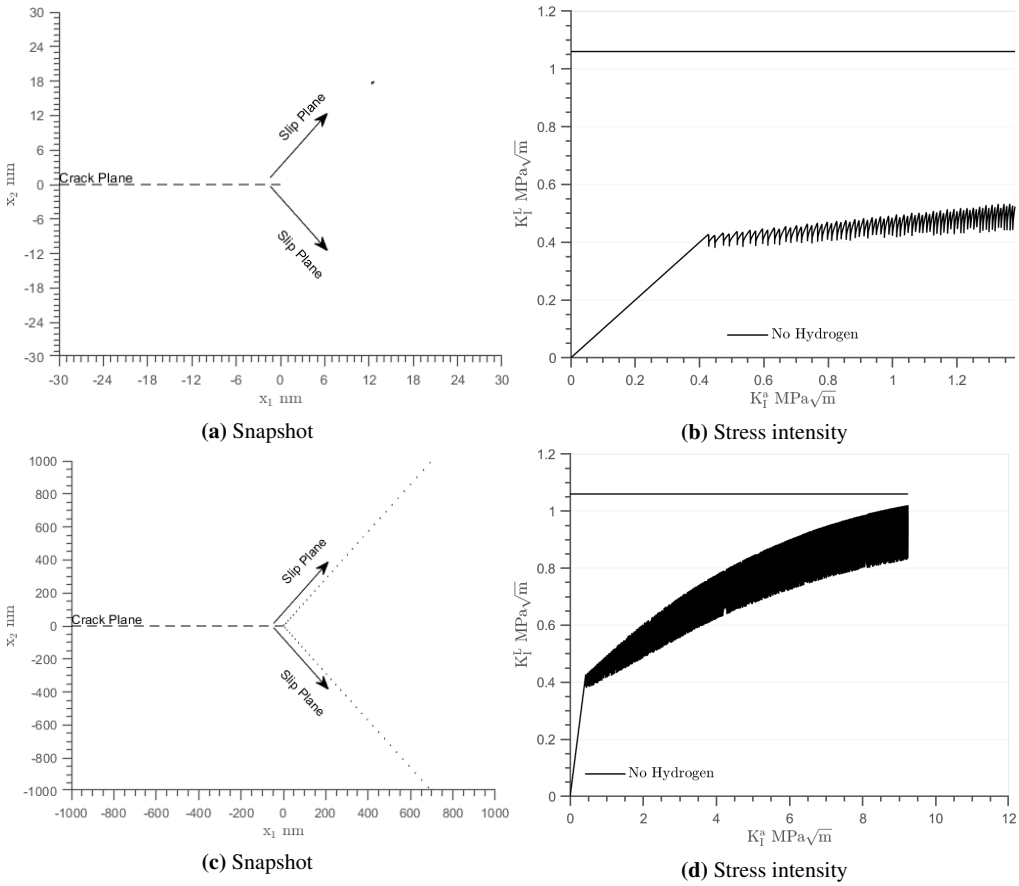

(a) Snapshot

(b) Stress intensity

(c) Snapshot

(d) Stress intensity

Figure 4.10: Snapshots of the model at two different applied stress intensities. a) and b) $K_{\mathrm{I}}^{\mathrm{a}} \simeq 1.38\mathrm{MPa}\sqrt{\mathrm{m}}$ and c) as well as d) $K_{\mathrm{I}}^{\mathrm{a}} \simeq 9.24\mathrm{MPa}\sqrt{\mathrm{m}}$. The dots spreading out at an angle from the crack plane are dislocations. The dislocation configuration is formed due to the point sources that are put into the simulation, one source per slip plane. a) & c) are drawings of a subset of the infinite simulation volume. There are more dislocations in the simulations than shown in the snapshots. b) & d) are the loading history of the simulation up til the $K_{\mathrm{I}}^{\mathrm{a}}$. The loading history shows the development of the stress state of the crack tip due to the external loading. The local stress intensity $K_{\mathrm{I}}^{\mathrm{L}}$ depends on the applied stress intensity and the shielding effect due to the dislocation configuration. The red line is the cleavage threshold. A cleavage event occurs when the local stress intensity (black line) intersects with the cleavage threshold (red line).

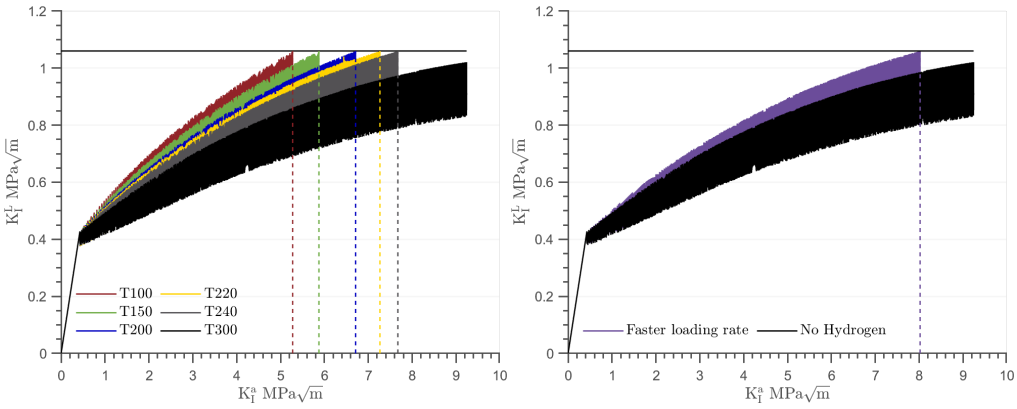

(a) Temperature **(b)** Loading rate

Figure 4.11: The variation in the stress state of the crack tip $K_{\mathrm{I}}^{\mathrm{L}}$ dependent on the applied stress intensity $K_{\mathrm{I}}^{\mathrm{a}}$. a) and b) are examples of reducing the temperature or increasing the loading rate, respectively.

that is close to the net shear stress, except for the dislocations close to the crack tip. The net shear increases with increasing loading. The increase depends on the loading conditions and the dislocation mobility. Figure 4.12 shows the history of the net shear stress with increasing load. The net shear stress is an indication of the mobility of dislocations in the system; a higher net shear stress means it is harder for dislocations to move.

By lowering the temperature (lower dislocation mobility) or by increasing the loading rate, the net shear stress increases. The harder it is to move the dislocation, the faster the build-up of stresses at the crack tip. A fast build-up of stresses at the crack tip activates the cleavage event at a lower applied load. The mobility and loading parameters given in table 4.1 (”No Hydrogen” case) result in a net shear stress off $\tau_{\mathrm{f}} \approx 160$ MPa at the end.

The change to the residual plastic zones from experimental work will be compared to the dislocation configuration generated by the simulation. The intention is to use the dislocation configuration as an indication of how the plastic zone has developed. A higher net shear stress corresponds to lower dislocation mobility and lower fracture toughness. The lower fracture toughness is a result of the reduced amount of dislocations generated at the crack tip. The reduced amount of dislocations emitted during loading can be seen in Fig. (4.13), where the temperature and loading rate are decreased. The dislocation configuration in Fig. (4.13) shows a snapshot of the distribution of the dislocations away from the crack. The snapshot is taken at a specific global applied stress intensity, in a) $K_{\mathrm{a}} = 5.0\ \mathrm{MPa}\sqrt{\mathrm{m}}$ and in b) $K_{\mathrm{a}} = 8.0\ \mathrm{MPa}\sqrt{\mathrm{m}}$.

Reducing the temperature or increasing the loading rate gives a lower fracture toughness, which is accompanied by a reduced amount of plasticity. Though remember, there are no surfaces or defects. Any comparison with experiments should thus take into consideration what would occur with the plastic zone when defects are introduced.

The crack growth rate and crack growth ratio from the case without hydrogen will serve as the baseline to which the consequences of the hydrogen mechanisms will be compared. The crack growth from the simulation is estimated from dislocation emission and cleavage events. In those cases where a cleavage event is activated, there is crack growth (Δa_c) without contributing to the crack opening. The event can be seen in Fig. (4.14) as a sudden growth without increasing

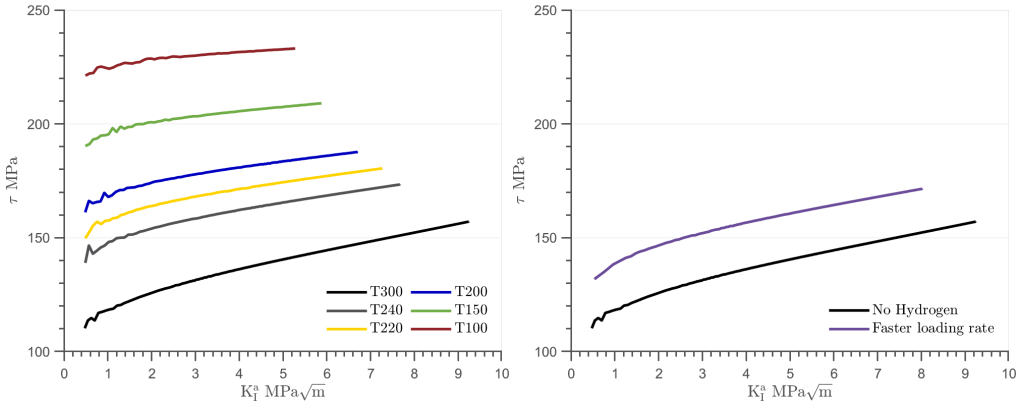

(a) Temperature **(b)** Loading rate

Figure 4.12: The development of the net shear stress of the dislocation configurations is plotted vs the loading. The net shear stress is dependent on the mobility of dislocations. This is shown by varying the temperature or increasing the loading rate. A lower temperature, i.e. lower dislocation mobility, increases the net shear stress of the dislocation configuration. A higher loading rate, which reduces the time dislocations have to move, also increases the net shear stress of the dislocation configuration.

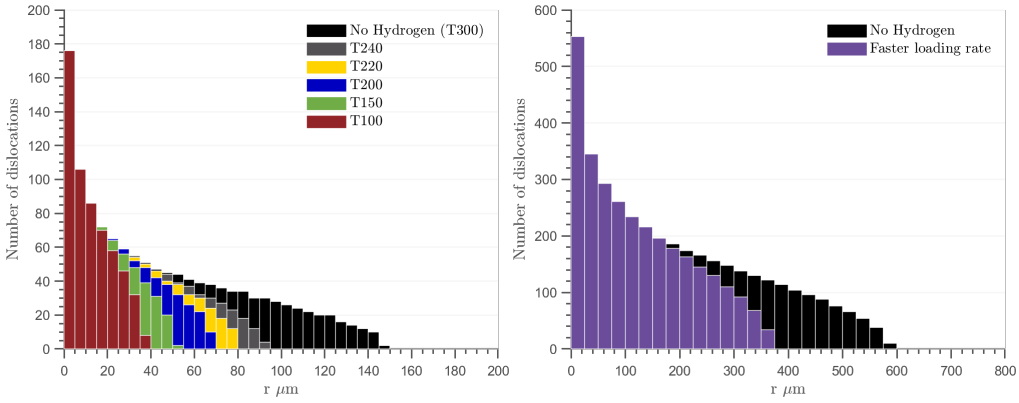

(a) Temperature **(b)** Loading rate

Figure 4.13: The change to the dislocation configuration is presented here with changing the temperature or loading rate. Lowering the temperature in the system, which lowers the dislocation mobility, reduces the amount of dislocation emission from the crack tip. The same occurs with increasing the loading rate. The dislocation configurations are snapshots at the same applied load, $K_a = 5.0$ MPa$\sqrt{m}$ and in b) $K_a = 8.0$ MPa$\sqrt{m}$.

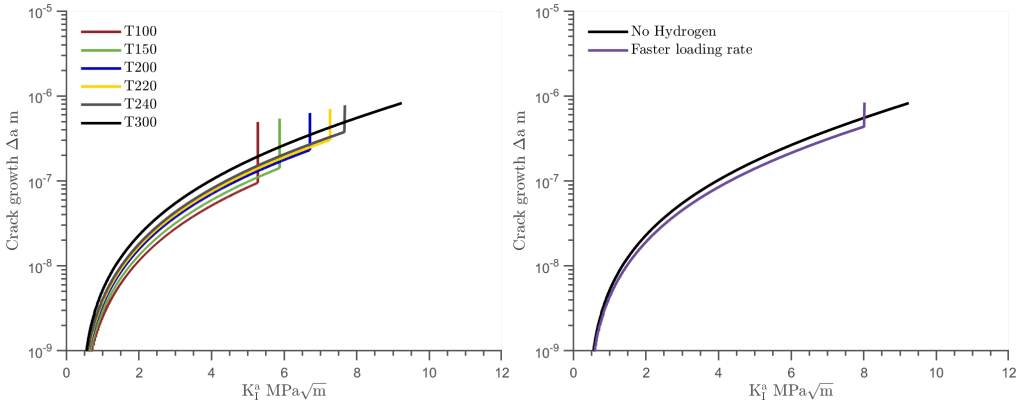

(a) Temperature **(b)** Loading rate

Figure 4.14: The total crack growth as a function of the loading history. The total crack growth is a function of both dislocation emission and cleavage fracture. The total crack growth here grows steadily through dislocation emission. If a cleavage event is recorded, the total crack growth has a sudden uptick. Reducing the temperature or increasing the loading rate decreases the crack growth rate through dislocation emission. However, with activation of cleavage events, the crack growth rate is enhanced significantly.

the load. The total crack growth is a sum of the dislocation emissions (Δa_d) and the cleavage jump (Δa_c). The crack opening is only dependent on the dislocation emission. A higher crack growth ratio compared to the case without hydrogen would indicate a sharpening of the crack.

At the time of writing, we have no solution to estimate how far the crack cleaves before it comes to a rest. Therefore, at this moment, a cleavage jump of $\Delta a_c = 400$ nm is assumed for all cleavage events. The jump distance is not validated, any comparisons except within the model must be done with care.

The total crack growth is presented in Fig. (4.14), where the crack growth is plotted against the applied fracture toughness. Here again, temperature is reduced in Fig. (4.14a) and the loading rate is increased in Fig. (4.14b).

The initial crack growth decreases with reduced dislocation mobility, i.e. reduced temperature or increased loading rate. The reduction to the crack growth rate occurs as the growth is due to dislocation emission. The higher the dislocation mobility, the more dislocations can be emitted at the crack tip. This is an important point; increased dislocation emission will increase the crack growth rate. However, the increased crack growth rate through dislocation emission would not cause a sharpening of the crack.

The lowered plastic response due to either reducing the temperature or increasing the loading rate results in a sharper crack tip. The cases activate a cleavage event, which gives crack growth without any crack opening. The additional crack growth through a cleavage fracture results in a higher crack growth ratio and sharper crack.

Case name	τ_{f} MPa	$K_{\mathrm{I}}^{\mathrm{C}}$ MPa$\sqrt{\mathrm{m}}$	N_{D}	Δa_d nm	$\Delta\delta_{\mathrm{d}}$ nm	Δa_{c} nm	a_{n}
No Hydrogen	157	10.44[1]	5727	824	1164	0	1.42
HELP 10kPa	155	11.22[1]	5463	786	1110	0	1.42
HELP + HEDE 0.1kPa	152	7.273	3218	463	654	400	2.64
HELP + HEDE 1kPa	152	6.841	2806	404	570	400	2.82
HELP + HEDE 10kPa	152	6.463	2482	357	504	400	3.00
HELP + HEDE 100kPa	152	6.095	2192	316	445	400	3.21

[1] Extrapolated fracture toughness

Table 4.3: Results from the cases within the hydrogen study. The fracture toughness $K_{\mathrm{I}}^{\mathrm{C}}$, net shear stress τ_{f}, amount of dislocations N_{D} and crack growth related variables.

4.4.2 Reduced Dislocation Energy

The case "HELP 10kPa" is presented in Fig. (4.15) together with the case without hydrogen, which is added as a reference. The hydrogen effect of lowered dislocation line energy has been applied to both the elastic interaction between dislocations and the mobility changes from section 4.3.1. The hydrogen gas pressure is at 10 kPa, with a bulk hydrogen concentration $C_0 = 0.0061$ appm. The extrapolated fracture toughness and other results the "HELP 10kPa" case, and others, are given in table (4.3).

The emission of the first dislocation occurs at a lower applied load compared to the case without hydrogen, see Fig. (4.15a). The reduced energy of the dislocation activates the emission of the first dislocation at a lower stress state of the crack tip. Increasing the charging conditions, i.e. a higher chemical potential of hydrogen lowers the necessary stress state at the crack tip for the emission of a dislocation. At the event of the first dislocation emission, due to the local strain at the crack tip, the hydrogen concentration at the source position would be approximate $C_{\mathrm{H}}(d) = 0.0130$ appm. The "HELP" case emits the first dislocation at a lower applied stress intensity than compared to the "No Hydrogen" case. With reduced line energy, the emission of the first dislocation occurs at a lower load. The first dislocation emission occurs at $K_{\mathrm{I}}^{\mathrm{a,nuc}} = 0.35\mathrm{MPa}\sqrt{\mathrm{m}}$, without hydrogen the first emission occurs at $K_{\mathrm{I}}^{\mathrm{a,nuc}} = 0.42\mathrm{MPa}\sqrt{\mathrm{m}}$.

The predicted fracture toughness of the "HELP" case, Fig. (4.15a), is extrapolated to be $11.22\ \mathrm{MPa}\sqrt{\mathrm{m}}$, with the coefficients $a = 0.4543$ and $m = 0.3505$. This is equivalent to a global stress of $\sigma = 240$ MPa. The lowered elastic energy of dislocations enhances the fracture toughness of the system by $7.5\ \%$. Increased fracture toughness has been shown to be connected to a lowered net shear, i.e. increased dislocation mobility. However, the net shear stress is the same as for the case of "No Hydrogen", at the end of the simulation $\tau_{\mathrm{f}} \approx 160$ MPa.

The dislocation configuration in Fig. (4.15b) is a snapshot of the dislocation configuration in both cases at a loading off $K_{\mathrm{a}} = 8.0\ \mathrm{MPa}\sqrt{\mathrm{m}}$. The lowered line energy of the dislocations results in an increased number of dislocations. The reduced elastic interaction between the defects in the system increases the dislocation density along the plastic zone.

The crack growth due to dislocations is shown in Fig. (4.15c). Both simulations are unfinished due to increased computational demand with increasing number of dislocations. However, the cases can still be compared to each other. The crack growth in the "HELP 10kPa" is higher than the "No Hydrogen" case. In this case, the increased dislocation emission increases the

crack growth rate. Though, the crack growth rate predicted here is not significant and the crack would not be sharper. Both cases at the have a crack growth ratio off $a_{\mathrm{n}} = 1.42$, and the crack opening angle is $\alpha = 2\,\mathrm{arccot}\, a_{\mathrm{n}} = 70.3$.

4.4.3 Reduced Surface Energy at Crack

The results from the cases where both hydrogen effects are implemented are presented in Fig. (4.16), including the case without hydrogen as a reference. In these cases, the surface energy and the line energy of dislocation are reduced due to the initial charging and loading conditions. The difference between the hydrogen cases is the gas pressure, given in table 4.2. The resulting bulk hydrogen concentrations are presented in table 4.2. Varying the gas pressure is done to see if the model can capture the same effect as found in experimental testing[45, 80]. The higher the hydrogen gas pressure, the higher the base chemical potential of hydrogen in the simulated cases. The increased chemical potential of hydrogen enhances the magnitude of change due to hydrogen.

With the implementation of the hydrogen effect on the cleavage criterion, the cleavage event is activated at a lower load than compared to without the hydrogen effect. The reduction in the cleavage threshold due to loading is shown in Fig. (4.16a), where the cleavage threshold lines decrease with increasing $K_{\mathrm{I}}^{\mathrm{L}}$. As the strain at the crack builds during loading, the chemical potential of hydrogen close to the crack tip is increased. The cleavage event is activate when the stress state of the crack tip ($K_{\mathrm{I}}^{\mathrm{L}}$) exceeds the cleavage threshold. The increasing chemical potential of hydrogen results in a gradual decrease in the cleavage threshold, activating a cleavage event at a lower load. The resulting fracture toughness recorded for the cases are given in table 4.3. Since the simulation reached a cleavage point there is no need for a extrapolation.

As a reminder, the activation of a cleavage fracture has an impact on the crack growth ratio; the crack is now sharper. There is an initial crack growth due to the dislocation emission, which contributes to the crack opening; the cleavage jump does not. The estimation of sharpness of the crack tip is based on the crack growth ratio explained in section 4.2.1. A cleavage event is assumed to results in a cleavage jump of $\Delta a_{\mathrm{c}} = 400\ \mathrm{nm}$, with a contribution to the crack opening as $\Delta\delta_{\mathrm{c}} = 0$.

The crack growth before the cleavage event for "HELP + HEDE 10 kPa" is $\Delta a_d = 357$ nm, with a crack opening of $\Delta\delta_{\mathrm{d}} = 504$ nm. Using Eq. (4.1) both the crack growth due to dislocation emission and cleavage is included. The crack growth ratio for "HELP + HEDE 10 kPa" is $a_{\mathrm{n}} = 3.00$, and the crack opening angle would be $\alpha \simeq 2\,\mathrm{arccot}\, a_{\mathrm{n}} = 36.9°$.

The major difference between the charging conditions is that with a lower gas charging the cleavage event occurs at a higher load. This means more dislocation emission and corresponding crack growth and opening before the cleavage event. At lower gas pressures, the sharpening due to hydrogen is reduced. A higher hydrogen gas charging in this model results in a sharper crack.

With the activation of a cleavage event at a lower load, the corresponding dislocation configuration is less developed. In Fig. (4.16b), the dislocation configurations are plotted at the last recorded snapshots. In the case of the "HELP + HEDE" cases, the last recorded snapshot is at the cleavage event, whilst for the "No Hydrogen" case it is at $K_{\mathrm{I}}^{\mathrm{a}} = 9.24$ MPa $\sqrt{\mathrm{m}}$. The activation of a cleavage event at a lower load gives a smaller dislocation configuration. The plastic zone reduces with a reduction to the cleavage threshold. A higher gas charging results

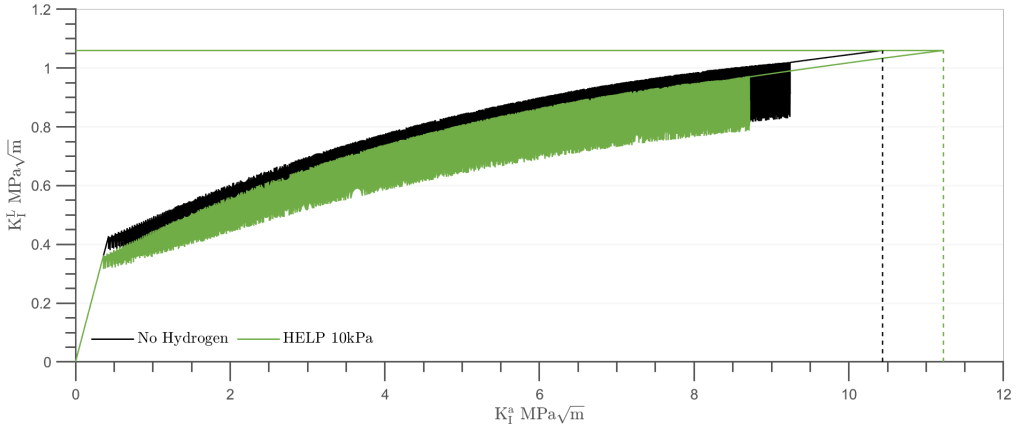

(a) Local vs Global stress intensity

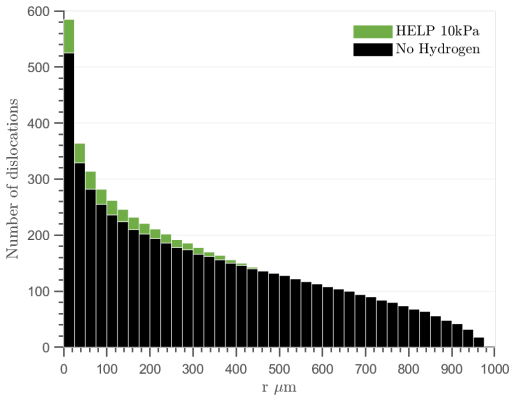

(b) Dislocation configuration

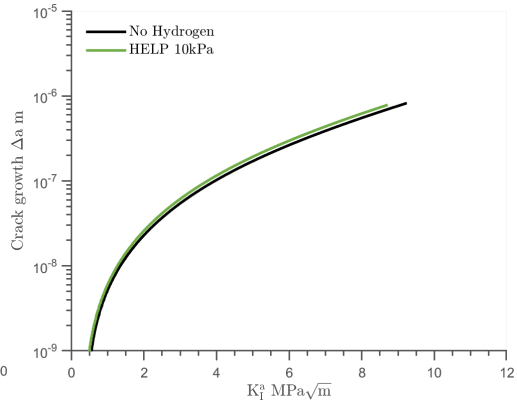

(c) Crack Growth

Figure 4.15: There are two cases presented in this figure. The green is the "HELP" case where the line energy of the dislocations is reduced due to hydrogen. The chemical potential of hydrogen affects both the elastic interactions between dislocations and their mobility. The black case is the case without hydrogen added for reference. a) Local stress intensity, $K_{\mathrm{I}}^{\mathrm{L}}$ vs. applied stress intensity $K_{\mathrm{I}}^{\mathrm{a}}$. The local stress intensity and corresponding cleavage criterion lines are drawn with the same colour. There is no change to the cleavage criterion in these cases, so both cleavage criterion lines overlap. b) A snapshot of the dislocation configurations for both cases at the same loading, $K_{\mathrm{a}} = 8.0$ MPa$\sqrt{\mathrm{m}}$. c) The crack growth due to alternating dislocation emission. Neither case in this figure activated a cleavage event.

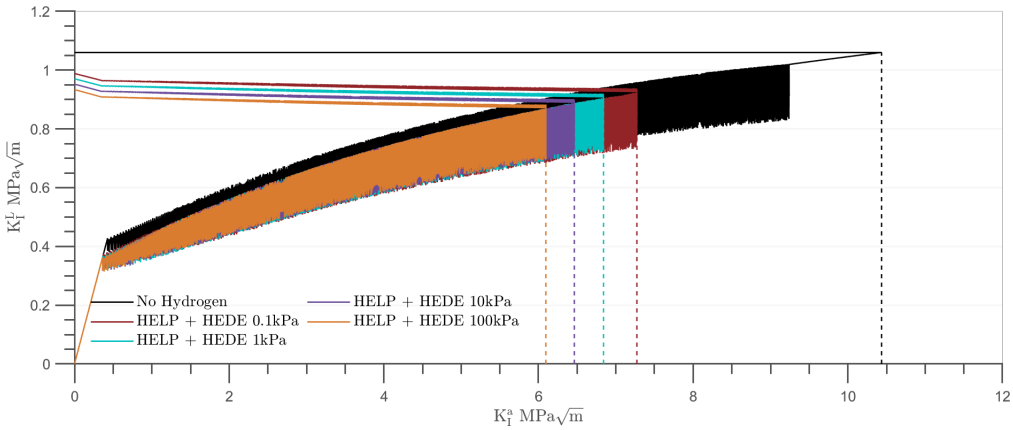

(a) Local vs Global stress intensity

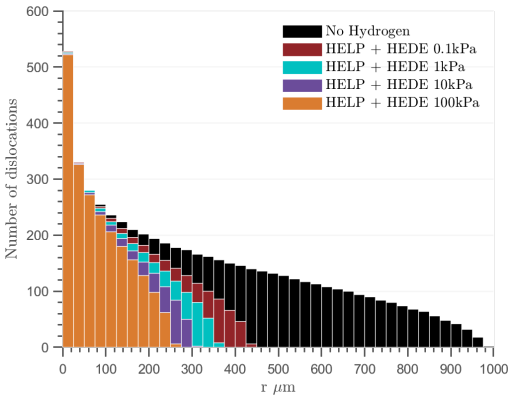

(b) Dislocation configuration

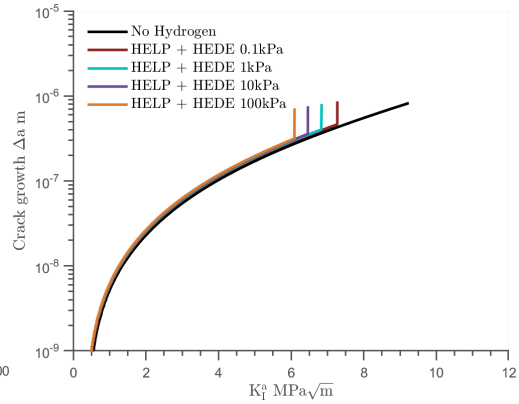

(c) Crack Growth

Figure 4.16: The results in this figure are from cases where where the effect of lowered energy is applied to both dislocations and the crack surface. As in Fig. (4.15), the case without hydrogen is included in black as a reference. The difference between these cases is the charging conditions, as in different applied hydrogen gas pressures. a) Local stress intensity, $K_{\mathrm{I}}^{\mathrm{L}}$ vs. applied stress intensity $K_{\mathrm{I}}^{\mathrm{a}}$. The local stress intensity and corresponding cleavage criterion lines are drawn with the same colour. b) Snapshot of the dislocation configuration at different applied stress intensities. For the HELP + HEDE cases the snapshot is at the cleavage event, for the "No Hydrogen" case, the snapshot is at $K_{\mathrm{a}} = 9.24\,\mathrm{MPa}\sqrt{\mathrm{m}}$. c) The crack growth due to alternating dislocation emission and cleavage growth when the cleavage event is activated. The effect of the cleavage event on the total crack growth is the vertical growth without increase to load.

in less plasticity.

4.5 Discussion

The idea behind the work in this chapter is to use a 2D crack model that can simulate the critical aspects of the hydrogen effect on crack growth in iron. The two hydrogen mechanisms, HELP and HEDE, are implemented into the model with the intention to see which can replicate the experimental findings of an enhanced crack growth rate, smaller residual plastic zones and sharper crack tips. The effect of hydrogen is implemented through the defactant framework by lowering the energy of dislocations and the crack surface. Lowering the elastic interaction between defects emulates the HELP mechanism. The reduction to the cleavage threshold emulates the HEDE mechanism.

The discussion will start with an analysis on the results from the model without hydrogen. The resulting fracture toughness and dislocation configuration from the 2D crack model is shown to not be directly comparable with experimental results. The value of these results is the comparison between cases, identifying which can cause cleavage at a lower load. The discussion then continues by comparing the results when hydrogen is implemented. The reduced elastic interaction between the dislocations enhances plasticity. The reduced elastic interactions alone do not reproduce the experimental results. The hydrogen effect on dislocation mobility could both enhance or decrease the plastic response. However, the solubility of hydrogen in iron is too small to allow any mobility effect to have a significant impact on the plastic work. The reduction of surface energy reproduces the experimental results. In this current study hydrogen effectively reduces the cleavage criterion with the increasing chemical potential of hydrogen ahead of the crack tip. Activation of a cleavage event at a lower load leads to a loss in fracture toughness, smaller plastic zone and a sharper crack tip.

4.5.1 The Case without Hydrogen

Within this section, we will discuss the validity of the standard case, "No Hydrogen". The intention is to indicate where the model succeeds and fails. This discussion will also include the results of varying the temperature and the loading rate.

The accuracy of the predicted fracture toughness by the model for the standard case, "No Hydrogen", is unclear. The simulation of the "No Hydrogen" case have not ended due to computational reasons mentioned above. An extrapolation is used to estimate at what load the cleavage event would occur. The extrapolation is based on a power law. The accuracy of the extrapolation in cases where the cleavage event occurs at applied stress intensities below 8 MPa$\sqrt{\mathrm{m}}$ is within an error range of ± 0.2 MPa$\sqrt{\mathrm{m}}$. The accuracy of the extrapolation above the 8 MPa$\sqrt{\mathrm{m}}$ applied stress intensity is not clear. The extrapolation may over- or under-estimates the fracture toughness.

The experimental results [45, 80] do not offer a fracture toughness which the modelling results can be compared too. There is a previous study on the fracture toughness of Fe-3wt$\%$Si [97]. Though, the study's loading conditions and the geometry of the specimens are not the same as in our model.

An ad-hoc comparison for the fracture toughness between the model and experimental data from Vehoff and Rothe [45] can be done. The net stress $\sigma_{\mathrm{net}} \approx 250$ MPa given in figure 3 of

[45] is assumed to be the maximum opening stress that is applied to the specimen in their study. The authors recorded a crack growth ratio of $a_{\mathrm{n}} = 1.42$ at that load, which would indicate that a cleavage event was not activated. The opening stress σ_{net}, using the relations described in section 4.2.2, would indicate an maximum applied stress intensity of $K_{\mathrm{I}}^{\mathrm{a}} \approx 11.7\ \mathrm{MPa}\sqrt{\mathrm{m}}$. This applied stress intensity from Vehoff and Rothe is higher than the predicted fracture toughness from our model, $K_{\mathrm{I}}^{\mathrm{a}} \approx 10.4$. From this comparison, we conclude that our model would seem to underestimate the fracture toughness. However, we do not know the loading rate from Vehoff and Rothe. That max load could be reached with this model without activating a cleavage event by using a slower loading rate.

There is an additional concern with the accuracy of the predicted fracture toughness in relation to the temperature. The fracture toughness increases linearly with increasing temperature. While we do not have exact experimental conditions to compare with, the BDT found in the experimental data [97], and previous 2D DDD modelling of the BDT in Fe [23], would suggest a more sudden behaviour with increasing temperature with a peak at the BDT. This means there is no clear transition between brittle and ductile crack growth behaviour. This could be related to the assumption of quasi-static dynamics.

The model may be missing some inertial effects in the dislocation dynamics close to the crack tip. In this context, it is important to point out that great care must be taken with the numerical integration. By relaxing our thresholds for numerical integration errors (increasing the time step), a more sudden behaviour is predicted by the model. The error is in the dynamics close to the crack tip. The stresses are in the GPa range close to the crack tip, and the dislocation velocities are close to the sonic barrier ($v_{\max}$). The integration error may counteract an oversimplification of the assumption of quasi-static dynamics and create an artifact that looks like a BDT peak.

The choice in the dislocation mobility parameters were taken with emphasis on later investigating the hydrogen effect as accurately as possible. The mobility parameters could have been fitted to better reproduce the BDT, but this would have clouded the hydrogen effect. Therefore the dislocation velocity and the effects of hydrogen from Kazarov [100] were used.

The final snapshots of the dislocation configurations should also be interpreted with care. The simulated dislocation configuration is a snapshot at the time of loading. In contrast, in experiments, the plastic zone is often identified after loading in post-analysis. The difference in dislocation configuration between max loading and post-analysis could be considerable. If a cleavage occurs, or the specimen is unloaded, the stress field maintaining the current configuration will go away. When the stress field is removed, the dislocation configuration will find a new equilibrium. The model can include the unloading, where the final dislocation configuration would have been more comparable with the experimental data. However, the unloading has not been included as the calculations of the loading is still ongoing. Nonetheless, the snapshots of the dislocation configuration in this study have been included in the results to offer a possible link with the reduced plasticity found in post-analysis of crack growth in Fe-3wt$\%$Si [80].

What the model can capture is the crack growth rate due to dislocation emission, and illustrate the sharpening of a crack with cleavage fractures. Due to the mentioned uncertainties with the accuracy of the model; conclusions could not be drawn on the exact crack growth rate due to load and on the transition to sharpness. What the model can provide is which hydrogen effect enhanced crack growth rate and causes a sharpening of the crack tip.

The model associates the crack growth ratio with the activated slip system and is able to

predict a similar ratio as given in experiments [45], ignoring discrepancy address in the ad-hoc comparison given above. As long as the load never reaches the extrapolated fracture toughness of $10.44\ \mathrm{MPa}\sqrt{\mathrm{m}}$, the crack growth would be steady, and the crack growth ration is $a_{\mathrm{n}} = 1.42$. If we ever were to exceed the fracture toughness and activate a cleavage event, the result would be catastrophic as the crack would cleave into the tensile field of the dislocation configuration. The tensile field of the dislocations would only enhance the stresses at the crack tip, and the crack growth would be unstable. This is not necessarily the case when the cleavage event is activated at a lower load due to hydrogen [99].

The quantitative accuracy of the model is unclear, and this investigation will instead focus on what the implemented hydrogen mechanisms do to the crack growth rate and the crack growth ratio relative to the modelling results without hydrogen. Specific conclusions on exact critical charging conditions for the detrimental effect of hydrogen are, therefore, not given.

4.5.2 Reduced Dislocation Energy

The HELP mechanism is emulated by reducing the line energy of dislocations. The investigation on this hydrogen mechanism is done using a single case, (”HELP 10kPa”). The reduction to the line energy has two effects in this current implementation. The hydrogen effect on the line energy is explained in more detail in section 4.2.1. The reduction in the line energy of dislocations affects both the elastic interactions and the mobility of the dislocations. The reduction to the elastic interaction and changes to the dislocation mobility depends on the chemical potential of hydrogen at the dislocation. The magnitude of the change is connected to the chemical potential of hydrogen.

Reducing the elastic interaction between the defects enhances dislocation generation at the crack tip. The first emission of a dislocation occurs at a lower applied stress intensity compared to the ”No Hydrogen” case. Loading of the crack with the reduced elastic interactions also generates more dislocations than the ”No Hydrogen” case. Increasing the hydrogen gas pressure would increase the chemical potential of hydrogen, and reduce the elastic interactions even further.

The lowered elastic interaction also reduces the average distance between dislocations. The ”HELP” case has a higher dislocation density along the entire dislocation configuration. The reduced elastic interactions facilitate a smoother dislocation configuration, leading to a more effective shielding of the stresses at the crack tip. The more effective shielding leads to increased fracture toughness.

The hydrogen effect on the elastic interactions adds another complication in comparing the dislocation configuration between simulation snapshot and experimental post-analysis. Hydrogen can diffuse out after loading, and the elastic interaction between dislocations could regain their former strength. If the chemical potential of hydrogen changes between loading and the post-analysis, a new equilibrium will have been achieved.

The hydrogen effect on the mobility of the dislocations are negligible under the current charging conditions. The net shear stress on the dislocation configuration in the ”HELP” case is equal to the ”No Hydrogen” case; i.e. the mobility has not been impacted significantly. The chosen hydrogen gas pressure results in hydrogen base concentrations less than one appm. The insignificant effect seen on mobility is a result of the implementations, as it assumes no effect below one appm.

Applying hydrogen charging conditions so that the base hydrogen concentrations are at one appm or above would mostly enhance the dislocation mobility. Enhanced dislocation mobility would not cause a cleavage at a lower load. Lower dislocation mobility, on the other hand, could. The hardening due to hydrogen drag requires high hydrogen concentrations, which are at its highest just ahead of the crack tip. Pinning dislocations close to the crack tip due to the hydrogen drag could cause a severe reduction in the fracture toughness.

Lowered dislocation mobility due to hydrogen means an increase in the net shear stress, and the increasing stress state of the crack tip will accelerate. The more local strain at the crack tip results in higher hydrostatic stress, which, in turn, leads to higher hydrogen concentration and dislocation pinning. The effect would be self-amplifying and would cause a cleavage at a lower load. However, with the current phenomenological equation, a detrimental effect on the fracture toughness due hydrogen drag is difficult to achieve. Testing at artificially high hydrogen concentrations has shown that the drag effect is still negligible as the high stresses close to the crack tip predicts dislocation velocities close to the sound of speed.

If the mobility change needs a higher gas pressure to be effective, it is not the critical hydrogen mechanism at these hydrogen gas pressures. The gas pressures in this study are chosen as experiments have shown that hydrogen has an detrimental impact at these pressures [45].

There is one change in the dislocation mobility that has not been included. A reduced line energy could indicate a change to the activation volume. The lower elastic interaction between the kink edges means that kink-pairs with a smaller width would be stable. Whether or not this leads to an increase, reduction, or no change in the dislocation mobility is difficult to predict a priori. If this change leads to increased friction stress, the dislocation velocity would be reduced. If the change is negligible or enhances dislocation mobility, the simulation results would not replicate the experimental findings.

The enhanced dislocation emission from the crack tip increases the crack growth rate. Though, not by one order of magnitude as was found in the experimental work of Wan et al. [80]. Also, the crack growth is still related to dislocation emission, and so the crack growth ratio is not changed. The reduced line energy of dislocations does not cause a sharpening of the crack tip.

The reduced line energy reduces elastic interaction among defects and changes the dislocation mobility. The magnitude of the effect is controlled through the chemical potential. The reduced elastic interaction enhances the plastic response. Dislocation emission from the crack tip is enhanced, and the dislocation density is higher along the slip band. Due to the enhanced plasticity, the crack tip can more easily accommodate the load. The reduce line energy of dislocations does not lower the fracture toughness, enhanced crack growth to a considerable degree or sharpen the crack tips. The changes in the dislocation mobility are negligible due to the low hydrogen solubility. The effect of hydrogen on the mobility of dislocations are deemed not critical, though with one caveat. The hydrogen effect on elastic interaction between kink edges is not included. The consequences for the dislocation mobility, with a reduced elastic interaction between the kink edges, are unknown.

4.5.3 Reduced Surface Energy at Crack

This final section will include the fully applied hydrogen mechanisms as detailed in section 4.3. Hydrogen reduces the line energy of dislocations and the energy of the surface that would be

formed in the case of a cleavage. The reduced surface energy lowers the cleavage threshold, and is meant to represent the HEDE mechanism. The effect of changing the hydrogen gas pressure is also investigated. A higher gas pressure results in a sharper crack tip in the experiments [45]. That sharpening in this model can be linked with the lowered cleavage threshold.

The fracture toughness of the system is reduced with the applied hydrogen effect. The reduction in the fracture toughness is mainly due to the reduction in the cleavage threshold. The reduction in the cleavage threshold changes with the chemical potential of hydrogen at the cleavage point. The increased strain at the crack tip leads to a higher chemical potential of hydrogen, which in turn reduces the energy of the surface that would be formed at a cleavage event. The reduced surface energy lowers the cleavage threshold. The reduced cleavage threshold activates a cleavage fracture at a lower load.

The enhanced fracture toughness due to the enhanced plasticity (reduced line energy) is counterbalanced by the lowered cleavage threshold. The added hydrogen concentration due to loading is at the highest right ahead of the crack tip due to the high hydrostatic stresses. The reduction to the cleavage threshold is the most critical hydrogen effect with the current loading and charging conditions.

The activation of a cleavage event at a lower load leads to both less plasticity and a smaller plastic zone size. Fatigue crack growth test [80] reported a reduced residual plastic zone. The experimental reduced residual plastic zone may be due to activation of a cleavage event at a lower load.

The model links the sharpening of the cracks to activation of cleavage events. Dislocation emission contributes to crack opening, cleavage growth does not. A cleavage event at a lower load means less growth through dislocation emission. The following crack growth due to the cleavage jump has a larger impact on the crack growth ratio. A higher ratio of crack growth through cleavage would mean a sharper crack, illustrated in fig (4.17).

The activation of a cleavage event is different compared to the case without hydrogen. In the case without hydrogen, the cleavage event is catastrophic, and crack growth is unstable. This is not the case when hydrogen lowers the cleavage criterion locally. In the case of hydrogen, the cleavage event is activated due to the elevated hydrogen concentration at the crack tip. At the time, when the crack cleaves through the material, it will travel into areas where hydrogen concentration is less affected by the stress field of the crack. The hydrogen concentration ahead of the now newly formed crack tip is much lower than at the crack tip's previous location. The lowered hydrogen concentration would indicate higher energy necessary for cleavage fracture. The cleavage threshold would increase as the crack grows. At a certain point, the cleavage threshold would be higher than the criterion for dislocation emission. At this point, the crack growth through cleavage will stop, and dislocation emission from the crack tip will be activated.

The final fracture toughness, crack growth ratio and sharpness of the crack with loading after the cleavage event depends on the diffusion speed of hydrogen to the new crack tip. In the case of hydrogen activated cleavages, there would be intermittent steps of crack growth through dislocation emission and cleavage.

Lowering the hydrogen gas pressure decreases the effect from hydrogen. The plasticity is still enhanced compared to the case without hydrogen, but less enhanced compared to the cases where the hydrogen gas pressure is higher. With less effect on the line energy, the nucleation stress intensity of the first dislocation is slightly higher, and the plastic response is slightly reduced. The changes in mobility are even less, due to the much smaller bulk concentration of

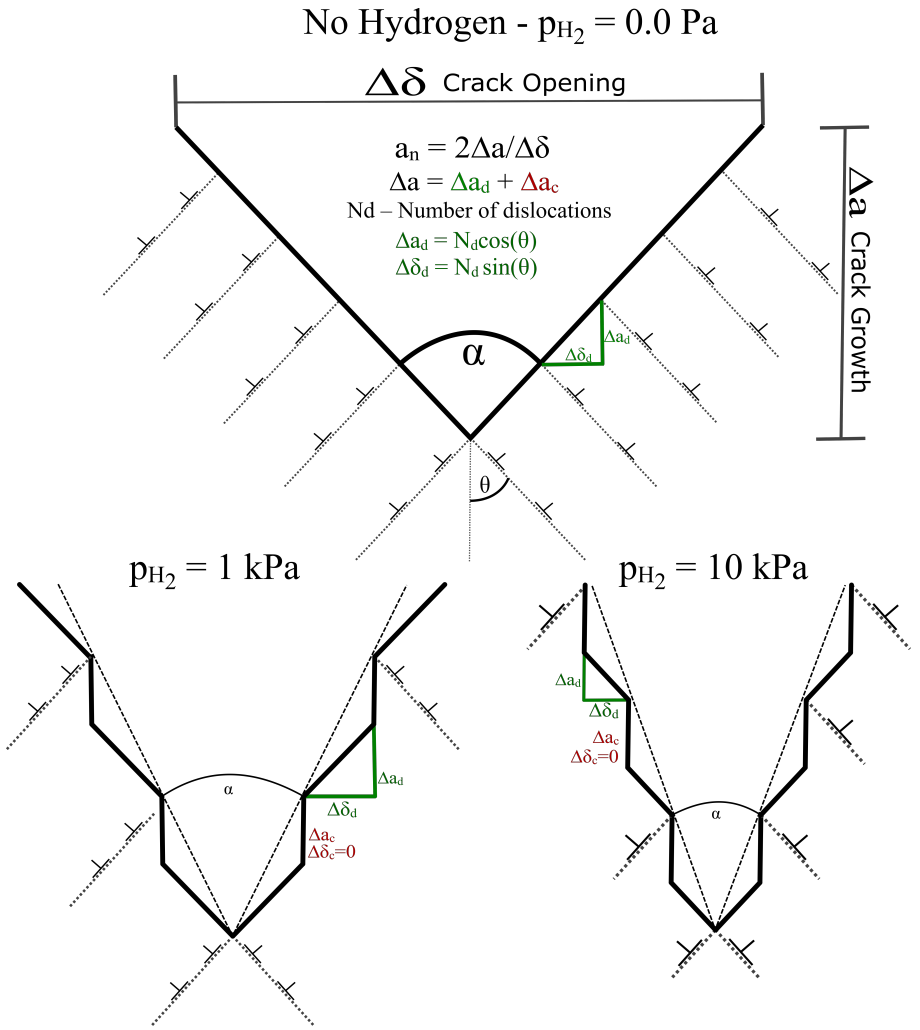

Figure 4.17: Crack growth mechanism in Fe-3wt%Si. In the cases of alternative slip, the crack grows through nucleation of dislocations from the crack tip. The crack opening angle is determined by the activated slip system given no cleavage events. With the same slip system, and with cleavage events, the crack opening angle will be smaller, i.e. sharper crack. The higher the hydrogen gas charging, the higher the hydrogen concentration within the sample. A higher hydrogen concentration means a larger hydrogen effect. A higher gas pressure leads to lower fracture toughness and sharper cracks. Δa is the crack growth and $\Delta\delta$ is the crack opening. The hydrogen gas charging conditions 1 kPa and 10 kPa results in a bulk hydrogen concentration of 0.0019 appm and 0.0061 appm.

hydrogen.

In the lower gas pressure cases, the reduction to the cleavage threshold is still considerable. The decrease to the cleavage threshold is dependent on the hydrogen potential close to the crack tip, exactly where the hydrostatic stress is at the highest. Since the base chemical potential of hydrogen is lower, a higher strain at the crack tip is necessary to reach a critical level of hydrogen concentration to activate a cleavage event. A smaller reduction in the cleavage threshold means more time for the dislocation configuration to develop, and more dislocation growth through dislocation emission. With a lower gas pressure, the fracture toughness is slightly regained, and the crack growth through dislocation emission is enhanced. Increasing the gas pressure would lead to a drop in the fracture toughness and less developed plastic zones.

HELP affects the plastic response of the crack, HEDE affects the cleavage criterion. The lowered line energy of dislocations increases fracture toughness; the lowered cleavage criterion lowers the fracture toughness. There is a competition between the two effects. An increase to the gas pressure enhances the hydrogen effect on both. Though, as the HEDE effect is more enhanced by the hydrostatic stress at the crack tip, these cases predicts a cleavage event at a lower load. The HEDE effect is shown to be the reason for activation of a cleavage event at a lower load. However, this does not rule out that HELP or other mechanisms may be at effect. This will be further discussed in chapter 6.

The increasing crack growth ratio with increasing hydrogen gas pressures does not fully capture the experimental observations. In figure 9a) in Vehoff and Rothe [45] the crack growth ratio at a hydrogen gas charging p_{H_2} of 0.3, 5 and 130 Pa results in a crack growth ratio of a_{n} of $\approx$ 5,10 and 12, respectively. The modelling results predict a crack growth ratio of a_{m} 2.64, 2.82 and 3.0 at hydrogen gas pressures of 100, 1000, and 10 000 Pa. The model underestimates the sharpening due to hydrogen gas charging, and it fails to capture the variation with varying hydrogen gas pressure.

The problem of the sharpening as a function of the hydrogen gas charging is two-fold. The first problem is that the length of the crack growth through cleavage fracture is unknown. The second problem is that the crack growth ratio from the experiments [45] is an average of crack growth through several intermittent steps. The current model ends at the first cleavage event and this study has not explored what occurs after the assumed cleavage jump.

Clearly, the crack growth due to a cleavage fracture needs further refinement. The distance of the jump could be linked to a constitutive relation. This refinement could be either a phenomenological relation for the displacement jump or solving the distance using additional simulation techniques. A constitutive framework or simulation technique could handle both the fracture criterion and the following crack growth. A better description of the cleavage would allow the model to expand the simulation to include several steps of crack growth alternating between ductile behaviour and cleavage fracture. The alternating crack growth should be dependent on loading conditions(loading rate), charging conditions(gas pressure) and material system(dislocation mobility, hydrogen affinity and diffusion speed).

4.6 Conclusion

The effect of hydrogen on the fracture behaviour of BCC iron has been investigated by applying the defactant concept within a 2D Discrete Dislocation Dynamics simulation. The defactant framework has been used to implement the HELP and HEDE mechanisms. The work presented

in this chapter has not explained how hydrogen can cause the effects, but rather investigate the implications of HELP and HEDE. An important outcome of this work is the implementation of the defactant framework. This implementation of the defactant framework can replicate material behaviour previously seen in experiments, which has previously been linked to the hydrogen mechanisms HELP and HEDE. The defactant framework evaluates the magnitude of the hydrogen effect based on the chemical potential, which mean this implementation can also integrate the effect of different charging conditions.

The simulation results indicate that a reduction in the elastic interactions between dislocation does not explain the sharpening of cracks in iron at low hydrogen gas pressures. Lowering the cleavage criterion, on the other hand, causes sharper cracks. The following conclusions have been drawn based on the model results:

a The HELP mechanism is implemented through reducing the line energy of dislocations due to the chemical potential of hydrogen. The hydrogen mechanism HELP can result in two significant changes. Both as a lowered elastic interaction between dislocations and a change to the mobility of dislocations.

   - Reducing the line energy of dislocations enhances the plastic response. Hydrogen facilitates dislocation multiplication and increases the dislocation density along the entire dislocation arrangement ahead of the crack tip. The enhanced plasticity increases the fracture toughness of the crack and the crack growth rate. The enhanced plasticity does not cause sharper cracks.
   - The hydrogen effect on the mobility of dislocations include a reduction to the formation energy of a kink-pair and a solute drag effect on kink migration. The changes to dislocation mobility are negligible at low gas pressure due to the low solubility of hydrogen in iron.

b The HEDE mechanism is implemented through lowering the cleavage criterion due to both gas charging and loading. Lowering the cleavage criterion reproduces the experimental findings of a lowered fracture toughness and sharper cracks. It can also account for the effect of changing gas pressure. A higher gas pressure means activation of a cleavage event at lower loads, leading to even sharper cracks.

The results show that a reduction to the cohesive energy of the lattice ahead of the crack tip is the most probable explanation for the observed sharpening of cracks. Though, that does not mean hydrogen does not affect the plasticity. We only show that at low gas pressures the hydrogen effect does not cause the enhanced crack growth rate and sharpening of cracks. This may not be the case at higher gas pressure or, in cases where the microstructure or loading is different. Which mechanism is dominates would depend on the mechanical loading, specimen microstructure and application of hydrogen. The work in this chapter indicates that the true hydrogen effect is most likely a hybrid of HEDE, HELP, and other mechanisms. A further discussion on how we have reached this conclusion is given in chapter 6.

Chapter 5

Nanoindentation

The defactant framework used in the previous chapter is implemented in a model for nanoindentation. Nanoindentation presents an opportunity in our investigation of the hydrogen effect on crack growth in Fe-3wt%Si. The indentation experiments offer a unique perspective on dislocation nucleation through a plastic avalanche called the pop-in. Other researchers have shown that hydrogen promotes this pop-in event [54]. Activating the pop-in at a lower load is correlated to a reduction in the line energy of dislocations. The model presented in this chapter can reproduce this experimental behaviour, using the same implementations as in chapter 4. This study is a demonstration of how the defactant framework implemented in chapter 4 can be applied to other situations.

5.1 Introduction

The defactant framework utilized in the previous chapter is implemented here with the same hydrogen parameters and comparable charging conditions. As we have pointed out earlier the wealth of studies into the hydrogen embrittlement show a multitude of hydrogen effects. A challenge with understanding hydrogen embrittlement is to know which hydrogen mechanism is critical. The value of having a unified implementation of the hydrogen effect within the thesis makes cross referencing possible. In this way, the implementations done in chapter 4 can be tested and checked with another model against different experimental results. The main purpose of the work described in this chapter is to do exactly that, an extra check on the assumptions made in chapter 4.

The work in this chapter will model load-controlled nanoindentation and the hydrogen effect using dislocation theory and the defactant framework. The model will be validated against a previous experimental study on nanoindenting Fe-3wt%Si with and without hydrogen [54]. The model in this chapter is a different approach from the 2D DDD (Chapter 4). The model for nanoindentation attempts to estimate the amount of elastic and plastic deformation during nanoindentation, and associate it with an achieved depth of the indenter. The complexity of nanoindentation includes several challenges; the most significant are large plastic avalanches, large strain gradients and significant changes to the dislocation configuration over large time periods (seconds). Also, in this model, features such as dislocation intersection and junction formation cannot be ignored.

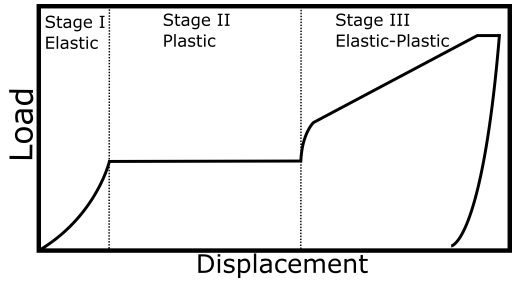

Figure 5.1: Schematic of a load-displacement curve from nanoindentation testing. There is an initial elastic response of the material, and then an elastic-plastic response after the pop-in is activated. The three distinct stages are: Stage I) Elastic loading, Stage II) Pop-in and Stage III) Elastic-plastic

The simulation model is based on the work by Srikanth and Ananthakrishna [36]. Ananthakrishna et al. have introduced several methods of addressing plastic instabilities in metallic materials; Portevin-Le Chatelier effect [103], displacement controlled nanoindentation [35] and load-controlled nanoindentation [36]. These models can describe transient dynamics of plastic deformation by linking the deformation to the evolution of the microstructure. For example, the pop-in [36] in nanoindentation is linked to a plastic avalanche.

The model presented in this chapter is a time-dependent dislocation evolution model with the goal to encompass loading and unloading in nanoindentation in one unified description. The foundation for the model is a phenomenological modelling approach of the behaviour of metals subject to a load or strain [27, 28, 37]. The model is able to account for both elastic and plastic deformation.

We will start by describing nanoindentation in section 5.2, with the intention of laying out what exactly we are interested in capturing with the model. The basics of the model is presented in section 5.3 where we detail the model, including the hydrogen effect. The results are presented in section 5.4, following discussion in section 5.5 and the conclusions of this work are in section 5.6.

5.2 Basics of Nanoindentation

Nanoindentation is forcing an indenter into a carefully-prepared surface, either as a load-controlled (LD) or displacement-controlled (DC) testing. We will focus on load-controlled nanoindentation, where a load curve is predetermined, and the displacement achieved by the indenter is recorded. Indentation testing at microscale is mostly used to determine the hardness of a material, while indentation at nanoscale has another feature, the pop-in.

Load-controlled indentation has three stages. These stages is illustrated in Fig. (5.1), where the achieved displacement is plotted against the applied load. Stage I) is an initial elastic part. Stage II) is a large depth increase without any significant increase in force. Stage III) is an elastic-plastic response where the surface and microstructure conforms to the indenter through elastic and plastic deformation. What these three stages signify are three distinct material responses.

The initial loading, Stage I, is purely elastic and can be approximated using the Hertz so-

lution for spherical contact between two elastic bodies. In any cases of mechanical loading of a material, it will deform by whatever mechanism is available. In nanoindentation, when the material is well annealed, and the surface is well prepared, there are no nearby defects to activate plastic behaviour. The material will deform elastically until another forms of deformation can be activated. When another form of deformation is possible (dislocation nucleation and multiplication); stage II begins.

Stage II signifies an avalanche of plasticity, as the now newly formed defect makes multiplication of dislocations possible. The avalanche of plasticity lets the indenter achieve a large depth increase without any significant increase in the force. Plasticity is activated, and the activity reduces the stresses significantly. Sometimes the avalanche relaxes the lattice below the flow stress necessary to activate further deformation. In this case, there will be an elastic loading until the stresses reach the flow stress of the system. The first defect formation which initiates stage II can be linked to the nucleation of a single dislocation loop. Even when the surface is well prepared, and without defects, there can be some variation in the pop-in force. A collection of nanoindents will give a distribution of pop-ins where the higher the force, the more likelihood of a pop-in. The probability of a pop-in increase as the stress in the system is increasing. Nucleation of dislocations is a rare event due to the high stresses necessary, in the range of 2 - 10 GPa.

Stage III is the elastic-plastic response of the material, which is more similar to the plastic response of macroscale mechanical testing. Here the dislocation configuration and microstructure dictates the response, where it can be a softening, hardening or equilibrium case. The material deforms, dictated by the ease of which plasticity is activated. There is a flow stress that must be met to activate plasticity; which in turn, lead to plastic deformation relaxing the stresses in the system.

In summary, the indenter applies a stress to the material surface and lattice. The stress is a function of the load and area of contact between the indenter and the surface. The system deforms in whatever way is possible. Both elastic and plastic deformation can conform to the indenter, increasing the area of contact between indenter and surface. An increase to the area of contact reduces the stress in the system. Elastic deformation is recoverable, while plastic deformation is not. The model presented in section 5.3 is designed to capture these features of nanoindentation, and connect them to micro-structural evolution processes.

5.3 The Model

This model aims to describe both the elastic and plastic behaviour of the material during nanoindentation in all three stages. Other nanoindentation models solve each stage separately. This model is different by modelling all stages with a unified description. With further development, we can use the model to fit the elastic-plastic stage with the dislocation mobility and constitutive relations for the evolution of the microstructure. The hydrogen effect in this study is a reduction in the line energy of dislocation. Further development could also lead to an investigation into hydrogen's effect on the elastic-plastic stage.

The model is unified over all stages, and all forms of deformation are numerically possible at all times. The elastic and plastic deformation occurs due to a stress σ that is imposed by the indenter, described in section 5.3.1. The elastic and plastic deformation due to the stress depends on the evolution of the microstructure and plastic deformation. This model does not simulate

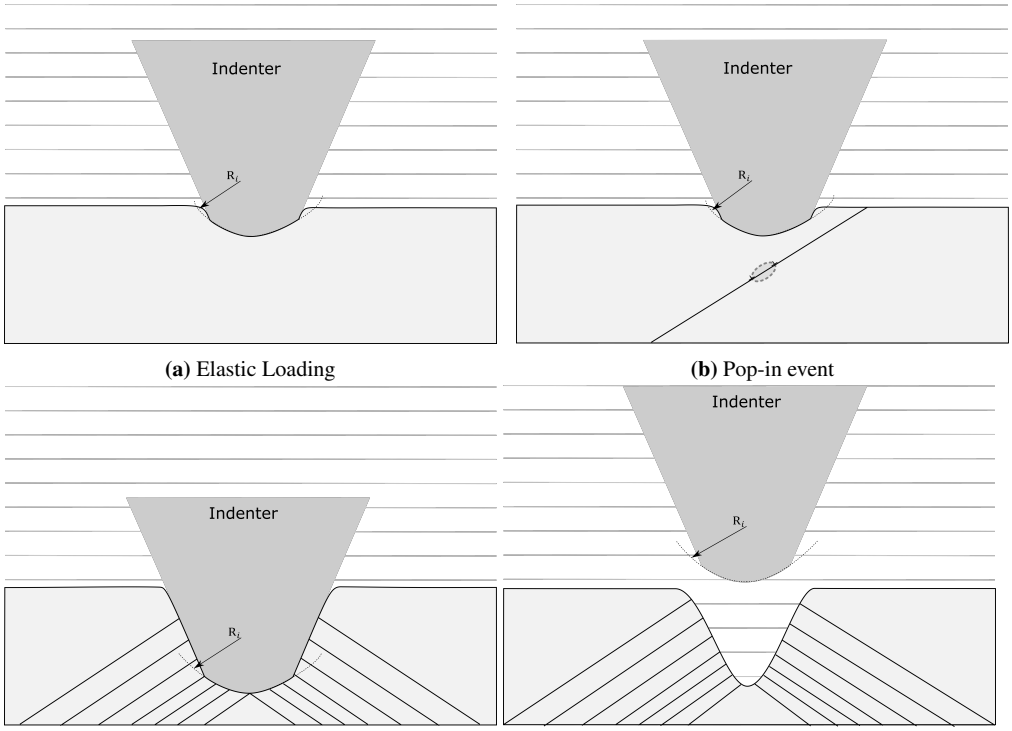

(a) Elastic Loading

(b) Pop-in event

(c) Elastic-Plastic Loading

(d) Unloaded

Figure 5.2: A schematic of distinct steps during the indentation. The first part of indenting into the material is an elastic loading. At the pop-in, a defect is formed, activating much easier forms of dislocation multiplication. The multiplication of dislocation and dislocation slip effectively accommodates the indenter, reducing the stresses in the system by increasing the area of contact which the load is distributed over. The plastic activity can be observed after unloading with the deformation of the specimen surface.

discrete dislocations as in chapter 4, but rather describes the system through three scalar state variables. The microstructure is described by two state variables, the mobile ρ_{m} and forest ρ_{f} dislocation density. The amount of plastic deformation is described by the plastic strain ϵ_{p}. The evolution of the three state variables is found through rate equations, described in section 5.3.2. The hydrogen effect in this model is implemented through the defactant framework, given in section 5.3.3. The hydrogen reduces the line energy of dislocations γ_{disl} as a function of the chemical potential of hydrogen μ_{H}. The final displacement z of the model is a function of the achieved area of contact, described in section 5.3.4. An overview of the numerical implementation of this model is given in section 5.3.5.

5.3.1 The Stress

The microstructure evolves due to a stress σ beneath the indenter. The stress beneath the indenter is a function of the load P divided by the area of contact πa_{c}^2. The circle of contact a_{c} when a spherical indenter is forced into another elastic body is based on the load P, the reduced

Property	Symbol	Value
Young's Modulus specimen [GPa]	E_{s}	211
Young's Modulus indenter [GPa]	E_{i}	1140
Poisson's ration specimen	ν_{s}	0.29
Poisson's ration indenter	ν_{i}	0.07
Reduced Elastic Modulus [GPa]	E^*	191.91
Radius of the indenter [μm]	R_{i}	1.75
Taylor relation	M	3
Shear Modulus [GPa]	G	82
Lattice constant [nm]	a	0.2875
Burgers vector	b	$\sqrt{3}a/2$
Velocity prefactor [m/s]	v_0	40
Kink-pair formation energy [eV]	Q_{kp}	0.69
Speed of sound in Fe [m/s]	$v_{\max}$	3000
Temperature [°K]	T	300
Disl. Mult. prefactor[1][m^{-1}]	δ	10
Disl. Nuc. att. freq.[2][s^{-1}]	v_D	10^9

[1] Prefactor for dislocation multiplication, an inverse length scale.
[2] Attempt frequency for dislocation nucleation of a loop.

Table 5.1: Fixed input parameters for the simulations of nanoindenting Fe-3wt%Si presented in this chapter. A separate table is given later for parameters that will be tested in this work

modulus E^* and the effective radius R_{eff}. The circle of contact a_{c} between indenter and the surface is

$$a_{\mathrm{c}}^3 = \frac{3PR_{\mathrm{eff}}}{4E^*}. \tag{5.1}$$

E^* is the reduced elastic modulus between the indenter and specimen. $1/E^* = (1-\nu_{\mathrm{i}}^2)/E_{\mathrm{i}} + (1-\nu_{\mathrm{s}}^2)/E_s$, where ν is the Poisson's ratio and E is the elastic modulus, the subscript denotes the indenter i and specimen s. The same material is modelled here in chapter 5 as is used in chapter 4. The fixed parameters are presented in table 5.1. The reduced elastic modulus is assumed to be constant regardless of deformation.

The effective tip radius R_{eff} will change during loading as the plastic activity beneath the indenter causes irreversible deformation to the surface, changing its shape. The surface conforms to the indenter, contributing to a relaxation in the lattice. The effective radius is

$$\frac{1}{R_{\mathrm{eff}}} = \frac{1}{R_{\mathrm{s}}} + \frac{1}{R_{\mathrm{i}}}, \tag{5.2}$$

where R_{s} is the effective radius of the curvature of the surface and R_{i} is the radius of the indenter. The concept of Eq. (5.2) is illustrated in Fig. (5.3), where the curvature of both indenter and surface is transformed into a representative larger indenter on a perfectly flat surface. The initial conditions assume a perfectly flat surface, meaning that $R_{\mathrm{s}} = \infty$, and $R_{\mathrm{eff}} = R_{\mathrm{i}}$. When plastic deformation is activated, the surface will conform to the indenter. The radius of the spherical

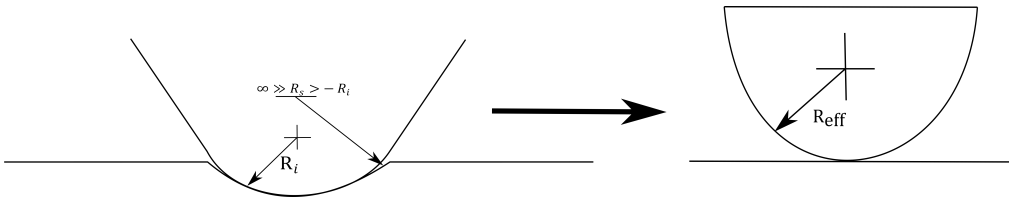

Figure 5.3: The Hertz theory of contact between two elastic bodies. The area of contact is a function of the load P, reduced elastic modulus of the specimen and surface E^*, and the effective tip radius R_{eff}. The effective tip radius is a function of the curvature of the indenter and surface. The model connects plastic deformation with a change to the curvature of the surface. Plastic deformation effectively changes the curvature so that the area of contact is increased; this reduces the stresses in the system.

indenter tip is fitted from the experimental values as $1.75\ \mu\text{m}$. The radius of the concave surface will evolve with the amount of plastic activity, described below.

The Plastic deformation of the surface

The relation between the plastic deformation and the deformation to the surface is found by linking the effective radius of the surface R_{s} with the plastic strain ϵ_{p}. The change in the effective surface radius is calculated through an observational relation

$$R_{\text{s}} = -R_{\text{i}}/\epsilon_{\text{p}}. \tag{5.3}$$

The increasing plastic strain beneath the indenter causes the radius of the surface to approach the radius of the indenter. The closer R_{s} is to R_{i}, the higher the area of contact is established between indenter and specimen surface. An increase in the area of contact relaxes the stresses. The effective curvature of the surface is $R_{\text{s}} \approx -R_{\text{i}}$ when $\epsilon_{\text{p}} \approx 1$. When the radius of the effective curvature of the surface approaches the radius of the indenter, the effective radius, and consequently area of contact approaches infinity, reducing the stresses to zero. The relation presented in this subsection accounts for the relaxation in the system through plastic deformation.

Glide stress

The glide stress on the mobile dislocation density is an effective resolved glide stress τ^*. The τ^* is a function of the imposed stress and the back stress of the forest dislocation density

$$\tau^* = \sigma/M - \tau_{\rho_{\text{f}}}. \tag{5.4}$$

Here $\tau_{\rho_{\text{f}}}$ is the back stress of the forest dislocation density. M is the Taylor factor, which is a general approach to resolving the imposed stress on a dislocation into a glide stress.

The back stress $\tau_{\rho_{\text{f}}}$ of the forest dislocation density is accounted for through a phenomenological relation. The effective force $\mathbf{f}$ on a dislocation is equal to the product of the resolved glide stress τ and its Burgers vector. It is assumed that the line energy density γ_{disl} of a dislocation primarily depends on the shear modulus G and the length of the burgers vector b, $\gamma_{\text{disl}} \approx Gb^2$. The interaction from between dislocations is then $\mathbf{f} = \tau b = Gb^2/L$, where L is the distance between the dislocations. A measure of the average distance between dislocations is the dislocation density ρ, which means that $L \approx \alpha/\sqrt{\rho}$. The estimation of the internal

stress would then be $\tau_{\rho_f} = \alpha G b \sqrt{\rho}$, where α is a dimensionless prefactor taken to be 0.3. A well-annealed metal has a low internal stress, with a dislocation density in the range of 10^{10} to 10^{12} $1/\mathrm{m}^2$. The average distance between dislocations with a density of 10^{12} is $1\mu\mathrm{m}$, and the internal stress would be around $\tau = 6\mathrm{MPa}$. More heavily worked materials have much higher dislocation densities of up to 10^{16} $1/\mathrm{m}^2$, which correspond to internal stresses of $\tau = 600\mathrm{MPa}$.

The condensed version of subsection 5.3.1 is that the stress beneath the indenter is controlled through the imposed load and the area of contact between indenter and the surface. During the elastic stage, the effective tip radius is equal to the tip radius of the indenter, as the surface is flat. Plastic deformation is activated by an effective shear stress τ^*. When plasticity has been activated, the system will relax the stresses by conforming to the indenter shape through plastic deformation. The relaxation of the stresses is captured by increasing the effective radius. The increase to the effective tip radius is implemented by establishing a relation between the plastic strain and the radius of the surface.

5.3.2 Time Evolution Model

The plastic deformation depend on a scalar state parameter, the plastic strain ϵ_p. The rate of change in the plastic strain depends on the microstructure, which is described through two state parameters. The microstructure is generalized as two sets of dislocation densities. These two scalar state parameters are the mobile dislocation density ρ_m (glissile dislocations) and the forest dislocation density ρ_f (sessile dislocations). These three state parameters are solved for time, where the time-dependence enters through the prescribed load-function (The same as is used experimentally).

Most work hardening models describe the evolution of the dislocation densities due to the imposed strain into the system $\mathrm{d}\rho/\mathrm{d}\gamma$. Our approach is different, where the evolution of the dislocation densities and plastic strain is dependent on time.

Plastic Strain

The amount of plastic deformation is represented by the plastic strain ϵ_p. Plastic strain is local deformation of the lattice through dislocation multiplication and movement. The plastic strain is calculated using the initial conditions and integrating the rate of change of the plastic strain over time.

The rate of change of the plastic strain is found through the Orowan equation

$$\frac{\mathrm{d}\epsilon_\mathrm{p}}{\mathrm{d}t} = b\rho_\mathrm{m} v(\tau^*). \tag{5.5}$$

Here $v(\tau^*)$ is the average velocity of the mobile dislocations. The materials ability to deform is based on its ability to move dislocations.

The velocity of the mobile dislocation density is found through the same phenomenological equation as is used in chapter 4. The velocity equation is

$$v(\tau) = v_0 \exp\left(-\frac{Q_\mathrm{kp}}{k_B T}\right) \exp\left(\frac{\tau V_\mathrm{act}}{k_B T}\right) \tag{5.6}$$

where v_0 is a velocity prefactor. Q_kp is the kink pair formation energy and T is temperature. The values of the parameters are given in table 5.1. V_act is the activation volume for kink pair formation and was set to $25b^3$ in chapter 4, that value will not be used here.

The phenomenological velocity equation (5.6) for screw dislocation assumes there is a kink-pair density along the dislocation line. This assumption is fair in regards to the infinitely long dislocation lines in the simulation model in chapter 4. However, the dislocation lines the nanoindentation model attempts to emulate are finite and in the range of nanometers. The small length of the dislocation lines means a finite space where both kink-pair nucleations can occur and a limit to the width of the kink-pair that is formed.

The kinetics of kink-pair nucleation and migration of movement depend on the size of the dislocation. A shorter screw dislocation can have a lower mobility compared to a longer screw dislocation. The reduction of the mobility is linked with the activation volume for kink-par nucleation, V_{act}. A reduction to the activation volume reduces the mobility of dislocations in Eq. (5.6). The V_{act} is therefore one of the parameters that will be tested in the parameter study in section 5.4.2.

Mobile Dislocation Density

The mobile dislocation density is the average density of dislocations close to the indentation that results in plastic deformation. When the mobile dislocation density is zero, plastic deformation does not occur. The rate of change of the mobile dislocation density $\mathrm{d}\rho_{\mathrm{m}}/\mathrm{d}t$ is controlled by the growth $\mathrm{d}\rho_{\mathrm{m}}^{+}/\mathrm{d}t$ vs the loss $\mathrm{d}\rho_{\mathrm{m}}^{-}/\mathrm{d}t$. In this work, the growth for the mobile dislocation densities are dislocation nucleation and multiplication. The losses to the mobile dislocation density are either through annihilation of dislocations (recovery mechanisms) or transformation of glissile dislocations into sessile dislocation (storage mechanisms). The overview of the rate of change in the mobile dislocation density is

$$\frac{\mathrm{d}\rho_{\mathrm{m}}}{\mathrm{d}t} = \frac{\mathrm{d}\rho_{\mathrm{Nucleation}}}{\mathrm{d}t} + \frac{\mathrm{d}\rho_{\mathrm{Multiplication}}}{\mathrm{d}t} - \frac{\mathrm{d}\rho_{\mathrm{Annihilation+m\rightarrow f}}}{\mathrm{d}t}, \tag{5.7}$$

where $\mathrm{d}\rho_{\mathrm{Nucleation}}/\mathrm{d}t$ and $\mathrm{d}\rho_{\mathrm{multiplication}}/\mathrm{d}t$ are the positive terms of the equation, serving as dislocation nucleation and multiplication, respectively. The negative term $\mathrm{d}\rho_{\mathrm{annihilation+m\rightarrow f}}$ is a loss term, accounting for dislocations intersecting, either forming sessile segments or annihilating.

Dislocation multiplication is handled through an empirical relation for the development of the mobile dislocation density through dislocation motion

$$\frac{\mathrm{d}\rho_{\mathrm{Multiplication}}}{\mathrm{d}t} = \delta\rho_m v(\tau^*)\ , \tag{5.8}$$

where δ is an inverse length scale, given in table (5.2). The empirical relation can be used when the mobility of dislocations is the primary factor in dislocation multiplication. There are other methods of implementing dislocation multiplications which have been neglected here, primarily a term to account for Frank-Read sources. Other dislocation multiplication terms, such as one for Frank-Read sources, are not included as the model is still under development, and further testing must be done before we can confidently implement specific multiplication terms.

The loss term is a function of moving dislocations encountering both moving dislocations and immobile dislocations

$$\frac{\mathrm{d}\rho_{\mathrm{Annihilation+m\rightarrow f}}}{\mathrm{d}t} = \beta\rho_{\mathrm{m}}(\rho_{\mathrm{m}} + \rho_{\mathrm{f}}). \tag{5.9}$$

The loss occurs when dislocations are annihilated or immobilised. Dislocations which move can intersect with both glissile and sessile dislocations. These intersections can lead to both annihilation of dislocations, a reduction in the total dislocation density, or a transformation of glissile dislocations to sessile dislocations. In other words, the mobile dislocations density is reduced through both annihilation and transformation into forest dislocations. Dislocation intersection occurs at a rate β. The rate of intersection is one of the parameters that will be investigated further in the parameter study in section 5.4.2.

The dislocation nucleation is the term that activates the pop-in, as it does not require any previous defects. The dislocation nucleation is

$$\frac{\mathrm{d}\rho_{\mathrm{Nucleation}}}{\mathrm{d}t} = \frac{v_{\mathrm{D}}}{\pi r^2} \exp\left(\frac{\Delta W(\tau)}{k_B T}\right), \tag{5.10}$$

where $v_D/\pi r^2$ is attempt frequency over the loop area. $\Delta W(\tau)/k_B T$ is an activation barrier dependent on the free energy for a stable dislocation loop under shear. k_B is the Boltzmann constant. The attempt frequency v_{D} is chosen based on the work of Wen and Li [104].

Dislocation nucleation is a rather uncommon stochastic process due to its high-stress nucleation threshold. The description of dislocation nucleation is based on classical nucleation theory, where the nucleation is dictated by the stability of the formed dislocation. The free energy of formation ΔW for a dislocation loop is determined by its energy and the work τb necessary to stabilise it. Dislocations are stable if the stresses are high enough to counter the attractive stresses between the loop segments. The equilibrium is

$$\Delta W = 2\pi r \gamma^*_{\mathrm{disl}}(r) - \tau b \pi r^2 \tag{5.11}$$

where the term $2\pi r$ is the length of the dislocation loop. τb is the force acting on the area πr^2 sheared by the dislocation loop. The effective line energy density γ^*_{disl} in Eq. (5.11) is a function of the loop radius r and the chemical potential of hydrogen. The effect of hydrogen on the line energy will be further discussed in section 5.3.3, for now, it is sufficient to know that the hydrogen effect will be an independent term.

γ_{disl} is the line energy of a dislocation without hydrogen, and will be estimated using the line energy for a circular dislocation loop [105]. The line energy density is

$$\gamma_{\mathrm{disl}} = \frac{2-\nu_{\mathrm{s}}}{1-\nu_{\mathrm{s}}} \frac{Gb^2}{8\pi} \left[-\ln\left(\tan\frac{r_{\mathrm{c}}}{4r}\right) - 2\cos\frac{r_{\mathrm{c}}}{2r} \right], \tag{5.12}$$

where r_{c} is the radius of the dislocation core, which is assumed to be $r_{\mathrm{c}} = 0.5b$. In Eq. (5.12) the line energy density increases the larger the dislocation loop radius r. Figure (5.4) shows the free energy of a dislocation loop as a function of the loop radius at three different shear stresses τ. In Fig. (5.4), a dislocation loop with a radius r is stable at a shear stress τ when the free energy of the dislocation loop is negative.

Forest Dislocation Density

The forest dislocation density are sessile dislocations, which represents the increasing resistance in the system to further plastic deformation. The forest dislocation density increases when dislocation intersection forms sessile segments, and decrease when sessile segments are annihilated.

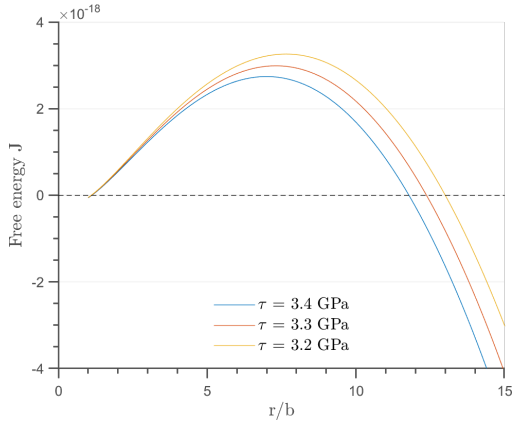

Figure 5.4: The free energy of a dislocation loop at three different shear stresses as functions of the loop radius r. This figure illustrates the stability of a dislocation loop with a radius r at the different shear stresses.

The rate of change in the forest dislocation density is

$$\frac{\mathrm{d}\rho_{\mathrm{f}}}{\mathrm{d}t} = \frac{\mathrm{d}\rho_{\mathrm{m}\to\mathrm{f}}}{\mathrm{d}t} - \frac{\mathrm{d}\rho_{\mathrm{Annihilation}}}{\mathrm{d}t} = \beta\rho_{\mathrm{m}}(\rho_{\mathrm{m}} + \rho_{\mathrm{f}}) - \beta\rho_{\mathrm{m}}(f_1\rho_{\mathrm{m}} + f_2\rho_{\mathrm{f}}). \tag{5.13}$$

The term $\beta\rho_{\mathrm{m}}(\rho_{\mathrm{m}} + \rho_{\mathrm{f}})$ represents intersections between mobile dislocations and other mobile dislocations as well as forest dislocations. The term $\beta\rho_{\mathrm{m}}(f_1\rho_{\mathrm{m}} + f_2\rho_{\mathrm{f}})$ corrects the gain term by removing the amount of intersections that leads to annihilation. f_1 is the fraction of intersection within the mobile dislocation density that leads to annihilation. f_2 is the fraction of intersections that cause annihilation when the mobile dislocation density intersects the forest dislocation density.

$f_1 = 1.0$ means that all dislocation intersection within the mobile dislocation density results in annihilation. Effectively, there is no growth to the forest dislocation density when $f_1 = 1.0$. On the other hand, setting $f_1 = 0.0$ would set all dislocation intersection to results in the formation of sessile segments. These two different cases will be tested in the parameter study. For the other parameter studies and the hydrogen study, $f_1 = 1.0$.

5.3.3 Implementation of the Hydrogen Effect

The current study is focused on testing the defactant framework implemented in chapter 4. The effect of hydrogen in nanoindentation has already been studied experimentally for Ni [106, 107], FeSi[54], super duplex steels [108] and TWIP steel [109]. The common behaviour found in all these systems is a drop in the pop-in force when enough hydrogen charging is applied. Hydrogen promotes the stochastic pop-in event. The lowered pop-in force has been correlated with a lowering of the line energy of dislocations[53]. With a lowered line energy, a dislocation loop is stable at a lower load. In this study, we aim to replicate the relation between pop-in force and reduction of line energy. This is also a first step in estimating the hydrogen effect on the evolution of the microstructure during nanoindentation.

The lowering of line energy is implemented through the same defactant framework as in section 4.3.1. The defactant framework describes the influence of hydrogen through reduced energy of defects. In this study, hydrogen impacts the line energy of a dislocation γ_{disl}. This study makes no assumptions to what exactly hydrogen affects on the dislocation loop to cause the lowering of the line energy. The hydrogen effect is implemented as an independent term. The effective line energy of the dislocation loop is then

$$\gamma^*_{\text{disl}} = \gamma_{\text{disl}}(r) - \gamma_{\text{H}}(\mu_{\text{H}}). \tag{5.14}$$

Here, the line energy of a dislocation γ_{disl} without the hydrogen effect is found through Eq. (5.12), and is dependent on the loop radius r. The change in the line energy due to hydrogen is $\gamma_{\text{H}} = \Gamma_{\text{H}}\mu_{\text{H}}$. Γ_{H} is the excess amount of hydrogen at the dislocation, and μ_{H} is the chemical potential of hydrogen. The Γ_{H} is assumed constant and set as 8.1×10^{-15} mol/m, which best fits the data in Fig. 4 in Barnoush et al. [54], between 5 and 20 kJ/mol. The change in the line energy of the dislocations is based on the nanoindentation study [54]. The resulting load-displacement curves are also used as validation for this study. This presents an opportunity to examine the consequences of the simplification made in chapter 4, where the Γ_{H} was assumed to be constant.

The chemical potentials for hydrogen used in our model are equivalent to the charging condition in Barnoush et al [54]. In [54], the application of hydrogen is achieved through electrochemically charging using a glycerol-based electrolyte solution [62]. This current study will test two different charging conditions of hydrogen, where the chemical potential is 4.8 or 25.5 kJ/mol. The chemical potentials of hydrogen at 4.8 and 25.5 kJ/mol represents the charging conditions -1000 mV and -1300 mV using the Eq. 7 [54].

In the more complicated alloys of super duplex steels[108] and TWIP steel[109], another observed hydrogen effect is a change in the hardness. In both cases, hydrogen increases the hardness. The increase in hardness suggests that hydrogen could be limiting dislocation mobility and multiplication. The hydrogen effect on the plastic deformation during the elastic-plastic stage is not investigated in this study.

5.3.4 The Displacement

The displacement z achieved by the indenter is the displacement of the surface from its original height $z = 0$. This displacement is found after the integration of the three state variables. The model have described the dynamics of the evolution of the microstructure and resulting elastic and plastic deformation through increasing the circle of contact a_{c} (Eq. (5.1)). The final displacement is a function of that circle of contact, with a correction to capture the unloading.

The indenter used in the experiments [54] is a Berkovitch indenter. The exact shape of the indenter is not known, but approximated by assuming a three faced pyramid with an half angle of $\phi = 70.3°$ and a spherical tip with a radius R_{i}, shown in Fig. (5.5).

The achieved displacement z is approximated through

$$z(a_{\text{c}}) = \begin{cases} a_{\text{c}}^2/R_{\text{i}} & a_{\text{c}} < a_{\text{c,h}} \\ a_{\text{c,h}}^2/R_{\text{i}} + (a_{\text{c}} - a_{\text{c,h}})/\tan(\phi) & a_{\text{c}} \geq a_{\text{c,h}} \end{cases}. \tag{5.15}$$

$a_{\text{c}} \geq a_{\text{c,h}}$ is the point where the indenter changes from a spherical shape to the conical shape. Eq. (5.15) is drawn in Fig. (5.5). Eq. (5.15) describes the height that is achieved based on the

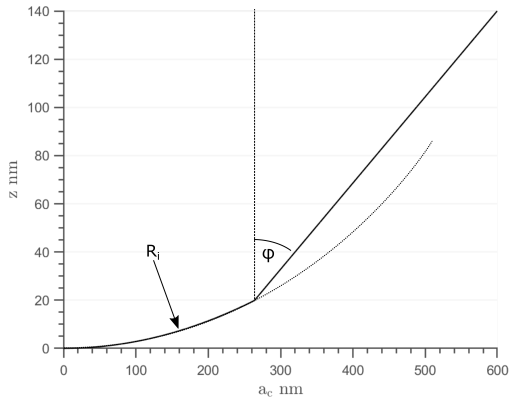

Figure 5.5: The assumed shape of the Berkovitch indenter is drawn partly by plotting the height as a function of the radius of the indenter. The indenter is three faced pyramid with a deformed tip. The deformed tip is assumed spherical with a radius R_{i}.

circle of contact, though this displacement is not the final displacement presented in the results. To capture the final displacement z during unloading we need to identified which displacement is recoverable and which is not.

The displacement in Eq. (5.15) can capture the loading, however, it fails to capture the unloading. This is corrected by splitting the displacement into two independent terms $z_{\mathrm{e}} + z_{\mathrm{s}} = z(a_{\mathrm{c}})$. The elastic displacement z_e is calculated using Hertz contact mechanics. z_{s} is the displacement achieved due to irreversible damage to the surface. The elastic displacement is recoverable when the specimen is unloaded, whereas z_{s} is not. The non-recoverable displacement is found by identifying the amount of elastic displacement, and then subtracting the elastic displacement from the displacement found in Eq. (5.15).

The elastic displacement is calculated from the load using

$$z_{\mathrm{e}} = a_{\mathrm{c}}^2 / R_{\mathrm{eff}} = \left(\frac{3P}{4E^* \sqrt{R_{\mathrm{eff}}}} \right)^{2/3}. \tag{5.16}$$

The terms are already presented in a previous section (5.3.1). The plastic deformation affects the elastic displacement through the effective tip radius. Increasing plastic deformation, i.e. increasing plastic strain ϵ_{p}, increases the effective radius. The elastic displacement achieved by load P is reduced now that the surface has conformed to the indenter.

The non-recoverable displacement is $z_{\mathrm{s}} = z(a_{\mathrm{c}}) - z_{\mathrm{e}}$. This term represents the plastic deformation to the system. This displacement is achieved as the material accommodates the indenter.

The final displacement z is then found as a function of the elastic and non-recoverable displacement, i.e. $z = z_{\mathrm{e}} + z_{\mathrm{s}}$.

5.3.5 Numerical Implementation

The model is built to estimate the elastic and plastic deformation due to load during nanoindentation. The numerical implementation integrates the plastic strain ϵ_{p}, the mobile dislocation

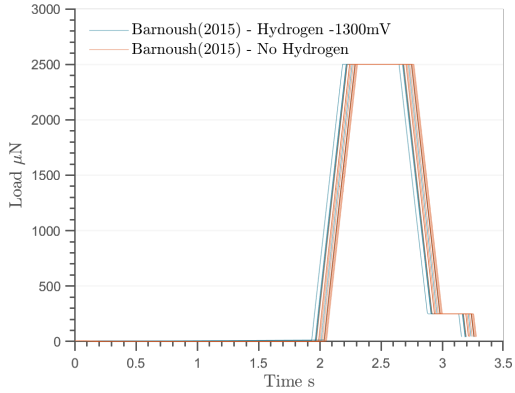

Figure 5.6: The load functions which are input into the testing apparatus, and will be the input into our model.

density ρ_{m} and the forest dislocation density ρ_{f} over time. The integration is done with the rate equation Eq. (5.5), (5.7) and (5.13) using an Runge-Kutta-Fehlberger implementation written in FORTRAN (Intel Fortran $v2019$ compiler). Aside from the experimental and material parameters, the main input into the model is the load function. The load functions used in this work are the same load functions used in the experimental study of Barnoush et al. [54], presented in Fig. (5.6).

The structure of the code is illustrated in the flow chart in Fig (5.7). The first step is initialization, where the load curve as a function of time is read, parameters are initialized and the intial conditions are set. The main do loop is m iterations, where m is the number of data points in the load function. The integration uses a Runge-Kutta-Fehlberger (RKF) method to integrate between each step n times, where the minimum amount of steps are $n_{\mathrm{min}} = 256$. Each RKF steps k_{1-6} finds the rate of change at the time t based on the current load P and microstructure $\rho_{\mathrm{m}}, \rho_{\mathrm{f}}$ and ϵ_{p}. For every step l the error e is found by the normalized difference between the fifth order Runge-Kutta y_5 step and the fourth order Runge-Kutta y_4 step. If the error becomes larger than the error threshold $e_{\mathrm{threshold}} = 10^{-5}$, the integration step j restarts with twice the amount of steps. If the integration finishes without exceeding the error threshold, the step is accepted. The number of steps returns to n_{min} and the integration continues to the next step. The algorithm continues m times until the loading is complete. After integration, in post-processing, the displacement z is calculated as a function of the circle of contact, correcting for the unloading as described in section 5.3.4.

The differential equations starts by finding the load P and the effective radius of the surface R_{s} based on the plastic strain ϵ_{p}. The area of contact a_{c} between the indenter and surface is found through Eq. (5.1) as a function of the load and the effective radius of the system R_{eff}. The area of contact is used to find the effective shear stress τ^* using Eq. (5.4), taking account of both the applied stress σ/M and the internal back stress $\tau_{\rho_{\mathrm{f}}}$. The plastic strain rate (Eq. (5.5)) is a function of the mobile dislocation density ρ_{m} and the effective shear stress τ^*. The rate of change to the mobile dislocation density (Eq. (5.7)) is a function of the mobile dislocation density ρ_{m}, the forest dislocation density ρ_{f} and the effective shear stress τ^*. The rate of change to the forest dislocation density (Eq. (5.13)) is a function of the mobile dislocation density ρ_{m}

Parameters	r m	V_{act} m^3	δ m^{-1}	β m^{-2}s^{-1}	f_1	f_2	μ_H kJmol^{-1}
Standard setup	$12.2b$	$5.5b^3$	1.0	10^{-9}	1.0	0.0	0.0
r = 11.2b	$11.2b$	$5.5b^3$	1.0	10^{-9}	1.0	0.0	0.0
r = 12.7b	$12.7b$	$5.5b^3$	1.0	10^{-9}	1.0	0.0	0.0
$V_{\text{act}} = 4.0b$	$12.2b$	$4.0b^3$	1.0	10^{-9}	1.0	0.0	0.0
$V_{\text{act}} = 6.0b$	$12.2b$	$6.0b^3$	1.0	10^{-9}	1.0	0.0	0.0
$\beta = 10^{-13}$	$12.2b$	$5.5b^3$	1.0	10^{-13}	1.0	0.0	0.0
$\beta = 10^{-6}$	$12.2b$	$5.5b^3$	1.0	10^{-6}	1.0	0.0	0.0
$f_1 = 0.0$	$12.2b$	$5.5b^3$	1.0	10^{-9}	0.0	0.0	0.0
$\mu_{\text{H}} = 4.8$ kJ/mol	$12.2b$	$5.5b^3$	1.0	10^{-9}	1.0	0.0	4.8
$\mu_{\text{H}} = 25.5$ kJ/mol	$12.2b$	$5.5b^3$	1.0	10^{-9}	1.0	0.0	25.5

Table 5.2: Overview of the fitting parameters used for the simulation cases in this chapter.

and the forest dislocation density ρ_{f}.

5.4 Results

The results in this work can be divided in three sections; the standard case, a parameter study of the model and a study on the effect of hydrogen. The standard case, section 5.4.1, represents one of the closest fits with the experimental results. The parameter study offers a more in-depth review of the model's ability to link model parameters to the plastic deformation. The parameter study is presented in section 5.4.2 and is further discussed in section 5.5.1. The study on the effect of hydrogen focuses on reproducing the lowered pop-in force observed in nanoindentation when hydrogen is charged into the sample. The hydrogen effect on the pop-in force is shown in section 5.4.3 and discussed in section 5.5.3.

The fixed input parameters for all simulations are presented in table (5.1), the rest are given in table (5.2). The model results are compared against the experimental nanoindentation on Fe-3wt$\%$Si [54]. The initial conditions for the dislocation densities and the plastic strain are set to be zero. These initial conditions are equivalent to assuming a defect-free material beneath the indenter.

5.4.1 The Standard case

The results here is referred to as the standard case. This case will serve as a comparison for both the parameter- and hydrogen study. The parameters for the standard case are chosen to replicate the experimental load-displacement curve and are compared with a indentation experiment from Barnoush et al. [54] in Fig. (5.8a). The model is compared with the experimental data through the Load-Displacement curves, specifically the force which the pop-in occurs P_{pop}, the resulting depth achieved through the pop-in Δz_{pop} and change in displacement during unloading Δz_{uL}. The resulting variables from Barnoush et al. study [54] and the model are presented in table (5.3).

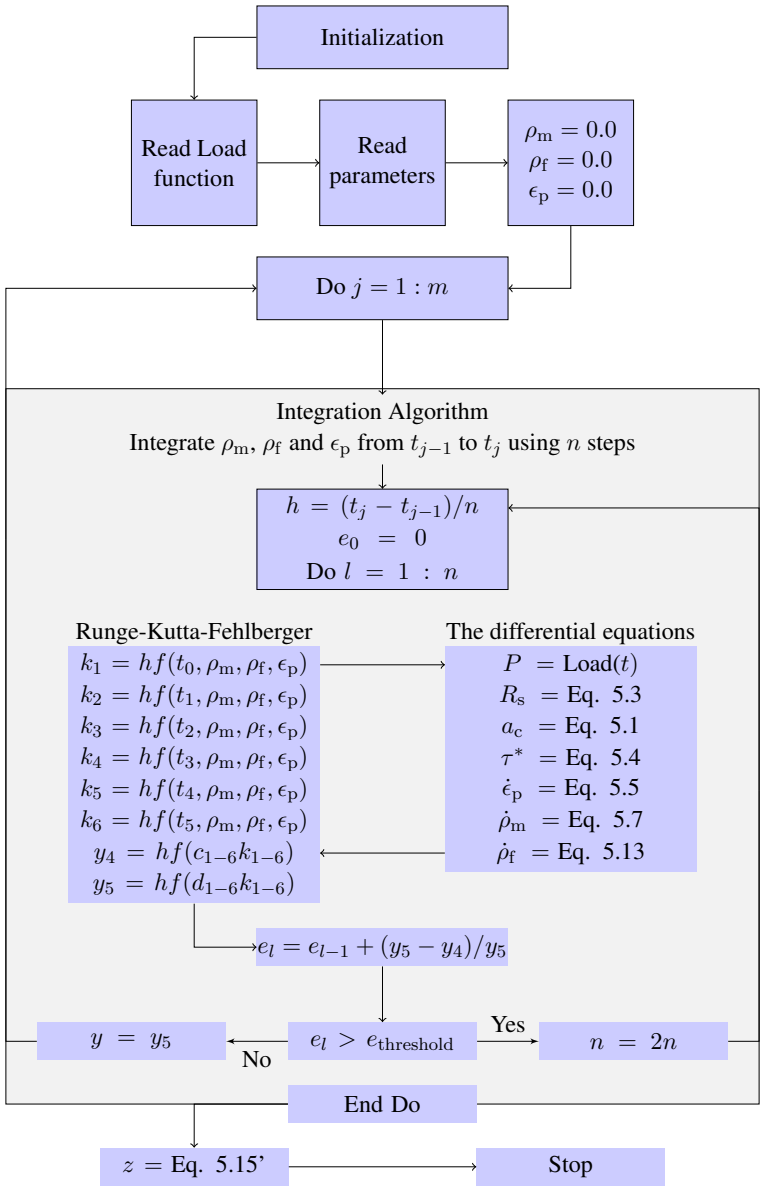

Figure 5.7: A flowchart sketching the numerical implementation of the nanoindentation model.

Case	P_{pop} μN	Δz_{pop} nm	τ_{bp} MPa	τ_{ap} MPa	Δz_{uL} nm
Barnoush et al.(2015) No H.[i]	1434	77			16
Barnoush et al.(2015) -1300mV[i]	443	11			16
Standard case model	1396	53	3292	1086	16
r = 11.2b	1573	58	3425	1103	16
r = 12.7b	1300	47	3214	1131	16
$V_{\text{act}} = 4.0b^3$	1396	32	3292	1538	19
$V_{\text{act}} = 6.0b^3$	1396	59	3292	988	15
$\beta = 10^{-12}$	1396	53	3292	1088	16
$\beta = 10^{-6}$	1396	42	3292	1270	18
$f_1 = 0.0$	1396	53	3292	1086	19
$\mu_{\text{H}} = 4.8$ kJ/mol	1268	45	3187	1135	16
$\mu_{\text{H}} = 25.5$ kJ/mol	809	26	2744	1146	16

[i] These are average values of several indents

Table 5.3: Results from the experimental study of Barnoush et al.(2015) and model simulations.

The initial conditions are equivalent to assuming no plastic deformation of the surface, and no nearby defects where dislocation multiplication can occur. The onset of the pop-in is captured through the nucleation of a dislocation loop. The Load-displacement curves between the standard case and the experimental case (Fig. (5.8a) match during the initial elastic displacement, i.e. before the pop-in. The elastic stage can be fitted by the radius of the indenter R_{i}.

The activation of the pop-in occurs at the approximately same P_{pop} for both cases. Activation of the pop-in at the same load was achieved through fitting of the loop radius r. The P_{pop} and other variables are given in table (5.3) for all simulation cases.

The model and the experiment deviates after the pop-in. The Δz_{pop} between the model and experimental indentations differs with ≈ 27.5 nm. After the pop-in, the experimental nanoindentation deforms in an elastic way up until it reaches the necessary load to activate further plastic deformation. In the model, the pop-in ends earlier, with both elastic and plastic deformation occuring after the pop-in.

The experimental elastic-plastic stage shows an approximately linear increase of displacement with increasing force. The relationship between the displacement and force during the elastic-plastic stage is dependent on both elastic and plastic deformation. The displacement achieved due to force in the elastic-plastic stage have been captured by fitting the dislocation mobility, as in fitting the activation volume V_{act}. The displacement achieved during the max loading step is also captured, which is dependent on the dislocation multiplication and the ease of plastic deformation through increasing the plastic strain in the system.

During the unloading stage, the system recovers the elastic displacement. The change in stiffness of the system before and after pop-in can be seen in the amount of elastic displacement achieved due to loading. The added stiffness during unloading is also captured by the model. The amount of Δz_{uL} for the experimental cases and the standard case is given in table 5.3.

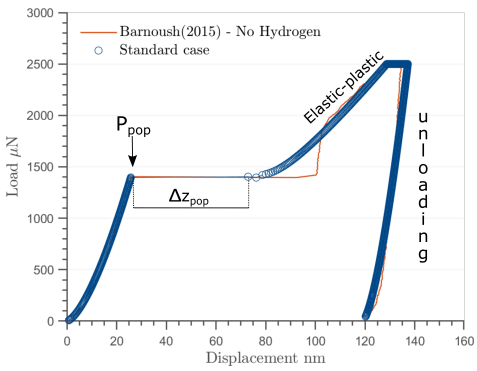

(a) Load – Displacement

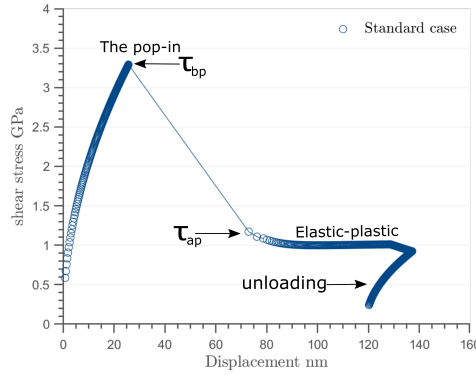

(b) Shear stress

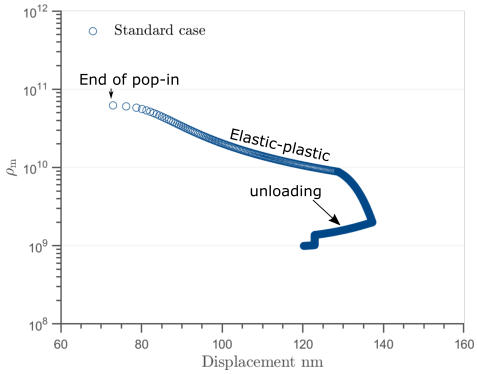

(c) Dislocation Density

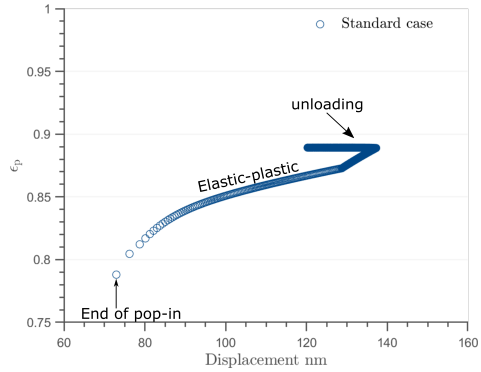

(d) Plastic Strain

Figure 5.8: The standard case is compared with a single nanoindent from Barnoush et al.'s study in a) The Load-displacement. The development of the shear stress b), dislocation densities c), and plastic strain d) during loading is presented as a function of the displacement. The variables P_{pop}, Δz_{pop}, τ_{bp} and τ_{ap} are explained in the text and given in table 5.3.

The corresponding shear stress beneath the indenter for the standard case is presented in Fig. (5.8b). The shear stress builds up to the point of the pop-in τ_{bp}. At the pop-in nucleation of a dislocation loop with a radius r is now stable. Plastic deformation is now possible, and the systems reduces the shear stress in the system through plastic deformation, increasing the area of contact. The system relaxes down to a shear stress at the end of the pop-in, τ_{ap}. The following elastic-plastic stage, which is seen as a linear increase in displacement vs. force, is a flat region of shear stress. The flat region in the shear stress indicates that the system has reached a steady flow stress, where the plastic deformation occurs without increasing the internal stresses. The displacement achieved during the max loading stage occurs through plastic deformation, which is shown in the shear stress as a decrease of shear stress in the system. The following unloading decreases the shear stress significantly.

In Fig. (5.8c) the mobile dislocation density is plotted as a function of the displacement. The parameter $f_1 = 1.0$, which means that all intersections within the mobile dislocation density end in annihilation. When all intersections end in annihilation, there is no formation of sessile

dislocation segments. That means no growth to the forest dislocation density. What occurs when we enable growth of the forest dislocation density will be explored later in section 5.4.2. With these parameters, the mobile dislocation density is largest at the end of the pop-in. After the pop-in, the mobile dislocation density reduces as the loss terms for the density are larger than the gain terms.

The plastic strain in Fig. (5.8d) goes from 0.00 at the start to 0.79 at the end of the pop-in. The plastic strain is a dimensionless estimation of the amount of plastic deformation, and it increases gradually during the elastic-plastic stage. The plastic deformation reduces the stress in the system through increased area of contact.

The standard setup captures the initial elastic loading, i.e. stage I. The activation of the pop-in can be found through fitting with the loop radius r of the nucleated dislocation loop. The model underestimates the plastic avalanche due to the pop-in, and the model and experimental data deviate during and right after the pop-in. The model reproduces the elastic-plastic stage, loading during max load and unloading. What follows is a more in-depth investigation of the effect of the parameters in the model. The following subsections will show that the model can link different ease of plastic deformation in systems to different load-displacement curves.

5.4.2 The Parameter Study

The parameter study offered in this section is a more in-depth investigation of the model. The parameter study investigates several parameters, all affecting the systems ability to deform through plasticity. The study shows how the ease of plastic deformation in a system can affect the achieved depth gained during load-controlled nanoindentation.

The following sub sections will investigate specific material mechanisms through varying related parameters. The term for dislocation nucleation activates the pop-in. We will explore the pop-in through varying the loop radius r (Section 5.4.2). The displacement achieved during the pop-in and the elastic-plastic stage depends on the ease of dislocation multiplication and dislocation mobility. The effect of the dislocation mobility is shown in Section 5.4.2, where the activation volume for kink-pair nucleation V_{act} is varied. The parameters dictating the evolution of the microstructure are simplified in this model. Though, even with the simplification, the complexity of the system is too large to cover in this chapter. We will give two brief examples in section section 5.4.2 as an illustration of what the model can be capable of. The rate of intersection between dislocation is tested by varying β; these results are presented in Fig. (5.11). The last study changes the ratio of dislocation intersection that results in annihilation. By lowering the ratio of annihilation f_1, the formation of sessile segments can occur, and the forest dislocation density grows. The growth of the forest dislocation density shows how the model can capture the build-up of internal stresses, presented in Fig. (5.12).

The Pop-in and the Loop Radius

This subsection will investigate the impact the loop radius r has on the pop-in, and as an extension, investigate a linear relationship between the pop-in force and pop-in width. In Barnoush et al [54] the relationship between the pop-in force and width is linear. A higher pop-in force increases the length of the displacement jump during the pop-in.

By varying the inputted loop radius r, the P_{pop} changes. The larger the dislocation loop radius, the lower the P_{pop}. The pop-in event is activate when a nucleated dislocation loop is

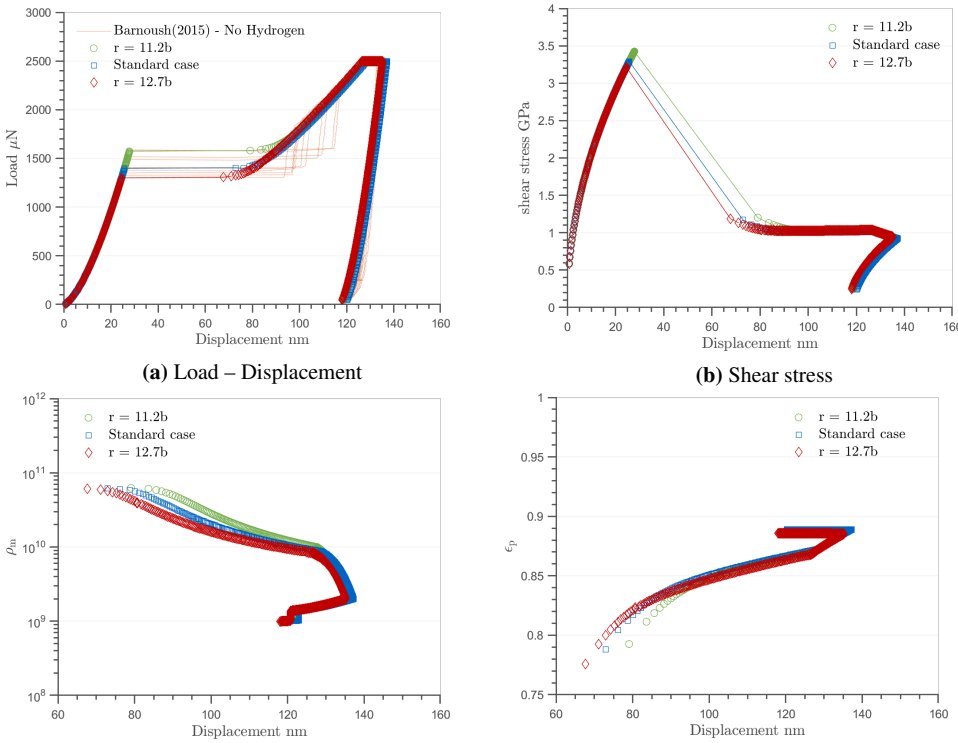

(a) Load – Displacement

(b) Shear stress

(c) Dislocation Density

(d) Plastic Strain

Figure 5.9: Three modelling cases with different radii are overlapped with a set of experimental indents from the Barnoush et al. study. The different loop radii activate the pop-in at different loads. Activation of the pop-in at different forces leads to different pop-in widths. The linear relationship between the pop-in force and displacement will be linked to the shear stress, notice how all three cases drop down to the same shear stress level after the pop-in.

stable, dependent on the relation in Eq. 5.11. The stability of a dislocation loop in this model depends on its loop radius r and corresponding dislocation energy $\gamma_{\text{disl}}(r)$. The model can activate pop-in events at different loads based on changing the loop radius r of the nucleated dislocation loop. The three cases in Fig. (5.9) are different only in the loop radius r. The case $r = 11.2b$ corresponds to the case with the highest P_{pop}. Increasing the loop radius r decreases the force necessary to activate the pop-in. The variable parameters are given in table (5.2), and the results are presented in Fig. (5.9) and table (5.3).

A pop-in at a lower load means that the pop-in occurred at a lower stress compared to a pop-in at a higher load. Before the pop-in, at the moment of the dislocation nucleation, the three different pop-in forces 1573, 1396 and 1300 μN corresponds to shear stresses (τ_{bp}) of 3425, 3292 and 3214 MPa. The effective shear stress in the system at the end of the pop-in (τ_{ap}) for the three cases are $1086, 1135$ and 1146 MPa, respectively. The pop-in is activated within a range of 548 MPa. The effective shear stress at the end of the pop-in for the three cases for r differs by 60 MPa. The effective shear stress variation at and after the pop-in is further

discussed in section 5.5.2.

The plastic deformation that occurs after the pop-in is similar in all cases as the dislocation multiplication and mobility parameters are the same. The pop-in width, amount of mobile dislocation density and plastic strain show small differences right after the pop-in. The small differences in the microstructure after the pop-in does not significantly affect the final plastic deformation.

The Plastic Deformation

The second feature we will investigate is the effect of dislocation mobility on the plastic deformation. A higher dislocation mobility means that plastic deformation occurs at lower stresses. This is modelled through changing the activation volume for kink-pair nucleation, V_{act}. Fig. (5.10) shows the result from the model for three cases and one experimental from Barnoush et al.[54]. The cases from the model are the standard case and two other cases with different activation volumes for kink-pair nucleation.

The significant changes between the three cases from the model is the ease of plastic deformation. All cases activate the pop-in at the same load, however, the pop-in width varies, see Fig. (5.10a). The lower the mobility of dislocations, i.e. lower activation volume, the smaller the pop-in width. With a lower dislocation mobility, the plastic avalanche that occurs at the pop-in causes less plastic deformation, as in less plastic strain at the end of the pop-in, see Fig. (5.10d). The effect of lowered mobility can also be seen in the shear stress, where the flow stress at the end of the pop-in for each case differs, see Fig. (5.10b) and table (5.3) for specific values. A lower dislocation mobility affects the flow stress during the elastic-plastic stage, which also can be seen as a higher hardness in the load-displacement.

The Microstructure Evolution

The study in this subsection will be a brief glimpse in changing two of the parameters that dictate the evolution of the microstructure. The first is the rate of intersection, β; the second is the fraction of intersection that leads to annihilation within the mobile dislocation density, f_1.

The rate of intersection β is a fitting parameter dictating the rate the mobile dislocation density intersect either within itself or with the forest dislocation density. The higher the β, the more intersections occur, leading to a higher rate of annihilation and, if possible, growth to the forest dislocation density. The standard case and two new cases are presented in Fig. (5.11), each case differs only in the rate of intersection, see table (5.2) for specifics. The values for the P_{pop} and others are presented in table (5.3).

The nucleation of a dislocation loop occurs at the same stage, activating plastic deformation at the same load. When plastic deformation is possible, changing the rate of intersection changes the plastic response. In the previous study, the dislocation mobility affected the plastic deformation. A higher mobility leads to a lower flow stress in the system, and more plastic deformation. Here, in this study, we show the impact of the evolution of the microstructure on the flow stress. With a higher rate of intersection, i.e. $\beta = 10^{-6}$ the loss term to the mobile dislocation density is greater compared to the standard case. As we still only allow for annihilation, there is no growth to the forest dislocation density.

The loss to the mobile dislocation density in the $\beta = 10^{-6}$ case is higher compared to the standard case. The less mobile dislocation density available, the higher the shear stress has to

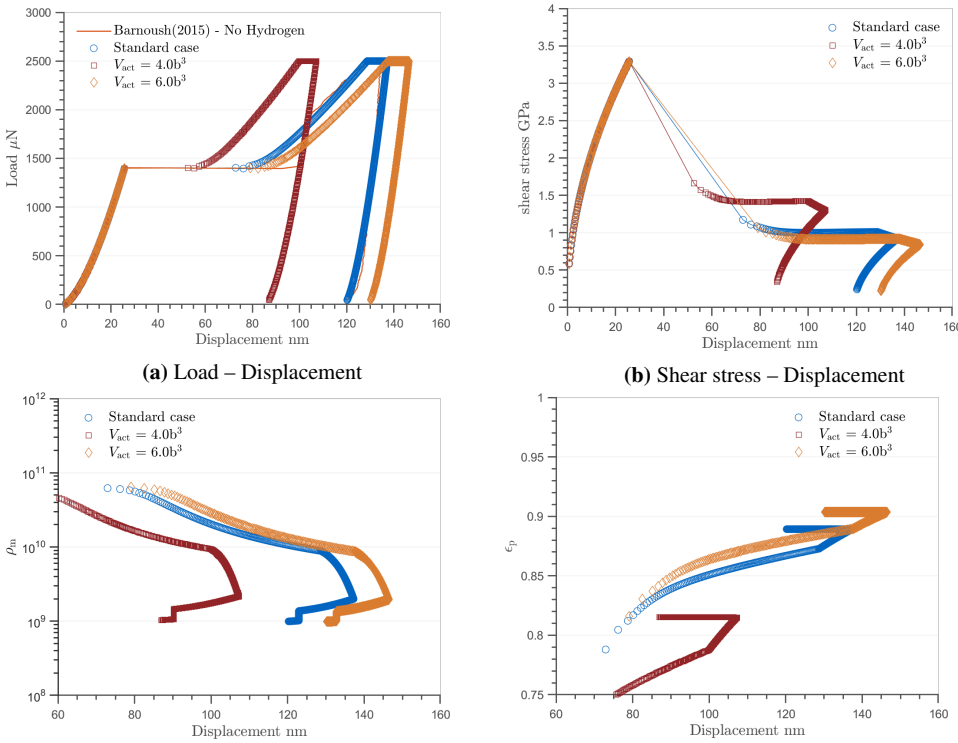

(a) Load – Displacement

(b) Shear stress – Displacement

(c) Dislocation Density

(d) Plastic Strain

Figure 5.10: The figure includes three simulations with different dislocation mobilities together with a subset of the experimental Load-Displacement curves from Barnoush et al. In a) notice how the mobility of dislocations dictate the achieved displacement, both during the pop-in and in stage III. The lower the dislocation mobility, the harder it is to deform plastically. The increase in hardness can also be observed in b) where the steady flow stress of the system differ between the dislocation mobilities. The reduced plastic deformation in d) is a direct results of the reduced dislocation mobility.

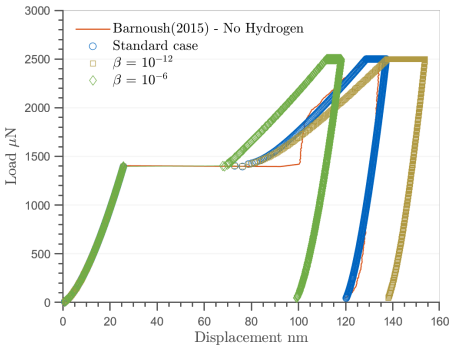

(a) Load – Displacement

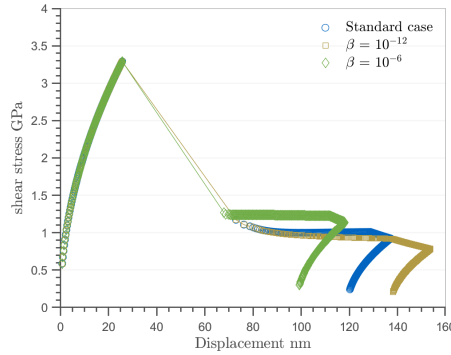

(b) Shear stress

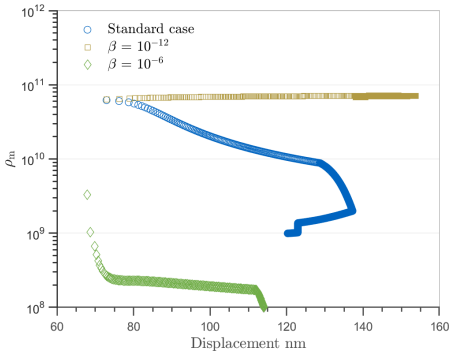

(c) Dislocation Density

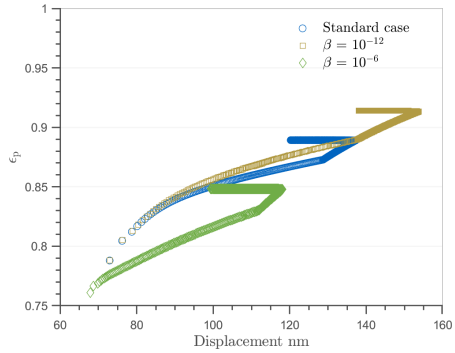

(d) Plastic Strain

Figure 5.11: Three simulations illustrating the effect of the rate of intersection β on the plastic deformation. The higher the rate of intersection, the larger the loss to the mobile dislocation density. The loss to the mobile dislocation density affects the ease of plastic deformation. A higher loss to the mobile dislocation density increases the flow stress of the system.

be to activate plastic deformation.

A lower rate of intersection, i.e. case $\beta = 10^{-12}$, shows the another behaviour, where the loss term to the mobile dislocation density is smaller than the growth term. When the growth term to the mobile dislocation density is largest, there is a relaxation in the system. Less stress is needed to activate the necessary plastic deformation to accommodate the indenter.

Changing the rate of intersection has shown one way the evolution of the microstructure can affect the load-displacement curves from nanoindentation. The evolution of the microstructure affects the plastic response of the system to the load. The results will extend the importance of the microstructure and its evolution during the indentation. The above results are simplified in one essential way. Any intersection between mobile dislocations results in annihilation, which means that there is no build-up of sessile dislocation segments, i.e. the forest dislocation density is null at all times. The ratio of annihilation will be changed in the next results, and the forest dislocation density will grow.

The effect of setting parameter $f_1 = 0.0$ is shown in Fig. 5.12, where it is compared against the standard case($f_1 = 1.0$). The growth in the forest dislocation density is changed, and at a rate of intersection β, all intersection leads to growth in the forest dislocation density. Intersections between the mobile dislocation density and the forest dislocation density also result in further growth of the forest dislocation density as $f_2 = 0.0$. The consequences of a large growth in the forest dislocation density is a large loss to the mobile dislocation density. The increasing forest dislocation density also increases the flow stress, as the back stress from the forest dislocation density counters the imposed stress from loading. The growth in the forest dislocation density, and larger loss to the mobile dislocation density, leads to a hardening in the system.

This final study is only scratching the surface of the different evolution's of the microstructure that is possible. With no growth in the forest dislocation density the evolution of the microstructure is limited to either a growth, loss or stable mobile dislocation density. With a growth in the forest dislocation density we need to consider the build up of the internal stresses, the increased intersection between the dislocation densities and consider other dislocation multiplication sources.

5.4.3 Hydrogen Effect

The reduced pop-in forces due chemically charging of hydrogen during nanoindentation is replicated here [54]. Barnoush et al. [54] has shown that chemically charging hydrogen at a constant chemical potential decreased the force at which the pop-in occurs. The higher the chemical potential during the experiment, the larger the reduction in the pop-in force. The reduction in the pop-in force is replicated in the model by reducing the line energy of dislocations.

The charging conditions in the experimental study [54] is implemented into the simulation as a chemical potential of hydrogen. The conversion between the chemical potential of the cell and resulting chemical potential of hydrogen is explain in the experimental study [54]. Two different charging conditions are tested in this model; these are a chemical potential in the electrochemical cell of -1000 mV and -1300 mV. A chemical cell potential of -1000 mV ≈ 4.8 kJ/mol, case $\mu_{\mathrm{H}} = 4.8$ kJ/mol. Chemically charging at -1300 mV ≈ 25.5 kJ/mol, case $\mu_{\mathrm{H}} = 25.5$ kJ/mol.

The pop-in is promoted by reducing the line energy of dislocation, as is shown in Fig. (5.13a) and table (5.3). The modelling results are presented alongside two chosen indents from

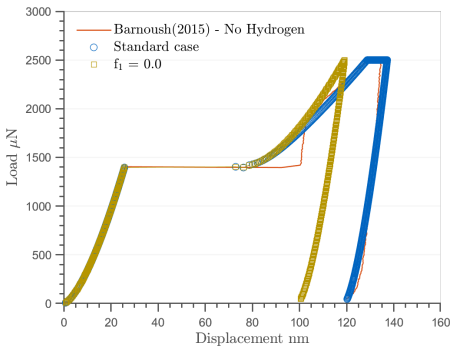

(a) Load – Displacement

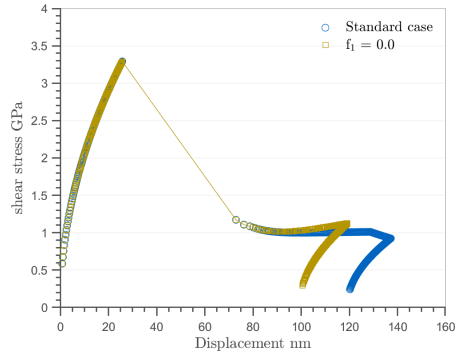

(b) Shear stress

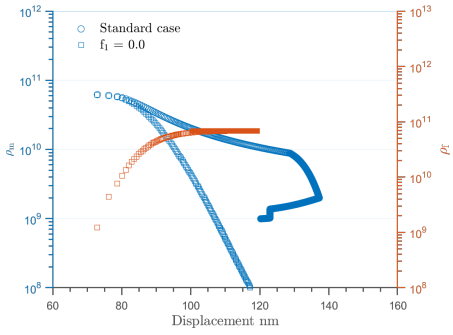

(c) Dislocation Density

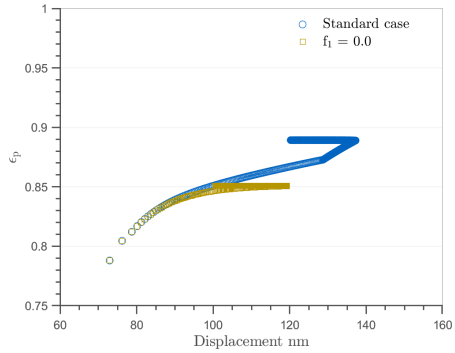

(d) Plastic Strain

Figure 5.12: The results of case $f_1 = 0.0$ illustrates the change to the plastic deformation when the growth to the forest dislocation density is enabled through f_1. Here, the new case sets $f_1 = 0.0$, which sets all intersections within the mobile dislocation density to grow the forest dislocation density. As a reminder, f_1 is the ratio of intersection within the mobile dislocation density that results in annihilation. The behaviour during the elastic-plastic stage is a hardening behaviour. The hardening occurs as the growth in the forest dislocation density increases the flow stress of the system.

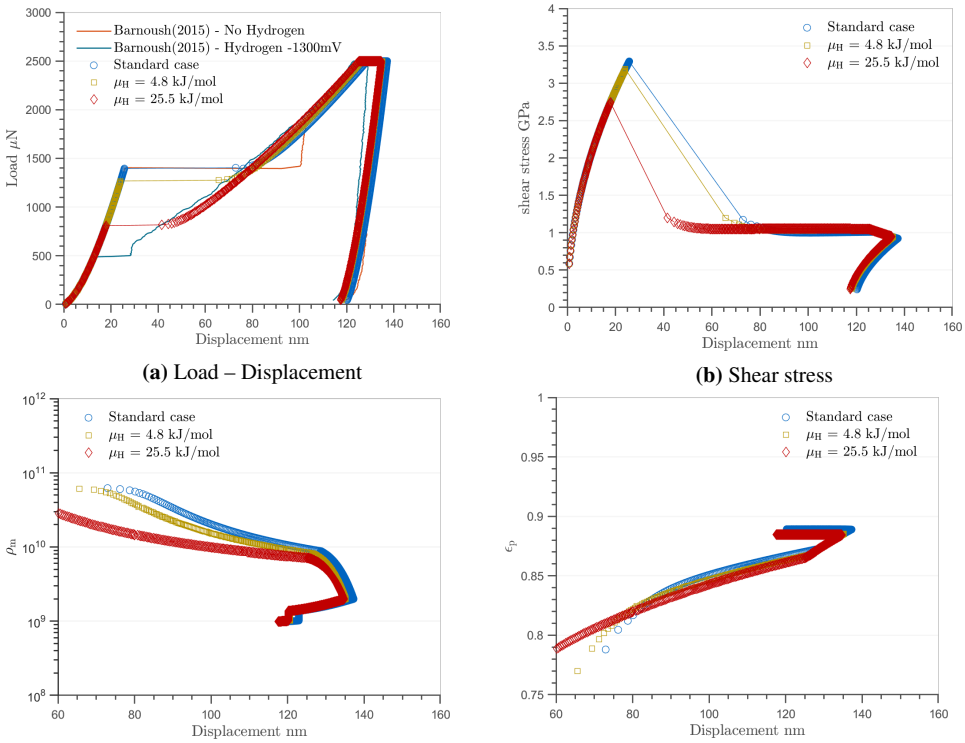

(a) Load – Displacement

(b) Shear stress

(c) Dislocation Density

(d) Plastic Strain

Figure 5.13: A study on the hydrogen effect looking at the resulting Load-displacement curves from the simulations together with two cases from the Barnoush et al.(2015) study. Simulations are at different chemical potentials of hydrogen. The lowered pop-in forces are achieved through lowering the line energy of the dislocations based on the chemical potential of hydrogen.

the experimental study [54]. The reduction in line energy is a function of the chemical potential. The higher the chemical potential of hydrogen, the larger the reduction in line energy.

The "No Hydrogen" case has a pop-in at $1396\ \mu$N. Applying a chemical potential of hydrogen μ_H at 4.8 kJ/mol reduces the pop-in force to $1268\ \mu$N. Applying a higher chemical potential of hydrogen reduces the pop-in force even further to $809\ \mu$N. For reference, the experimental values without hydrogen have an average pop-in at $1434\ \mu$N. Chemically charging at -1300 mV gives an average pop-in force of $443\ \mu$N. The reduction to the line energy manages to replicate the behaviour in lowering the pop-in force with increased charging of hydrogen. Though comparing the behaviour to the experimental data, the current implementation underestimates the reduction in the pop-in force. The pop-in force and other results from the hydrogen charging simulations are presented in table 5.3.

The reduced pop-in width is also replicated with the reduction to the pop-in width. This is similar as shown in the parameter study on the loop radius r. The achieved pop-in width has a linear relationship with the pop-in force, the lower the pop-in force, the shorter the pop-in width.

The elastic-plastic stage in the model is not considerably affected by the reduction to the line energy. The small effect on the elastic plastic stage occurs as no hydrogen effect has been implemented on the dislocation mobility or on the evolution of the microstructure.

5.5 Discussion

The parameter study and the validity of the results are discussed in section 5.5.1. The discussion will then follow with a discussion on the linear relationship between the pop-in force and pop-in width (section 5.5.2). The last section (5.5.3) discusses the implementation of the hydrogen effect in this model.

5.5.1 Parameter Study and Validity of the Model

The parameter study shows that the model can replicate an elastic loading, a pop-in, an elastic-plastic stage, a creep stage (displacement gained during max load) and unloading in one unified description. The model quantitatively captures most of the load-displacement from the experiments. The model can link each stage to material-specific processes and parameters. These parameters can then be connected to other studies through the dislocation mobility or microstructure rate equations. What the model offers is a new perspective on nanoindentation experiments.

The pop-in depth, and following elastic-plastic loading from the modelling results do not capture the experimental load-displacement exactly. At the moment, the over-relaxation seen in the experimental results, and following elastic loading are not captured. There could be several reasons for the mismatch between model and experimental load-displacement curve. One possibility is that inertial effects, which are neglected in the model, are responsible for the over-relaxation in the experiments. Another possibility is that it could be related to the evolution of the microstructure and the approximations made in the rate equations.

Neglecting the inertial effect in the dynamics of dislocation velocity could lead to an underestimation of the pop-in width. The description of the dynamics in the model uses an overdamped phenomenological equation (Eq. (5.6)) for the dislocation velocity, neglecting the time-dependence of the elastic fields and dynamics of dislocations. In reality, the dynamics of dislocation motion during the pop-in are closer to shock loading than to those during macroscale testing at typical strain rates ($\epsilon < 10^1 \mathrm{s}^-1$). The actual dynamics of the dislocation would over relax the system. The elastic stage is then a build-up of stresses in the system, and plastic deformation is activated when the stresses reach or exceeds the flow stress.

Another unknown is the accuracy of the observational relation established between the effective curvature of the surface and the plastic strain. That relation controls the relaxation of the system through plastic deformation. The relaxation is sensitive to the effective radius of curvature of the surface when it approaches the radius of the indenter. Further relaxation through plastic deformation is easy, as a small increase to the plastic strain ϵ_{p}, can lead to a large increase in the contact area.

5.5.2 The Pop-in Force and Pop-in Width

In the experimental study [54], the pop-in force has a linear relationship with the pop-in width. The exact reason for the linear relationship is not fully understood. This linear relationship also appears in the model and is due to the flow stress of the system. A possible explanation for the linear relationship is offered here.

The pop-in event experimentally is stochastic and occurs within a range of stresses dependent on the system. A pop-in at a high force corresponds to a higher stress in the system compared to a pop-in at a lower force. The variation of the effective shear stress at the pop-in varied roughly 548 MPa.

The relaxed state after the pop-in depends on the flow stress of the system. The effective shear stress at the end of the pop-in varies only by 60 MPa. The flow stress is the same for all cases. Each pop-in event will relax the system to the stress level, regardless of the stress at the moment of the pop-in. The increased pop-in width achieved during the pop-in activated at a higher load is due to increased relaxation that is necessary to relax the system to its flow stress.

The linear relationship between the pop-in force and achieved pop-in depth could be due to the relaxation that occurs during the pop-in. The pop-ins are activated at different stresses, but the flow stress of the system is close to equal. The added depth achieved at high loads is due to the additional plastic activity that has to occur to relax the system to the same stress state.

5.5.3 Hydrogen Effect

The original aim of this work was to couple the chemical potential of hydrogen to the change in line energy and mobility. The line energy could be fitted using the pop-in. The hydrogen effect on dislocation mobility could be fitted using the elastic-plastic stage. Quantifying the hydrogen effect on the line energy of dislocations and evolution of the microstructure could provide a benchmark for comparisons with other simulation models and experiments. Though as will be discussed, the model has not reached a state where we can confidently link the displacement achieved during nanoindentation to our microstructure evolution model. The lowered pop-in due to hydrogen, on the other hand, can be replicated using the defactant framework established in the previous chapter.

The hydrogen effect is implemented through the defactant framework established in chapter 4. One goal is to demonstrate the versatility with the defactant framework, where it can replicate several experimental findings and as a check on the assumptions made.

The change in the pop-in force in the hydrogen cases is a result of the hydrogen effect on the dislocation line energy. A higher chemical potential of hydrogen results in a more significant decrease in the line energy of dislocations. A lowered line energy for dislocations leads to the nucleated dislocation loop is stable at a lower load. This increased stability at a lower load activates the pop-in at a lower load.

The defactant framework implemented in chapters 4 and 5 can replicate the lowered pop-in. Though it fails to predict the magnitude of change exactly. A charging potential of -1300 mV in the experimental study had an average pop-in force at 443 μN. In our model, the chemical potential of -1300 mV corresponds to a chemical potential of hydrogen at 25.5 kJ/mol, and the pop-in force was recorded to be 809 μN.

The simplification of the framework used here is that the excess hydrogen Γ_{H} is assumed to be constant. The experimental work suggests that the excess hydrogen at the dislocation changes

with the chemical potential of hydrogen. Our simplification leads to an underestimation of the reduction in line energy when charging at higher chemical potentials of hydrogen.

The relationship between the chemical potential of hydrogen and the excess amount of hydrogen could be replicated. However, the simplification was kept to illustrate the benefits of cross checking implementations of the hydrogen effect. When the magnitude of the hydrogen effect is linked directly to the chemical potential of hydrogen, and the implementations are comparable, comparisons between experiments can be simpler, and implementation biases more apparent.

The elastic-plastic behaviour is a complex process dependent on both the mobility of dislocations and the evolution of the dislocation configuration. Nanoindentation of TWIP steel[109], can show a hardening when hydrogen is introduced. The hardening due to hydrogen is linked to an increase to the lattice friction [109], effectively reducing the dislocation mobility.

When the model can replicate the elastic-plastic stage, changes to the elastic-plastic stage could be connected to the mobility of dislocations or the evolution of the microstructure. The model would then be able to link these changes to their corresponding chemical potential of hydrogen. The dual role of hydrogen, as is seen in chapter 4, might introduce competing effects. No change to the elastic-plastic behaviour does not mean that hydrogen has no effect on dislocation mobility or microstructure evolution.

5.6 Conclusion

The effect of hydrogen on Fe-3wt$\%$Si has been investigated using a simulation model for load-controlled nanoindentation. The nanoindentation model estimates the displacement gained due to the loading imposed by the indenter. The displacement is a function of both elastic and plastic deformation. The plastic deformation is found through the evolution of the microstructure and plastic strain. The elastic displacement is found through Hertz contact theory accounting for the effect of plastic deformation to the surface. The aim of developing this model is to study the material response during nanoindentation both with and without hydrogen.

The parameter study illustrates that the model is able to replicate several features of load-controlled nanoindentation. These features can be connected to specific terms in the microstructure rate equations and parameters. The findings in this model can be combined with similar models which represent different mechanical tests and testing at different scales. Some concerns have been raised, and further testing and development must be done before we can confidently associate the nanoindentation features to specific rate equation terms and parameters.

The model and implemented defactant framework replicated the reduction in the pop-in force due to hydrogen charging. The hydrogen effect enhances dislocation nucleation by reducing the line energy of dislocations. The reduction in line energy of dislocations is a function of the chemical potential of hydrogen. A higher chemical potential of hydrogen is linked to a more substantial hydrogen effect.

Future work could use the model to quantify the hydrogen effect on dislocation line energy, dislocation mobility and other microstructural deformation processes.

Chapter 6

Final Discussion

The HEDE mechanism was shown to be the most likely cause for the experimental observations of a sharper crack in Fe3wt%Si. However, the chapter concluded that the full hydrogen effect could be a function of both HELP, HEDE and other mechanisms. This chapter addresses why the hydrogen effect on crack growth in iron should account for the other mechanisms as well.

The simulation results from chapter 4 strongly suggest that hydrogen affects the cohesion ahead of a crack tip. The results can also show that the magnitude of the effect can be correlated with the chemical potential of hydrogen. A higher hydrogen chemical potential results in a more substantial hydrogen effect. The hydrogen effect on plasticity in the 2D crack model, on the other hand, is inconclusive. The resulting dislocation configuration from the model and plastic zone from experiments are not directly comparable. The model cannot prove or disprove if the reduction of the line energy of dislocations is at effect. Just because HEDE explains the sharpness of the cracks does not mean it is the only effect that can occur.

The hydrogen effect on dislocations does not cause the sharpening in the 2D crack model, whereas in nanoindentation it is critical. The pop-in in nanoindentation is correlated to the formation of a dislocation loop. The hydrogen effect of lowering the force necessary to activate the pop-in can be explained through a reduction to the line energy of dislocations. Another study on cracks in TEM samples[50], found that hydrogen activated dislocation emission at a lower load than without. The reduction of dislocation energy may not be the only possible explanation for the results in the nanoindentation and TEM experiments. However, with the exact same implementation in both chapters, the reduced line energy can replicate both the lowered pop-in force and dislocation emission from a crack at a lower load. The exact effect of hydrogen is unknown, and observations may depend on where and how it is investigated.

Furthermore, even within our simplified 2D model, it is easy to achieve different answers to which hydrogen effect is the critical one. Lowering the line energy of dislocations enhance the plastic response from the crack tip. Lowering the cleavage criterion due to hydrogen decreased the plastic response. Essentially, these two changes starts a competition. In the current study hydrogen was always assumed to be equilibrated at the crack tip due to gas charging and load. Hydrogen accumulation due to the load on the crack tip is much more significant, and in this case, cause a cleavage event at a lower load than without the decohesion effect.

What happens if the charging conditions change? In chapter 4, we assume the SENT specimen is within a hydrogen gas environment with specific gas pressure. Our assumptions are then that the mechanical testing was done during charging and that the sample was properly charged

before testing. The chemical potential of hydrogen, is in this case, at equilibrium between the sample and the hydrogen gas. If the sample was not fully equilibrated before testing, the hydrogen concentration in the bulk would be smaller, and the effect on the line energy would be even smaller. Here the decohesion ahead of the crack would dominate as it is the closes to the hydrogen source. If the specimen was just precharged and then brought into the testing machine, the hydrogen source would be the interstitial hydrogen within the bulk. When the interstitial hydrogen is the only source of hydrogen, the hydrogen effect on dislocation line energy could dominate. The decohesion effect would be starved for hydrogen, and would very much depend on the hydrogen mobility within the sample. Enhanced plasticity in the 2D model could instead lead to the suggested mechanisms of AIDE and HESIV. When the hydrogen effect of enhanced plasticity dominates the strain at the crack would not build-up to the critical level to activate a cleavage event. As the external load is increased, the dislocation configuration both screens the stresses at the crack tip and develops a tensile field ahead of the crack. The material must deform in another way since the cleavage criterion is not reached. Hydrogen could help nucleate voids at a lower load, and together with the enhanced dislocation emission from the crack, connect the crack with the voids at a faster rate. The charging conditions can change which hydrogen mechanism enhances the crack growth rate.

A different material or microstructure in the 2D model can also change the predicted outcome. If the material tested had a much higher hydrogen solubility, then the effect of mobility on dislocation could go into effect. As has been discussed previously, the hydrogen effect on dislocation mobility could be both a softening or hardening effect. A higher hydrogen drag could pin the dislocations close to the crack tip, preventing further dislocation multiplication. Pinning of dislocations would be a self-amplifying behaviour, eventually leading to a lowered fracture toughness. A softening effect, on the other hand, could prevent a cleavage fracture, and the material would go down another deformation path. The critical hydrogen effect could then be a lowered line energy of dislocations, enhancing crack growth through dislocation emissions, possibly affecting void nucleation and growth. Assuming hydrogen lowers the energy of any defect, the entire plastic response can change depending on which defects are present in the material. Introducing a change to the crack plane and blunting systems, or adding precipitates and grain boundaries can also change the behaviour. In the case of a grain boundary, one should monitor the accumulation of stress at a grain boundary due to build-up of dislocation pile-ups. Increased stress on the grain boundary would mean elevated hydrogen concentrations. Depending on the hydrogen accumulation at the grain boundary compared to the crack tip region, and which is the weakest, hydrogen can promote both inter- and trans-granular fracture.

Future work should include linking the predictions of the model and a mechanical SENT test. The simulation of the 2D crack strongly suggested a hydrogen effect on the cohesion ahead of the crack, while any definite statements on the hydrogen effect on the energy of dislocations cannot be made. The nanoindentation model, on the other hand, strongly suggest a reduction in the energy of a dislocation. If hydrogen reduces the energy of dislocations during nanoindentation, it should also occur in other tests. The sharpening of the crack tip still occurs in the 2D crack model, whether or not the line energy of dislocations is reduced. The 2D crack model could help find what hydrogen gas pressure activates cleavage events. If the transition point for sharpening of the crack can be correlated to the model, a more thorough investigation can be done, where the hydrogen effect can be compared against other mechanical test. The comparison would be done by applying the different hydrogen mechanisms and see which recreates the

full behaviour of increasing the gas pressure. The HEDE effect alone could overestimates the sharpening of the crack, meaning that a hydrogen effect on dislocation is most likely at effect.

In summary, we have not offered an exact prediction at what critical hydrogen pressure would activate a sharpening of the crack. Nor have we presented an estimation of how much the crack growth rate is enhanced by hydrogen. The simplified 2D crack model and the dislocation evolution model are at this time not able to make these predictions. The actual value of this thesis lies in using the defactant mechanism to implement and emulate HELP and HEDE. The comparison between experiments is easier when the implementation of hydrogen is done with a common denominator, the chemical potential of hydrogen. The point is not that we have solved how exactly hydrogen assists crack growth in iron. Instead, we believe the hydrogen effect might be a hybrid of the suggested mechanisms HEDE, HELP, AIDE, HESIV and enhanced hydride formation. The way forward could be to use the defactant framework to approximated these mechanism by assuming that hydrogen lowers the energy of defects.

Chapter 7

Final Conclusion

Perhaps the most infuriating issue with hydrogen embrittlement is different answers are found dependent on the type of testing. Hydrogen embrittlement seems to be a combination of several mechanisms and which one will be dominant depends on the material (phase, chemical composition), hydrogen charging conditions, mechanical testing and temperature. In our work, we show that the defactant framework can replicate the hydrogen mechanisms HEDE and HELP, and found that the critical mechanism is system-specific.

Our suggestion to develop our understanding of hydrogen embrittlement further would be establishing standardized tests, where the chemical potential of hydrogen and the location of deformation are known. Experimental test can be designed to estimate the energy change in defects due to hydrogen. The magnitude of energy change should be linked to the chemical potential of hydrogen.

Understanding the hydrogen effect on each type of defect allows us to develop constraints that we may impose on more complex microstructure. However, we advise care, as what may seem a straight forward change in a pure material, may have several stages of effects in a complex microstructure. Fracture of materials is often dependent on its weakest link, and the final fracture may be a process which has gone through several stages where the path taken is system-specific. If we assume hydrogen makes all links weaker, the path taken through the stages of deformation may change.

Bibliography

[1] Magnus Själander, Magnus Jahre, Gunnar Tufte, and Nico Reissmann. EPIC: An Energy-Efficient, High-Performance GPGPU Computing Research Infrastructure. 12 2019.

[2] I.-H. Lin and R. Thomson. Cleavage, dislocation emission, and shielding for cracks under general loading. *Acta Metallurgica*, 34(2):187–206, 2 1986.

[3] George E. Dieter. *Mechanical metallurgy*. McGraw-Hill, 1976.

[4] Giacomo Po, Yinan Cui, David Rivera, David Cereceda, Tom D. Swinburne, Jaime Marian, and Nasr Ghoniem. A phenomenological dislocation mobility law for bcc metals. *Acta Materialia*, 119:123–135, 10 2016.

[5] M. Peach and J. S. Koehler. The forces exerted on dislocations and stress fields produced by them. *Physical Review*, 80(3):436–439, 1950.

[6] D. Weygand, L. H. Friedman, E Van der Giessen, and A. Needleman. Aspects of boundary-value problem solutions with three-dimensional dislocation dynamics. *Modelling and Simulation in Materials Science and Engineering*, 10(4):437–468, 7 2002.

[7] Wei Cai, Athanasios Arsenlis, Christopher R. Weinberger, and Vasily V. Bulatov. A non-singular continuum theory of dislocations. *Journal of the Mechanics and Physics of Solids*, 54(3):561–587, 3 2006.

[8] L. P. Kubin and G. Canova. The modelling of dislocation patterns. *Scripta Metallurgica et Materiala*, 27(8):957–962, 1992.

[9] Vasily V. Bulatov, Luke L. Hsiung, Meijie Tang, Athanasios Arsenlis, Maria C. Bartelt, Wei Cai, Jeff N. Florando, Masato Hiratani, Moon Rhee, Gregg Hommes, Tim G. Pierce, and Tomas Diaz de la Rubia. Dislocation multi-junctions and strain hardening. *Nature*, 440(7088):1174–1178, 4 2006.

[10] S. M. Keralavarma and W. A. Curtin. Strain hardening in 2D discrete dislocation dynamics simulations: A new '2.5D' algorithm. *Journal of the Mechanics and Physics of Solids*, 95:132–146, 2016.

[11] Ryan B. Sills, Nicolas Bertin, Amin Aghaei, and Wei Cai. Dislocation Networks and the Microstructural Origin of Strain Hardening. *Physical Review Letters*, 121(8):85501, 2018.

[12] E Van der Giessen and A. Needleman. Discrete dislocation plasticity: a simple planar model. *Modelling and Simulation in Materials Science and Engineering*, 3(5):689–735, 9 1995.

[13] C. Motz, D. Weygand, J. Senger, and P. Gumbsch. Micro-bending tests: A comparison between three-dimensional discrete dislocation dynamics simulations and experiments. *Acta Materialia*, 56(9):1942–1955, 5 2008.

[14] E. Tarleton, D. S. Balint, J. Gong, and A. J. Wilkinson. A discrete dislocation plasticity study of the micro-cantilever size effect. *Acta Materialia*, 88:271–282, 2015.

[15] H.H.M. Cleveringa, Erik Van der Giessen, and A. Needleman. A discrete dislocation analysis of mode I crack growth. *Journal of the Mechanics and Physics of Solids*, 48(6-7):1133–1157, 6 2000.

[16] V. Lakshmanan and J. C. M. Li. Edge dislocations emitted along inclined planes from a mode I crack. *Materials Science and Engineering: A*, 104:95–104, 10 1988.

[17] Siu Sin Quek, Zheng Hoe Chooi, Zhaoxuan Wu, Yong Wei Zhang, and David J. Srolovitz. The inverse hall-petch relation in nanocrystalline metals: A discrete dislocation dynamics analysis. *Journal of the Mechanics and Physics of Solids*, 88:252–266, 2016.

[18] V. S. Deshpande, A. Needleman, and E. Van der Giessen. Discrete dislocation plasticity modeling of short cracks in single crystals. *Acta Materialia*, 51(1):1–15, 1 2003.

[19] N. Irani, J. J C Remmers, and V. S. Deshpande. A discrete dislocation analysis of hydrogen-assisted mode-I fracture. *Mechanics of Materials*, 105:67–79, 2017.

[20] Alexander Hartmaier and Peter Gumbsch. The brittle-to-ductile transition and dislocation activity at crack tips. *Journal of Computer-Aided Materials Design*, 6(2/3):145–155, 1999.

[21] P.B. Hirsch and S.G. Roberts. Comment on the brittle-to-ductile transition: A cooperative dislocation generation instability; dislocation dynamics and the strain-rate dependence of the transition temperature. *Acta Materialia*, 44(6):2361–2371, 6 1996.

[22] P. B. Hirsch and S. G. Roberts. Modelling plastic zones and the brittle-ductile transition. *Philosophical Transactions of the Royal Society of London. Series A: Mathematical, Physical and Engineering Sciences*, 355(1731):1991–2002, 10 1997.

[23] M Tanaka, E Tarleton, and S.G. Roberts. The brittle–ductile transition in single-crystal iron. *Acta Materialia*, 56(18):5123–5129, 10 2008.

[24] Alexander Hartmaier and Peter Gumbsch. Discrete Dislocation Dynamics Simulation of Crack-Tip Plasticity. In *Continuum Scale Simulation of Engineering Materials*, pages 413–427. Wiley-VCH Verlag GmbH & Co. KGaA, Weinheim, FRG, 6 2005.

[25] Alexander Hartmaier and Peter Gumbsch. Thermal activation of crack-tip plasticity: The brittle or ductile response of a stationary crack loaded to failure. *Physical Review B - Condensed Matter and Materials Physics*, 71(2):024108, 1 2005.

[26] E. Tarleton and S.G. G. Roberts. Dislocation dynamic modelling of the brittle-ductile transition in tungsten. *Philosophical Magazine*, 89(31):2759–2769, 11 2009.

[27] U. F. Kocks. Laws for Work-Hardening and Low-Temperature Creep. *Journal of Engineering Materials and Technology*, 98(1):76, 1976.

[28] H. Mecking and U. F. Kocks. Kinetics of flow and strain-hardening. *Acta Metallurgica*, 29(11):1865–1875, 11 1981.

[29] M.F. F. Ashby and J.D. D. Embury. The influence of dislocation density on the ductile-brittle transition in BCC metals. *Scripta Metallurgica*, 19(4):557–562, 4 1985.

[30] H. Mughrabi. Dislocation wall and cell structures and long-range internal stresses in deformed metal crystals. *Acta Metallurgica*, 31(9):1367–1379, 9 1983.

[31] L.P; Kubin and Y. Estrin. Evolution of Dislocation Densities and Portevin-Le Chatelier Effect. *Acta. Metall. Mater.*, 38(5):697–708, 1990.

[32] Y. Estrin, L. S. Tóth, A. Molinari, and Y. Bréchet. A dislocation-based model for all hardening stages in large strain deformation. *Acta Materialia*, 46(15):5509–5522, 9 1998.

[33] Bjørn Holmedal, Knut Marthinsen, and Erik Nes. A unified microstructural metal plasticity model applied in testing, processing, and forming of aluminium alloys. *Zeitschrift fuer Metallkunde/Materials Research and Advanced Techniques*, 96(6):532–545, 6 2005.

[34] Ritupan Sarmah and G. Ananthakrishna. Correlation between band propagation property and the nature of serrations in the Portevin-Le Chatelier effect. *Acta Materialia*, 91:192–201, 2015.

[35] G. Ananthakrishna, Rohit Katti, and K. Srikanth. Dislocation dynamical approach to force fluctuations in nanoindentation experiments. *Physical Review B - Condensed Matter and Materials Physics*, 90(9):17–22, 2014.

[36] K. Srikanth and G. Ananthakrishna. Dynamical approach to displacement jumps in nanoindentation experiments. *Physical Review B*, 95(1):1–14, 1 2017.

[37] Y. Estrin and H. Mecking. A unified phenomenological description of work hardening and creep based on one-parameter models. *Acta Metallurgica*, 32(1):57–70, 1984.

[38] Y. Estrin and L.P. Kubin. Local strain hardening and nonuniformity of plastic deformation. *Acta Metallurgica*, 34(12):2455–2464, 12 1986.

[39] A. A. Griffith. VI. The phenomena of rupture and flow in solids. *Philosophical Transactions of the Royal Society of London. Series A, Containing Papers of a Mathematical or Physical Character*, 221(582-593):163–198, 1 1921.

[40] J. R. Rice and R. Thomson. Ductile versus brittle behaviour of crystals. *Philosophical Magazine*, 29(1):73–97, 1 1974.

[41] William H. Johnson. On some remarkable changes produced in iron and steel by the action of hydrogen and acids. *Nature*, 11(281):393, 1 1875.

[42] William H. Johnson. On some remarkable changes produced in iron and steel by the action of hydrogen and acids - Extra, 1875.

[43] L. B. Pfeil. The effect of occluded hydrogen on the tensile strength of iron. *Journal of the Franklin Institute*, 203(2):331–332, 2 1927.

[44] R. A. Oriani. Whitney Award Lecture-1987:Hydrogen—The Versatile Embrittler. *CORROSION*, 43(7):390–397, 7 1987.

[45] H. VEHOFF and W. ROTHE. GASEOUS HYDROGEN EMBRITTLEMENT IN FeSi- AND Ni-SINGLE CRYSTALS. In M. F. Ashby and J. P. Hirth, editors, *Perspectives in Hydrogen in Metals*, chapter 30, pages 647–659. Elsevier, 1 edition, 1 1986.

[46] James H. Rose, John R. Smith, and John Ferrante. Universal features of bonding in metals. *Physical Review B*, 28(4):1835–1845, 8 1983.

[47] James H. Rose, John R. Smith, Francisco Guinea, and John Ferrante. Universal features of the equation of state of metals. *Physical Review B*, 29(6):2963–2969, 3 1984.

[48] C. D. Beachem. A new model for hydrogen-assisted cracking (hydrogen "embrittlement"). *Metallurgical Transactions*, 3(2):441–455, 2 1972.

[49] T. Tabata and H. K. Birnbaum. Direct observation of the effect of hydrogen on the behavior of dislocations in iron. *Scripta Metallurgica*, 17:947–950, 1983.

[50] T. Tabata and H.K. K. Birnbaum. Direct observations of Hydrogen Enhanced Crack propagation in Iron. *Scripta Metallurgica*, 18(3):231–236, 3 1984.

[51] Reiner Kirchheim. Reducing grain boundary, dislocation line and vacancy formation energies by solute segregation. I. Theoretical background. *Acta Materialia*, 55(15):5129–5138, 9 2007.

[52] Reiner Kirchheim. Reducing grain boundary, dislocation line and vacancy formation energies by solute segregation: II. Experimental evidence and consequences. *Acta Materialia*, 55(15):5139–5148, 9 2007.

[53] Reiner Kirchheim. Revisiting hydrogen embrittlement models and hydrogen-induced homogeneous nucleation of dislocations. *Scripta Materialia*, 62(2):67–70, 1 2010.

[54] Afrooz Barnoush, Nousha Kheradmand, and Tarlan Hajilou. Correlation between the hydrogen chemical potential and pop-in load during in situ electrochemical nanoindentation. *Scripta Materialia*, 108:76–79, 11 2015.

[55] S. P. Lynch. A fractographic study of hydrogen-assisted cracking and liquid-metal embrittlement in nickel. *Journal of Materials Science*, 21(2):692–704, 1986.

[56] S. P. Lynch. Environmentally assisted cracking: Overview of evidence for an adsorption-induced localised-slip process. *Acta Metallurgica*, 36(10):2639–2661, 1988.

[57] S. P. Lynch. Hydrogen embrittlement (HE) phenomena and mechanisms. *Stress corrosion cracking: Theory and practice*, 30:90–130, 1 2011.

[58] M. Nagumo, M. Nakamura, and K. Takai. Hydrogen thermal desorption relevant to delayed-fracture susceptibility of high-strength steels. *Metallurgical and Materials Transactions A: Physical Metallurgy and Materials Science*, 32(2):339–347, 2001.

[59] M. Nagumo. Hydrogen related failure of steels – a new aspect. *Materials Science and Technology*, 20(8):940–950, 8 2004.

[60] K. Takai, H. Shoda, H. Suzuki, and M. Nagumo. Lattice defects dominating hydrogen-related failure of metals. *Acta Materialia*, 56(18):5158–5167, 2008.

[61] Michihiko Nagumo and Kenichi Takai. The predominant role of strain-induced vacancies in hydrogen embrittlement of steels: Overview. *Acta Materialia*, 165:722–733, 2 2019.

[62] Tarlan Hajilou, Malin S.B. Hope, Amin H. Zavieh, Nousha Kheradmand, Roy Johnsen, and Afrooz Barnoush. In situ small-scale hydrogen embrittlement testing made easy: An electrolyte for preserving surface integrity at nano-scale during hydrogen charging. *International Journal of Hydrogen Energy*, 43(27):12516–12529, 7 2018.

[63] Reiner Kirchheim, Brian Somerday, and Petros Sofronis. Chemomechanical effects on the separation of interfaces occurring during fracture with emphasis on the hydrogen-iron and hydrogen-nickel system. *Acta Materialia*, 99:87–98, 10 2015.

[64] J. P. Hirth and J. R. Rice. On the thermodynamics of adsorption at interfaces as it influences decohesion. *Metallurgical Transactions A*, 11(9):1501–1511, 9 1980.

[65] W Beck, J O M Bockris, J Mcbreen, and L Nanis. Hydrogen permeation in metals as a function of stress, temperature and dissolved hydrogen concentration. *Proceedings of the Royal Society of London. Series A. Mathematical and Physical Sciences*, 290(1421):220–235, 1966.

[66] H. G. Nelson and J. E. Stein. Gas-phase hydrogen permeation through alpha iron, 4130 steel, and 304 stainless steel from less than 100 C to near 600 C. Technical report, Ames Research Center, Moffett Field, California, 4 1973.

[67] G. M. Pressouyre. A classification of hydrogen traps in steel. *Metallurgical Transactions A*, 10(10):1571–1573, 10 1979.

[68] G. M. Pressouyre. Hydrogen traps, repellers, and obstacles in steel; Consequences on hydrogen diffusion, solubility, and embrittlement. *Metallurgical Transactions A*, 14(10):2189–2193, 10 1983.

[69] E. Sirois and H. K. Birnbaum. Effects of hydrogen and carbon on thermally activated deformation in nickel. *Acta Metallurgica Et Materialia*, 40(6):1377–1385, 6 1992.

[70] H. K. Birnbaum and P. Sofronis. Hydrogen-enhanced localized plasticity-a mechanism for hydrogen-related fracture. *Materials Science and Engineering A*, 176(1-2):191–202, 3 1994.

[71] I.M. M. Robertson. The effect of hydrogen on dislocation dynamics. *Engineering Fracture Mechanics*, 68(6):671–692, 3 2001.

[72] Yejun Gu and Jaafar A. El-Awady. Quantifying the effect of hydrogen on dislocation dynamics: A three-dimensional discrete dislocation dynamics framework. *Journal of the Mechanics and Physics of Solids*, 112:1–24, 3 2017.

[73] Haiyang Yu, Alan Cocks, and Edmund Tarleton. Discrete dislocation plasticity HELPs understand hydrogen effects in bcc materials. *Journal of the Mechanics and Physics of Solids*, 123:41–60, 2 2019.

[74] Ryosuke Matsumoto, Shoichi Seki, Shinya Taketomi, and Noriyuki Miyazaki. Hydrogen-related phenomena due to decreases in lattice defect energies - Molecular dynamics simulations using the embedded atom method potential with pseudo-hydrogen effects. *Computational Materials Science*, 92:362–371, 2014.

[75] Haiyang Yu, Alan C.F. Cocks, and Edmund Tarleton. The influence of hydrogen on Lomer junctions. *Scripta Materialia*, 166:173–177, 6 2019.

[76] Shinya Taketomi, Ryosuke Matsumoto, and Noriyuki Miyazaki. Atomistic simulation of the effects of hydrogen on the mobility of edge dislocation in alpha iron. *Journal of Materials Science*, 43(3):1166–1169, 2 2008.

[77] M. Wen, S. Fukuyama, and K. Yokogawa. Atomistic simulations of effect of hydrogen on kink-pair energetics of screw dislocations in bcc iron. *Acta Materialia*, 51(6):1767–1773, 4 2003.

[78] M. Itakura, H. Kaburaki, M. Yamaguchi, and T. Okita. The effect of hydrogen atoms on the screw dislocation mobility in bcc iron: A first-principles study. *Acta Materialia*, 61(18):6857–6867, 10 2013.

[79] Di Wan, Yun Deng, and Afrooz Barnoush. Hydrogen embrittlement effect observed by in-situ hydrogen plasma charging on a ferritic alloy. *Scripta Materialia*, 151:24–27, 7 2018.

[80] Di Wan, Yun Deng, Jan Inge Hammer Meling, Antonio Alvaro, and Afrooz Barnoush. Hydrogen-enhanced fatigue crack growth in a single-edge notched tensile specimen under in-situ hydrogen charging inside an environmental scanning electron microscope. *Acta Materialia*, 170:87–99, 5 2019.

[81] Domas Birenis, Yuhei Ogawa, Hisao Matsunaga, Osamu Takakuwa, Junichiro Yamabe, Øystein Prytz, and Annett Thøgersen. Interpretation of hydrogen-assisted fatigue crack propagation in BCC iron based on dislocation structure evolution around the crack wake. *Acta Materialia*, 156(June):245–253, 9 2018.

[82] H. Vehoff and P. Neumann. Crack propagation and cleavage initiation in Fe-2.6%-Si single crystals under controlled plastic crack tip opening rate in various gaseous environments. *Acta Metallurgica*, 28(3):265–272, 3 1980.

[83] Tarlan Hajilou, Yun Deng, Bjørn Rune Rogne, Nousha Kheradmand, and Afrooz Barnoush. In situ electrochemical microcantilever bending test: A new insight into hydrogen enhanced cracking. *Scripta Materialia*, 132:17–21, 4 2017.

[84] Yun Deng and Afrooz Barnoush. Hydrogen embrittlement revealed via novel in situ fracture experiments using notched micro-cantilever specimens. *Acta Materialia*, 142(September):236–247, 1 2018.

[85] Bjørn Rune Sørås Rogne, Nousha Kheradmand, Yun Deng, and Afrooz Barnoush. In situ micromechanical testing in environmental scanning electron microscope: A new insight into hydrogen-assisted cracking. *Acta Materialia*, 144:257–268, 2 2018.

[86] Vigdis Olden, Christian Thaulow, Roy Johnsen, Erling Østby, and Torodd Berstad. Influence of hydrogen from cathodic protection on the fracture susceptibility of 25%Cr duplex stainless steel - Constant load SENT testing and FE-modelling using hydrogen influenced cohesive zone elements. *Engineering Fracture Mechanics*, 76(7):827–844, 2009.

[87] V. Olden, C. Thaulow, and R. Johnsen. Modelling of hydrogen diffusion and hydrogen induced cracking in supermartensitic and duplex stainless steels. *Materials and Design*, 29(10):1934–1948, 12 2008.

[88] Vigdis Olden, Antonio Alvaro, and Odd M. Akselsen. Hydrogen diffusion and hydrogen influenced critical stress intensity in an API X70 pipeline steel welded joint – Experiments and FE simulations. *International Journal of Hydrogen Energy*, 37(15):11474–11486, 8 2012.

[89] Antonio Alvaro, Vigdis Olden, and Odd Magne Akselsen. 3D cohesive modelling of hydrogen embrittlement in the heat affected zone of an X70 pipeline steel. *International Journal of Hydrogen Energy*, 38(18):7539–7549, 6 2013.

[90] I. Adlakha, Kuntimaddi Sadananda, and Kiran N. Solanki. Discrete dislocation modeling of stress corrosion cracking in an iron. *Corrosion Reviews*, 33(6):467–475, 1 2015.

[91] Shinya Taketomi, Ryosuke Matsumoto, and Noriyuki Miyazaki. Atomistic study of the effect of hydrogen on dislocation emission from a mode II crack tip in alpha iron. *International Journal of Mechanical Sciences*, 52(2):334–338, 2010.

[92] Mao Wen, Zhiyuan Li, and Afrooz Barnoush. Atomistic study of hydrogen effect on dislocation nucleation at crack tip. *Advanced Engineering Materials*, 15(11):1146–1151, 11 2013.

[93] J. Song, M Soare, and W. A. Curtin. Testing continuum concepts for hydrogen embrittlement in metals using atomistics. *Modelling and Simulation in Materials Science and Engineering*, 18(4):045003, 6 2010.

[94] I. Adlakha and K. N. Solanki. Role of hydrogen on the incipient crack tip deformation behavior in α-Fe: An atomistic perspective. *Journal of Applied Physics*, 123(1):0–10, 2018.

[95] J. Weertman, I.-H. Lin, and R. Thomson. Double Slip Plane Crack Model. *Acta metall*, 31(4):473–482, 4 1983.

[96] Robb Thomson. Physics of Fracture. *SOLID STATE PHYSICS*, 39:1–129, 1 1986.

[97] K. F. Ha, C. Yang, and J. S. Bao. Effect of dislocation density on the ductile-brittle transition in bulk Fe - 3%Si single crystals. *Scripta Metallurgica et Materialia*, 30(8):1065–1070, 4 1994.

[98] D.E. E. Jiang and Emily A. Carter. First principles assessment of ideal fracture energies of materials with mobile impurities: implications for hydrogen embrittlement of metals. *Acta Materialia*, 52(16):4801–4807, 9 2004.

[99] S. Serebrinsky, E. A. Carter, and M. Ortiz. A quantum-mechanically informed continuum model of hydrogen embrittlement. *Journal of the Mechanics and Physics of Solids*, 52(10):2403–2430, 10 2004.

[100] Ivaylo H. Katzarov, Dimitar L. Pashov, and Anthony T. Paxton. Hydrogen embrittlement I. Analysis of hydrogen-enhanced localized plasticity: Effect of hydrogen on the velocity of screw dislocations in α -Fe. *Physical Review Materials*, 1(3):033602, 8 2017.

[101] Johannes. Weertman. *Dislocation based fracture mechanics*. World Scientific, 2 1996.

[102] Wei Cai, Vasily V. Bulatov, Sidney Yip, and Ali S. Argon. Kinetic Monte Carlo modeling of dislocation motion in BCC metals. *Materials Science and Engineering A*, 309-310:270–273, 7 2001.

[103] G. Ananthakrishna and M. S. Bharathi. Dynamical approach to the spatiotemporal aspects of the Portevin-Le Chatelier effect: Chaos, turbulence, and band propagation. *Physical Review E - Statistical, Nonlinear, and Soft Matter Physics*, 70(2 2):1–15, 2004.

[104] Mao Wen and Zhiyuan Li. Thermally activated process of homogeneous dislocation nucleation and hydrogen effects: An atomistic study. *Computational Materials Science*, 54(1):28–31, 3 2012.

[105] P. M. Anderson, J. P. Hirth, and J. Lothe. *Theory of Dislocations*. Cambridge University Press, 2017.

[106] Afrooz Barnoush and Horst Vehoff. Electrochemical nanoindentation: A new approach to probe hydrogen/deformation interaction. *Scripta Materialia*, 55(2):195–198, 7 2006.

[107] Afrooz Barnoush and Horst Vehoff. In situ electrochemical nanoindentation of a nickel (111) single crystal: hydrogen effect on pop-in behaviour. *International Journal of Materials Research*, 97(9):1224–1229, 9 2006.

[108] Nousha Kheradmand, Roy Johnsen, Jim Stian Olsen, and Afrooz Barnoush. Effect of hydrogen on the hardness of different phases in super duplex stainless steel. *International Journal of Hydrogen Energy*, 41(1):704–712, 1 2016.

[109] Dong Wang, Xu Lu, Yun Deng, Xiaofei Guo, and Afrooz Barnoush. Effect of hydrogen on nanomechanical properties in Fe-22Mn-0 . 6C TWIP steel revealed by in-situ electrochemical nanoindentation. *Acta Materialia*, 166:618–629, 3 2019.

ISBN 978-82-471-4983-6 (printed ver.)
ISBN 978-82-471-4985-0 (electronic ver.)
ISSN 1503-8181 (printed ver.)
ISSN 2703-8084 (online ver.)

NTNU
Norwegian University of
Science and Technology